University of Nebraska Medical Center
BREAKTHROUGHS FOR LIFE

University of Nebraska Medical Center
DigitalCommons@UNMC

Theses & Dissertations

Graduate Studies

Fall 12-17-2021

Development of a MUC16-Targeted Near-Infrared Antibody Probe for Fluorescence-Guided Surgery of Pancreatic Cancer

Madeline T. Olson
University of Nebraska Medical Center

Tell us how you used this information in this short survey.

Follow this and additional works at: https://digitalcommons.unmc.edu/etd

Part of the Cancer Biology Commons, Integrative Biology Commons, Oncology Commons, and the Pharmaceutics and Drug Design Commons

Recommended Citation

Olson, Madeline T., "Development of a MUC16-Targeted Near-Infrared Antibody Probe for Fluorescence-Guided Surgery of Pancreatic Cancer" (2021). *Theses & Dissertations*. 579.
https://digitalcommons.unmc.edu/etd/579

This Dissertation is brought to you for free and open access by the Graduate Studies at DigitalCommons@UNMC. It has been accepted for inclusion in Theses & Dissertations by an authorized administrator of DigitalCommons@UNMC. For more information, please contact digitalcommons@unmc.edu.

DEVELOPMENT OF A MUC16-TARGETED NEAR-INFRARED ANTIBODY PROBE FOR FLUORESCENCE-GUIDED SURGERY OF PANCREATIC CANCER

By

Madeline Terese Olson

A DISSERTATION

Presented to the Faculty of
the University of Nebraska Graduate College
in Partial Fulfillment of the Requirements
for the Degree of Doctor of Philosophy

Cancer Research
Doctoral Program

Under the Supervision of Professor Aaron M. Mohs

University of Nebraska Medical Center
Omaha, Nebraska

September 2021

Supervisory Committee:

Michael A. Hollingsworth Joyce C. Solheim Jared C. Garrison

Prakash Radhakrishnan Quan P. Ly

ACKOWLEDGEMENTS

First and foremost, I would like to thank my PI and advisor, Dr. Mohs, for the unending support, direction, and guidance over the course of my degree. Beyond frequent meetings to discuss new project directions, pitfalls, and successes, Dr. Mohs looked for every opportunity to support my career advancement, and help develop my collaborative, grantsmanship, and mentorship skills. Dr. Mohs was extremely invested in helping me to become the most inquisitive and impactful scientist I could be, and this work would truly not be possible without his encouragement, resiliency, and inspirational scientific mission. He really is an advisor that has the best interests of his students at heart, and I am so grateful for all I have learned from him in how to be an exceptional mentor and scientist. I look forward to following the inevitable future successes and exciting new directions of his lab.

I would also like to thank the members of my supervisory thesis committee: Dr. Joyce Solheim, Dr. Tony Hollingsworth, Dr. Quan Ly, Dr. Jered Garrison, and Dr. Prakash Radhakrishnan, for their feedback and direction over the course of my project. Meetings with my committee always resulted in productive discussions that shaped how I approached science and pushed my project to reach higher levels of scientific rigor. I would also like to thank Dr. Jennifer Black for serving on my comprehensive exam committee, and for serving as a mentor on the NCI T32 training grant and throughout my degree. I would like to thank Dr. Joyce Solheim, not only for her role on my supervisory committee, but also for serving as such an incredible mentor, guide, and listening ear for myself and all graduate students. I could not ask for a better representative of the cancer research program and the UNMC values.

This work would not be possible without the assistance of my current and former lab mates, who not only made this all possible but also made it bearable and

entertaining. I am thankful to my former lab members Deep Bhattacharya, Bowen Qi, Will Payne, and Josh Souchek for training me, and providing feedback on all my work, as well as Nick Wojtynek, for passing on his Mohs lab knowledge, and helping me prepare for a career in science. I am indebted to Denis Svechkarev for teaching me everything I ever wanted to know about fluorescence and bioconjugate chemistry, and for being an invaluable wealth of knowledge. I am grateful for my current lab members, Xiang Liu, Paul Lovell, Aishwarya Bapat, Katie Muilenburg, Aayushi Laliwala and Ashruti Pant who all played an immeasurable role in offering scientific collaboration, constant support and encouragement, and made lab a great place to be every day (even amidst a global pandemic). I learned an incredible amount from each one of them. I can't wait to see where they end up, and I am sure they will be successful in all their future endeavors. I am extremely grateful to current and former research technicians Carly Isder, Lucas Houser, and Megan Holmes for serving as incredible resources, for helping me whenever I needed, with whatever I needed, and providing unending support. Many thanks are also necessary to the undergraduate students, medical students, and rotating students that spent time helping me on my project over the years, and helped me become a better mentor.

There are many scientists who collaborated to make this project possible as well. I am grateful to Dr. Tony Hollingsworth, Dr. Prakash Radhakrishnan, and Craig Tuttle for sharing all their combined Mucin biology, pancreatic cancer, and AR9.6 expertise, and to Dr. Cory Brooks and his students for making large quantities of humanized antibody, conducting assays, and providing helpful insight into the antibody logistics. Thank you to Dr. Geoffrey Talmon for providing pathological feedback on countless samples over the years, and to Dr. Mark Carlson for helping to incorporate large animal models into the discussion and proposed projects.

None of this work could be completed without the assistance of funding. I am extremely appreciative of the sources that funded me as a student, including the NCI T32 training grant, the UNMC fellowship, the Nebraska University fellowship, as well as the Norman and Bernice Harris Award and Shawn Jessen Award.

I am very grateful for the friends I have made during graduate school, and for their willingness to talk through the frustrations and joys of science and pretty much everything else in life, while providing such an incredible support system both in and out of lab. I am grateful for our many shared adventures, and I look forward to following their careers and hearing about their achievements.

Finally, I would like to convey my sincere and overwhelming gratitude to my family including my mom (Beth Olson), dad (Brandon Olson), and brother (Tyler Olson). I am forever grateful for all the encouragement, love, and unwavering support they provided throughout my graduate school journey, this would not have been possible without them.

ABSTRACT

DEVELOPMENT OF A MUC16-TARGETED NEAR-INFRARED PROBE FOR FLUORESCENCE-GUIDED SURGERY OF PANCREATIC CANCER

Madeline T. Olson, Ph.D.

University of Nebraska Medical Center, 2021

Supervisor: Aaron M. Mohs, Ph.D.

Pancreatic cancer (PDAC) is an extremely lethal disease with an overall survival rate of 10% [1]. Surgery remains the only potentially curative treatment option, but resections are complicated by infiltrative disease, proximity of critical vasculature, peritumoral inflammation, and dense stroma [2, 3]. Surgeons are limited to tactile and visual cues to differentiate cancerous tissue from normal tissue. Furthermore, translating preoperative images to the intraoperative setting poses additional challenges for tumor detection, and can result in undetected and unresected lesions. Thus, PDAC has high rates of incomplete resections, and subsequently, disease recurrence [4]. Fluorescence-guided surgery (FGS) has emerged as a method to improve intraoperative detection of cancer and ultimately improve surgical outcomes. Initial clinical trials have demonstrated feasibility of FGS for PDAC, but there are limited targeted probes under investigation for this disease, highlighting the need for development of additional novel biomarkers to reflect the PDAC heterogeneity. MUCIN16 (MUC16) is a glycoprotein that is overexpressed in 60-80% of PDAC, yet this biomarker has not been investigated for FGS of this disease. Therefore, the goal of this project was to develop a MUC16-targeted fluorescent probe for intraoperative identification of PDAC through optical surgical navigation.

This dissertation describes the development of the fluorescent antibody conjugate, termed AR9.6-IRDye800, from inception to translational efficacy and safety studies. Initial studies demonstrated that AR9.6 bound to MUC16 *in vitro*, and demonstrated that binding was retained after conjugation to the near-infrared dye, IRDye800. Subcutaneous and orthotopic mouse models of pancreatic cancer demonstrated that this conjugate could target MUC16-expressing pancreatic cancer *in vivo,* and could identify PDAC intraoperatively, with significantly higher tumor to background ratios as compared to a non-specific IgG control. Metastatic lesions were identified under AR9.6-IRDye800 guidance, and fluorescence localization was observed microscopically in resected primary tumors and metastatic lesions. To build on the translational potential of this imaging probe, a humanized variant of the AR9.6 fluorescent conjugate was developed and investigated. This conjugate, termed huAR9.6-IRDye800, showed equivalent binding properties to its murine counterpart. Using an optimized dye:protein ratio of 1:1, *in vivo* studies demonstrated high tumor to background ratios in MUC16-expressing tumor models, and delineation of tumors in a patient-derived xenograft model. Safety, biodistribution, and toxicity studies were conducted, and demonstrated that huAR9.6-IRDye800 was safe, did not yield evidence of histological toxicity, and was well tolerated *in vivo*.

The results from this work conclude that AR9.6-IRDye800 is an efficacious and safe imaging agent for identifying pancreatic cancer intraoperatively through fluorescence-guided surgery. Future studies will investigate additional large animal models, patient stratification, development of companion MUC16 diagnostics and theranostics, and further safety, toxicity and efficacy studies to enable clinical translation.

TABLE OF CONTENTS

ACKOWLEDGEMENTS i

ABSTRACT iv

TABLE OF CONTENTS vi

Chapter 1: Introduction 1

1.1 Image-Guided Surgery 1

1.1.1 Clinical Relevance 1

1.1.2 Contrast Agents 2

1.1.3 Instrumentation 8

1.2 Tumor Targeting Strategies – Passive 11

1.2.1 Selective Accumulation 11

1.2.2 Challenges to Implementation 13

1.2.3 Proposed Strategies for Improved Implementation 14

1.3 Tumor Targeting Strategies – Active 15

1.3.1 Antibodies and Antibody Derivatives 17

1.3.2 Peptides 18

1.3.3 Aptamers 19

1.3.4 Ligand-Based Targeting 20

1.3.5 Improving Active Targeting 20

1.4 In Vivo *vs.* Ex Vivo Imaging 23

1.5 Clinical Translation 26

1.6 Opportunities in Image-Guided Surgery 33

Chapter 2: Development and Investigation of AR9.6-IRDye800 for PDAC 37

2.1 Introduction 37

2.2 Materials and Methods 39

2.2.1 Antibody Conjugation 39

2.2.2 Cell Culture 40

2.2.3 Western Blot 40

2.2.4 Immunofluorescence 41

2.2.5 Antibody Internalization 42

2.2.6 Animal Models 42

2.2.7 Fluorescence Imaging Dynamics 43

2.2.8 Fluorescence-Guided Surgery 43

2.2.9 Orthotopic Tumor Histology 44

2.2.10 Human Pancreatic Cancer Samples 44

2.2.11 Statistical Analysis 45

2.3 Results 45

2.3.1 MUC16 in Pancreatic Cancer Patients 45

2.3.2 Synthesis and *In vitro* Validation of MUC16 Expression 48

2.3.3 Determination of AR9.6-IRDye800 Optimal Imaging Time from Tumor Signal Dynamics 51

2.3.4 Fluorescence-Guided Surgery 57

2.4 Discussion 65

Chapter 3: Determining Translational Potential with huAR9.6-IRDye800 for FGS 70

3.1 Introduction 70

3.2 Materials and Methods 72

3.2.1 Cell Culture: 72

3.2.2 Antibody Conjugation 73

3.2.3 Binding Assessment 73

3.2.4 Western Blotting 74

3.2.5 Fluorescent Microscopy 75

3.2.6 Animal Models 75

3.2.7 Optimal Dye: Protein Ratio Assessment: 76

3.2.8 Dynamic Contrast Enhancement: 76

3.2.9 Immunohistochemistry 76

3.2.10 Fluorescence-Guided Surgery 77

3.2.11 Statistical Analysis 78

3.3 Results 78

3.3.1 HuAR9.6 and HuAR9.6-IRDye800 Bind MUC16 78

3.3.2 Impact of Dye to Protein Ratio on Biodistribution 84

3.3 3 Dynamic Contrast Enhancement and Role of Biomarker Expression in Accumulation of huAR9.6-IRDye800 90

3.3.4 FGS 99

3.4 Discussion 107

Chapter 4: Safety, Toxicity, and Long-Term Biodistribution of HuAR9.6-IRDye800 111

4.1 Introduction 111

4.2 Methods and Materials 113

4.2.1 Antibody Conjugation 113

4.2.2 Biodistribution, Safety, and Toxicity 113

4.2.3 Statistical Analysis 114

4.3 Results 114

4.3.1 Biodistribution 114

4.3.2 Blood Chemistry Analysis 123

4.3.3 Toxicity and Organ Pathology 131

4.4 Discussion 137

Chapter 5: Conclusions and Future Perspectives 139

5.1 Conclusions 139

5.2 Future Perspectives 142

5.2.1 Large Animal Models 142

5.2.2 Incorporation of Paired Clinical Imaging Systems and Standardized Imaging Methodology 143

5.2.3 Clinical Translation 147

5.2.4 Addressing Neoadjuvant Therapy and Antigenic Shift 149

5.2.5 Antibody Cocktail 149

5.2.6 Reducing off-target fluorescence 150

5.2.7 Application in Multiple Tumor Types and in Metastatic Lesions. 152

5.2.8 Photoimmunotherapy 153

5.2.9 Development of a Diagnostic Imaging Agent 155

5.2.10 Theranostic Development and ADCs 156

Bibliography 160

List of Figures:

Figure 1: Fluorescence Guided Surgery Instrumentation 10

Figure 2: Passive Targeting Mchanisms and Barriers 12

Figure 3: Tumor Targeting Strategies 16

Figure 4: Dual probe ex vivo specimen imaging 26

Figure 5: Goggles for FIGS and cancer Detection 33

Figure 6: Multimodal applications of FGS 35

Figure 7: MUC16 expression in human pancreatic ductal adenocarcinoma samples 48

Figure 8: Synthesis and in vivtro characterization of antibody conjugates 51

Figure 9: Tumor accumulation of fluorescent antibody conjugates 53

Figure 10: Biodistribution of AR9.6 in a Colo357 subcutaneous xenograft model over 144 hr. 54

Figure 11: Internalization of AR9.6-IRDye800 at 1 and 24 hrs after incubation 55

Figure 12: Biodistribution of AR9.6-IRDye800 at 144 hr after injection 57

Figure 13: Summary of imaging systems use to conduct fluorescence-guided surgery studies 59

Figure 14: Fluorescence-guided surgery in orthotopic pancreatic cancer 60

Figure 15: Biodistribution and signal of AR9.6-IRDye800 and IgG-IRDye800 in an orthotopic xenograft model 62

Figure 16: Spectral analysis of tumors and fluorescent histology 63

Figure 17: Identification of micro-metastases. 65

Figure 18: humanized AR9.6 binding 82

Figure 19: Characterization of huAR9.6-IRDye800 conjugates 83

Figure 20: Fluorescence microscopy of huAR9.6-IRDye800 binding to human PDAC cells 84

Figure 21: Internalization of huAR9.6-IRDye800 within MUC16 expressing PDAC cells after 24 hours 85

Figure 22: Representative images of biodistribution with varying dye: protein ratios 88

Figure 23: Quantified signal from resected organs with varying dye:protein ratios 89

Figure 24: Key clearance organs from varying dye:protein ratios imaged with the Curadel 90

Figure 25: Key clearance organs from varying dye:protein ratios imaged with the Fluobeam 91

Figure 26: Expression of MUC16 in human PDAC cells evaluated for subcutaneous xenograft models 94

Figure 27: Immunohistochemistry of MUC16 in PDAC tumors 95

Figure 28: Dynamic contrast enhancement with huAR.6-IRDye800 in MUC16 negative, moderate, and high expressing tumors 96

Figure 29: Tumor to background ratios from dynamic contrast enhancement study 97

Figure 30: Biodistribution in key clearance organs 9 days post-injection of huAR9.6-IRDye800 98

Figure 31: Interim necropsy conducted at 72 hours post-injection 99

Figure 32: Macroscopic and microscopic imaging of huAR9.6-IRDye800 injected tumors 100

Figure 33: Representative screened pancreatic cancer PDX models 102

Figure 34: Images from selected PDX tumor model 103

Figure 35: Fluorescence Guided Surgery in PDX Model Representative Images 106

Figure 36: Histological Analysis of PDX Model 107

Figure 37: Day 1 biodistribution study 119

Figure 38: Day 1 comparison of mean fluorescent signal in resected organs between male and female mice 120

Figure 39: Day 14 biodistribution study 121

Figure 40: Day 14 comparison of mean fluorescent signal in resected organs between male and female mice 122

Figure 41: Day 28 biodistribution study 123

Figure 42: Day 28 comparison of mean fluorescent signal in resected organs between male and female mice 124

Figure 43: Blood chemistry values from Day 1 time point 128

Figure 44: Blood chemistry values from Day 14 time point 130

Figure 45: Blood chemistry values from Day 28 time point 132

Figure 46: Change in mouse weights over time 135

Figure 47: Proposed workflow of future development of huAR9.6-IRDye800 149

Figure 48: Contextualizing fluorescence-guided surgery in the continuum of cancer care 162

List of Tables:

Table 1: Summary of Select Contrast Agents for use in FGS 7

Table 2: Representative Clinical Trials for FGS 30

Table 3: Blood Chemistry Analysis from Day 1 time point 127

Table 4: Blood Chemistry Analysis from Day 14 time point 129

Table 5: Blood Chemistry Analysis from Day 28 time point 131

Table 6: Histological evaluation of key clearance organs from Day 1 time point 136

Table 7: Histological evaluation of key clearance organs from Day 14 time point 137

Table 8: Histological evaluation of key clearance organs from Day 28 time point 138

Table 9: Nonclinical studies needed for optical imaging agents 151

List of Abbreviations:

PDAC	Pancreatic cancer
FGS	Fluorescence-Guided Surgery
MUC16	MUCIN16
NIR	Near-Infrared
SNR	Signal to Noise Ratio
5-ALA	5-aminolevulinici acid
ICG	Indocyanine Green
LED	Light-Emitting Diode
EPR	Enhanced Permeability and Retention
SBR	Signal to Background Ratio
EGFR	Epidermal Growth Factor Receptor
VEGF	Vascular Endothelial Growth Factor
RGD	Arg-Gly-Asp
SST	Somatostatin
GRP	Gastrin Releasing Peptide
NT	Neurotensin
pHLIP	pH Low Insertion Peptide
SELEX	Systematic evolution of ligands by exponential enrichment
MRI	Magnetic Resonance Imaing
PET	Positron Emission Tomography
PAI	Photoacoustic Imaging
CT	Computed Tomography
IFSA	Intraoperative Frozen Section Analysis
CEA	Carcinoembryonic Antigen

CNS	Central Nervous System
mAb	Monoclonal Antibody
PBS	Phosphate buffered saline
NHS	N-hydroxysuccinimide
TBST	Tris-Buffered Saline Polysorbate 20
TBS	Tris-Buffered Saline
RIPA	Radioimmunoprecipitation assay
BSA	Bovine Serum Albumin
DAPI	4’,6-diamidino-2-phenylindole
UNMC	University of Nebraska Medical Center
IACUC	Institutional of Animal Care and Use Committee
ROI	Region of Interest
OCT	Optimal Cutting Temperature Compound
H&E	Hematoxylin and Eosin
RAP	Rapid Autopsy Program
TBR	Tumor to Background Ratio
PANIN	Pancreatic Intraepithelial Neoplasia
PDX	Patient-derived xenograft
CDR	Complementary Determining Region
ALB	Albumin
ALP	Alkaline Phosphatase
AMY	Amylase
TBIL	Total Bilirubin
BUN	Blood Urea Nitrogen
CA+	Calcium

PHOS	Phosphorus
GLU	Glucose
NA+	Sodium
K+	Potassium
TP	Total Protein
GLOB	Globulin
OCM	Oncopig Cancer Model
PIT	Photoimmunotherapy
ROS	Reactive Oxygen Species

Chapter 1: Introduction

This chapter is adapted from a previous publication by Olson, Ly, and Mohs. Reprinted with permission from [5], Copyright © 2018, World Molecular Imaging Society.

1.1 Image-Guided Surgery

1.1.1 Clinical Relevance

With over 14 million estimated new cases, and 8 million deaths reported in the most recent *World Cancer Report*, cancer remains a leading cause of death across the globe [6]. In the United States alone, over 1.73 million new cases of cancer and over 600,000 deaths are estimated in 2018 [7]. Despite significant expansion and diversification of treatment options, surgical resection continues to serve as the cornerstone of treatment for most solid cancers. However, there are many complexities to tumor resections that require further investigation and improvement. Complete tumor resection relies on a surgeon's ability to differentiate between malignant and benign tissue using palpable and visual cues, but the infiltrative nature of cancerous tissue can make it difficult for surgeons to remove the entire tumor. The lack of differentiation, involvement of critical nerves and vasculature, and the stage of disease progression can complicate a tumor resection and lead to either incomplete removal or removal with significant morbidity [8]. If the tumor is not removed in its entirety, the residual cells at the surgical margin that result in positive margins can lead to disease recurrence [9–11]. Fluorescence-guided surgery (FGS) offers a strategy to assist surgeons in delineating cancerous tissue through the use of fluorescence. Using this technology to color code the surgical field would better equip surgeons with the visual information needed to remove the tumor in its entirety or abort if needed, avoid inadvertent injury to non-cancerous tissue, confirm cancerous lymph nodes and metastases, and decrease disease recurrence.

FGS may not be an equally beneficial solution for all cancer types. For example, in both ovarian and pancreatic cancers, the disease is often highly advanced and metastatic upon detection [12, 13]. Only 20% of pancreatic cancer patients are candidates for resection because of the aggressive dissemination of the disease and the high degree of involvement of the surrounding vasculature [14–17]. Even among pancreatic cancer patients who undergo surgical resection, 80% will eventually succumb to disease recurrence [13, 15]. In ovarian cancer, it is common that patients undergo debulking surgery to leave less than one centimeter of residual disease, but because of the advanced stage of the disease, adjuvant chemotherapy is often used in conjunction with resection in an attempt to ablate microscopic disease [12, 18]. However, like pancreatic cancer, most patients with ovarian cancer develop recurrent disease [19]. To make surgical resection a viable and curative treatment option for highly metastatic cancers such as these, the development of early detection biomarkers is essential.

In addition to highlighting the primary tumor, FGS may play a critical role in detecting early peritoneal disease and preventing inadvertent damage to critical and healthy tissue. Fluorescent detection of early peritoneal disease can reduce the number of unnecessary subsequent surgeries required to remove undetected metastatic disease [20, 21]. Nerve damage is a potential complication during surgical resection, especially in prostate and head and neck cancers, among others, because the fine innervations are difficult to differentiate from the tumor tissue. Damage to nerves during surgical resection can result in increased post–operative morbidity, including increased pain and impaired function [22, 23]. Extensive nerve identification during surgery often results in prolonged operation time and possible damage to surrounding tissue [24]. However, the use of FGS has shown efficacy in labeling the nerves to avoid this type of injury during resection [22, 25–27].

1.1.2 Contrast Agents

Contrast agents applicable to FGS generally fall into two categories: either visible or near infrared (NIR) dyes. NIR dyes (~700-1000 nm) offer potential advantages compared to visible dyes because of increased depth of light penetration, decreased light scattering, and lower tissue autofluorescence in the NIR region [28]. The properties of NIR fluorophores provide the high signal to noise ratio (SNR) required to aid surgeons in better differentiating cancerous tissue from normal tissue. **Table 1** summarizes the properties of contrast agents that are frequently investigated for FGS, including methylene blue, 5-aminolevulinic acid (5-ALA), cyanine-based dyes, including indocyanine green (ICG), IRDye800, and Dyomics dyes, and quantum dots. Fluorescein was an early dye used to illuminate tumors, but it is no longer as prevalent for FGS because of its high autofluorescence and low tissue penetration [29]. Additionally, several cases have reported fluorescein causing anaphylactic shock [30, 31]. Each contrast currently used for FGS comes with its own considerations, emission wavelength, quantum yield, toxicity, accumulation, and regulatory approval.

Methylene Blue

Methylene blue is a widely utilized, FDA approved, visible wavelength dye [32]. This dye was developed as an alternative to its predecessor, isosulfan blue (Lymphazurin). Because there was a shortage of isosulfan blue when sentinel lymph node mapping was accepted as the staging modality for breast cancer and melanoma, methylene blue is now commonly used instead. Furthermore, there were reports of a 1-3% incidence rate of anaphylaxis with isosulfan blue. There have been reports of anaphylactic shock with methylene blue, but the rate is much lower. Regardless, the use of this dye is limited during pregnancy, because of its teratogenic potential [33, 34]. Nevertheless, this contrast agent has many applications for FGS, as well as photodynamic therapy for cancer [35]. Previous studies have demonstrated the efficacy of this dye in identifying vital structures such as parathyroid glands, nerves, and ureters,

to avoid injury during cancer resection [36–40]. Additionally, methylene blue has been used to identify sentinel lymph nodes and the presence of certain tumors [41–45]. However, uptake of this dye is highly variable and dependent on tumor type. Methylene blue is further limited because it lacks the favorable properties of NIR dyes, and it requires a high dose for detection in order to overcome autofluorescence [32].

5-ALA

5-ALA is a visible wavelength dye that was recently FDA approved for use as a fluorescent imaging agent in patients with high grade gliomas. A precursor molecule of the hemoglobin synthesis pathway, 5-ALA catalyzes the production and accumulation of the compound protoporphyrin IX (PpIX) in cancerous tissue. This compound exhibits fluorescence when excited by a violet-blue light source (405 nm), allowing for the visualization of cancerous tissue [46, 47]. The use of 5-ALA is associated with high specificity and positive predictive values [48]. However, while improved resection with 5-ALA correlates to improved survival rates, there are also limitations to the use of this contrast agent, particularly its inconsistency [49]. Visible fluorescence is uncommon in low grade gliomas, and thus the usage of 5-ALA guided resection is restricted to solely higher grades. Previous studies have noted variance in the type of fluorescence, including both solid red fluorescence in the tumor tissue, and vague pink fluorescence at the transition zone between normal and cancerous tissue [50]. In areas of lower fluorescence, the ability of the dye to accurately identify cancerous tissue is sacrificed, thus poor sensitivity and low negative prediction values remain concerns for the use of 5-ALA [32, 46, 48, 49, 51].

ICG

ICG is an FDA-approved NIR tricarbocyanine dye that has many uses in the clinic, and expanding uses in FGS. This dye has very low toxicity, and has been

approved for use in determining hepatic function, cardiac output, and ophthalmic perfusion for decades [32, 52]. ICG has also shown efficacy for FGS in sentinel lymph node mapping, evaluating blood flow in reconstructed organs, and identifying and marking tumors for a variety of different solid cancer types [52–57]. Because ICG is a NIR dye, it is able to more deeply penetrate tissues, making it a good candidate for real-time FGS. This dye is widely used across clinical trials and patient care settings, and has shown great potential for use with FGS. However, ICG is limited by its aqueous instability, short circulation time, and concentration-dependent quenching. ICG also lacks the functional groups necessary for conjugation, rendering it a non-specific contrast agent. However, studies have shown that encapsulation of ICG improves its targeting abilities and circulation time, offering solutions to improve ICG for FGS use. [58, 59].

Dyes on the Rise

While 5-ALA, Methylene Blue, and ICG are the most prominent dyes entering clinical trials and approved for clinical usage, many other contrast agents are showing significant promise in the pre-clinical phases. Cyanine derivatives (e.g. Cy7.5) and those developed by Dyomics (Jena, Germany) and LI-COR (Lincoln, NE, USA) Dy800, quantum dots, and others have been adapted for FGS use in preclinical investigations **(Table 1)**. IRDye800 (LI-COR) is perhaps the most advanced, appearing in current clinical trials, particularly in conjugation with antibodies [60–62]. The use of cyanine dyes overall, however, is still mostly restricted to the laboratory, but the conjugatable nature, stability, and high fluorescent capabilities of these dyes suggest potential for further success and clinical translation in the future [63, 64]. Quantum dots have also demonstrated significant potential for use in bioimaging applications, but concerns with safety and toxicity, especially the release of heavy metal ions and generation of reactive

oxygen species, need to be addressed [65]. Development of non-toxic and biocompatible quantum dots is the next step towards clinical translation [66].

Table 1: Summary of Select Contrast Agents for use in FGS, Reprinted with permission from [5], © 2018, World Molecular Imaging Society.

Fluorophore	Excitation/Emission (nm)	Target	Applications in FIGS	Approval Phase	References
5-ALA	405/635	Non-specific	Glioma detection	FDA approved	[46–51]
Methylene Blue	665/686	Non-specific	Vital structure detection, SLN, tumor detection	FDA approved	[33–45]
ICG	800/822	Non-specific	SLN, reconstruction, tumor detection	FDA approved	[28, 52–59]
IRDye800CW	774/789	Non-specific, conjugatable	Tumor detection and imaging	Clinical Trials	[28, 60–62]
Dy800	777/791	Non-specific, conjugatable	Tumor detection and imaging	Pre-clinical	[67–69]
Other Cyanine dyes	Cy 5 – 658/666 Cy 5.5 – 679/696 Cy 7 – 747/774 Cy 7.5 – 788/808	Non-specific, conjugatable	Tumor detection and imaging	Pre-clinical	[28, 64, 70]
Quantum Dots	700-1500	Non-specific, conjugatable	Tumor detection and imaging	Pre-clinical	[28, 63]

1.1.3 Instrumentation

FGS is advantageous to other imaging modalities such as CT or MRI because it is less expensive, more mobile, and more feasible for integration into the surgical theater [71]. Additionally, FGS provides surgeons with real-time intraoperative feedback. FGS also lacks the ionizing radiation used in other imaging modalities, and is seen as extremely safe for use with clinically approved contrast agents and probes [35]. A typical FGS instrument has three main optical components: an excitation source, a collection source, and a display **(Figure 1)**. The excitation source must be able to excite the fluorophore at a working distance from the surgical field and emit a light that does not overlap with the emission wavelength of the fluorophore. Ideally, excitation light should be centered around the peak absorption wavelength for the fluorophore in use [72]. Common excitation sources are laser diodes, light-emitting diodes (LED), or filtered broadband lamps. Filtered broadband lamps are not ideal for image-guided surgery because they are inefficient. These lamps produce excessive heat and lose significant optical power on the surgical field. Additionally, many photons must be discarded in order to produce a narrow enough band of excitation [73–75]. Therefore, LEDs and laser diodes are preferential for use in FGS. However, each of these comes with its own considerations as well. LEDs provide a compromise of adequate efficiency, spectral confinement, and cost. However, heat dissipation is also a concern for this type of excitation source [72]. Laser diodes are the most precise in terms of spatial and spectral confinement, but raise concerns in terms of safety and cost [71, 73]. The collection source plays a critical role in FIGS instrumentation in transmitting the NIR signal from the excited fluorophore to the camera for interpretation. The sensitivity of detection is greatly determined by the background signal. In order to achieve a high level of sensitivity for the NIR signal, the FGS hardware must be able to filter out and minimize background light. Differences in hardware design and emission filtration techniques can

play a critical role in limiting the background signal and improving the sensitivity of FGS instrumentation. [73–75]. Display monitors are the most common form of image display used to integrate the NIR and surgical field images to provide real-time feedback to surgeons. Most current display monitors feature an image of the surgical field next to an image of the NIR region on the surgical field. Previous designs have suggested developing a more seamless integration by superimposing the NIR image onto the image of the surgical field [8]. A recent review by DSouza A. et al. extensively compares current FGS instrumentation systems and their efficacy, as well as features of FGS systems that are most valued for clinical implementation. Increasing sensitivity to low contrast agent concentrations, obtaining quantification of fluorophore concentration, and adapting to multi-fluorophore imaging capabilities are important considerations for FGS instrumentation development [74].

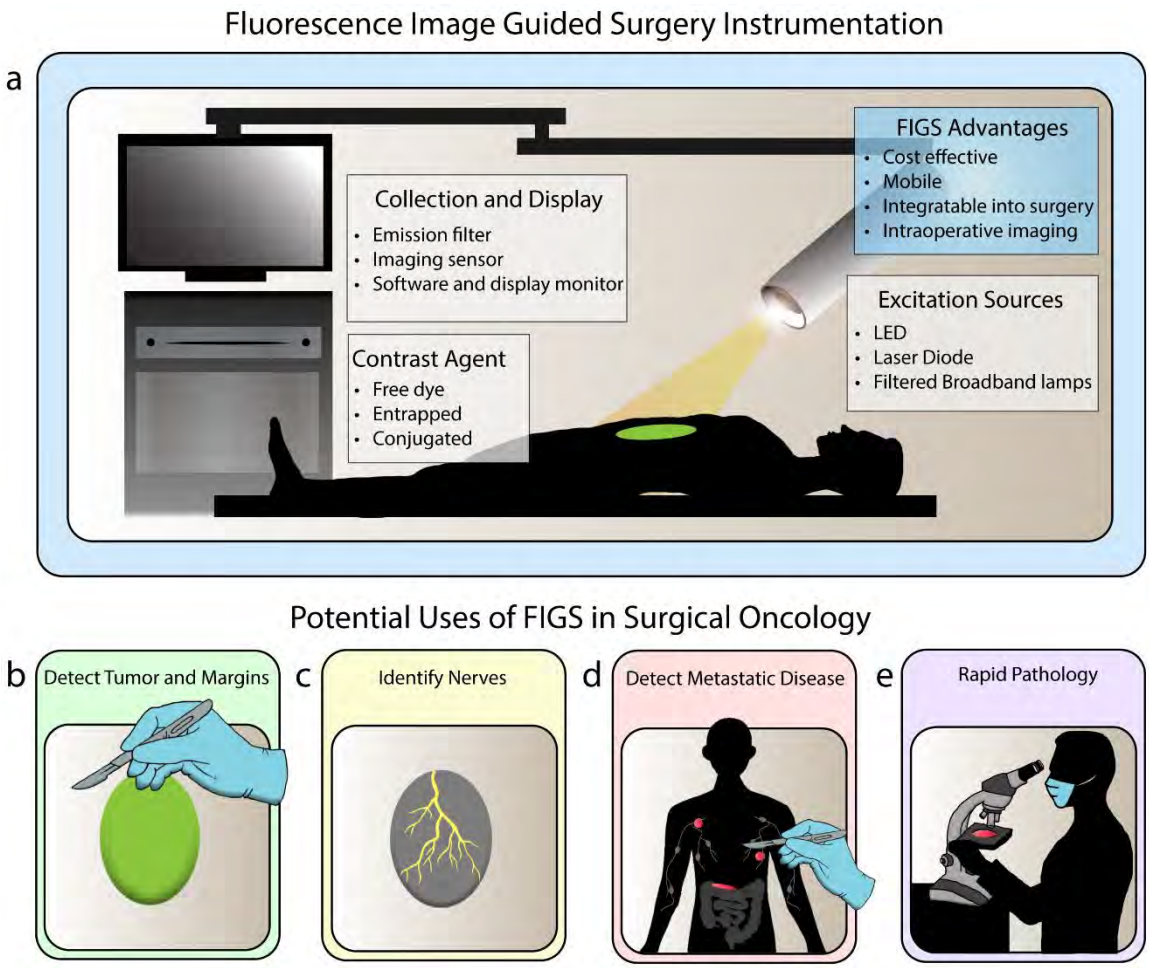

Figure 1: FIGS instrumentation and potential uses**. (A)** FIGS instrumentation consists of three critical components: an excitation source, a collection source, and a display. The excitation source is responsible for exciting the fluorophore, the collection source detects fluorescent emission and discards other light, and the display provides intraoperative real-time feedback of the surgical field. Contrast agents for FIGS can be used in several formulations, including free dyes, dyes entrapped in nanoparticles, and dyes conjugated to targeting moieties. FIGS has many potential applications in the field of surgical oncology. **(B)** Surgeons are able to detect tumors and tumor margins with FIGS, which can result in a reduction in recurrence. **(C)** Additionally, FIGS can be used to identify critical nerves during surgery, to avoid injurious resection. **(D)** FIGS has shown efficacy in detecting metastasis in addition to the primary tumor, especially in lymph nodes. **(E)** Pathologists can use FIGS for rapid ex vivo analysis of tissue samples, to confirm negative margins. (Originally published by Olson, Ly, and Mohs [5], reprinted with permission from © 2018, World Molecular Imaging Society).

1.2 Tumor Targeting Strategies – Passive

1.2.1 Selective Accumulation

The strategy of passive targeting was derived from the observation that certain macromolecules preferentially accumulate in tumors [76–78]. Passive targeting for the delivery of both free and conjugated contrast agents for FGS exploits the enhanced permeability and retention (EPR) effect to provide selective and preferential accumulation of contrast agents in tumor tissue, as shown in **Figure 2**. The biological basis for this phenomenon stems from the unique properties of vasculature and lymphatics in the tumor microenvironment. As tumors increase in size, inadequate delivery of oxygen and vital nutrients create a hypoxic environment in the center of the tumor. This hypoxic condition induces the expression of angiogenic growth factors to form neovasculature that will support the rapidly proliferating cells [79]. However, the architecture of this new vasculature is irregularly dilated, highly disorganized, and hyper-permeable [80–82]. A loosened association between pericytes and endothelial cells further contributes to the vascular abnormality and hyper-permeability [83]. In addition to faulty vasculature, poor lymphatic distribution and the markedly impaired lymphatic drainage in the tumor [84, 85] create a retentive tumor environment that can potentially be utilized in FGS due to the deposition of contrast agents in the tumor tissue [86, 87].

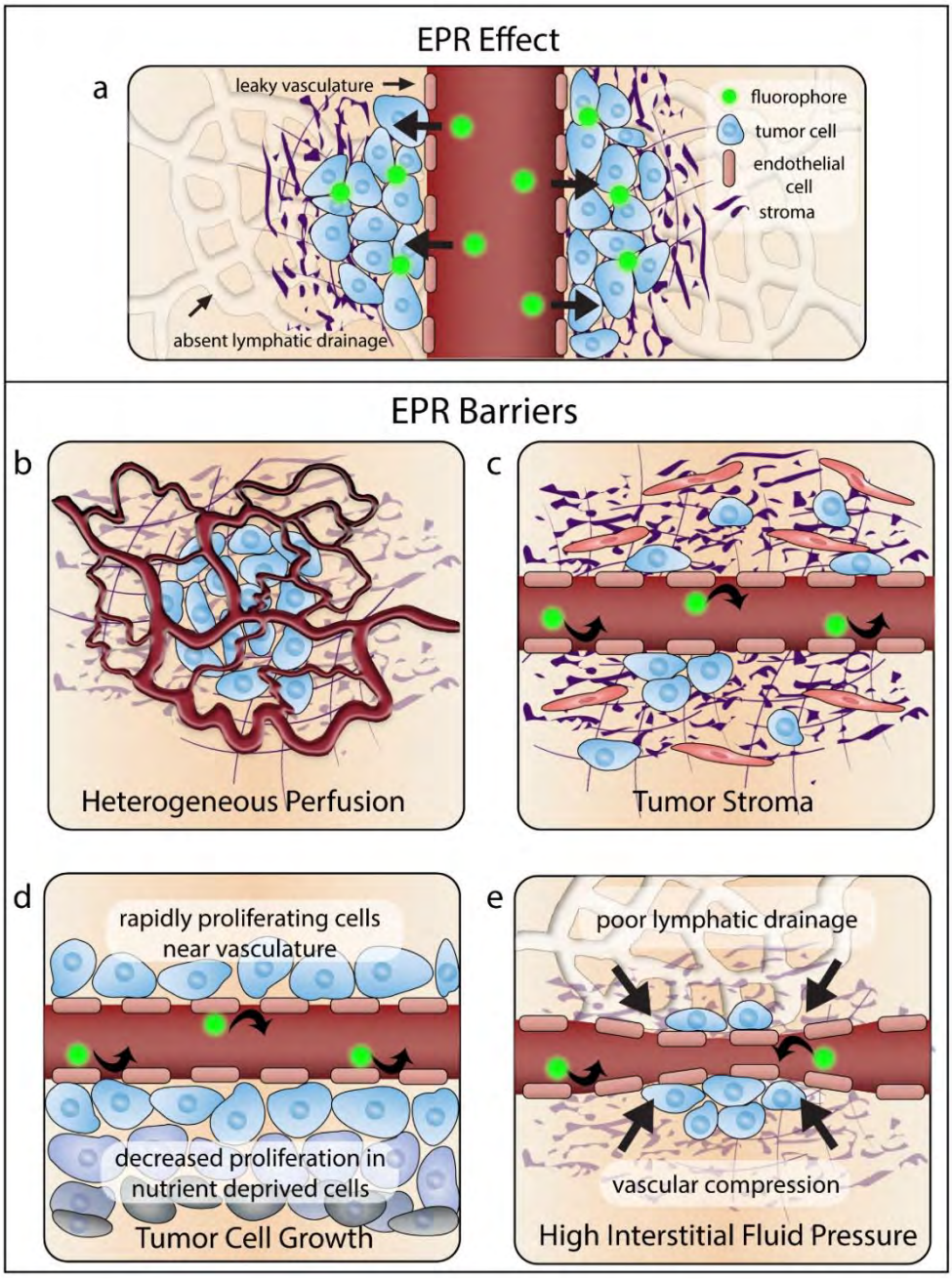

Figure 2: Passive targeting mechanisms and barriers: **(A)** the strategy of passive targeting for FIGS is based on the enhanced permeability and retention effect in tumors. Contrast agents enter the tumor through the leaky vasculature and stay in the tumor because of poor drainage. However, there are many barriers to the efficacy of this targeting strategy. **(B)** Heterogeneous perfusion from abnormal vasculature can result in inadequate perfusion in some areas of the tumor. **(C)** The presence of a dense tumor stroma can prevent penetration of contrast agents. **(D)** High gradients of tumor cell growth near to the vasculature can increase pressure and prevent contrast agents from leaking into the tumor. **(E)** High interstitial fluid pressure from inadequate lymphatic drainage can also prevent contrast agent deposition. (Originally published by Olson, Ly, and Mohs [5], reprinted with permission from © 2018, World Molecular Imaging Society)

1.2.2 Challenges to Implementation

Despite its proposed efficacy, there are many challenges involved with the implementation of EPR as a potential mechanism for contrast agent delivery. One criticism of this method of delivery is its relatively modest results, suggesting less than a 2-fold increase in delivery to tumor tissues in comparison to normal tissues [88, 89]. Because of the heterogeneity of tumors, it is difficult to predict the extent of the EPR in a specific patient. Tumor size, location, and organ type all play a role in the magnitude and presence of the EPR effect. While the unique characteristics of the tumor microenvironment are credited for the generation of the EPR effect, the same biological factors can significantly impede the efficacy of the phenomenon. For example, as depicted in **Figure 2B-E**, heterogeneous perfusion, gradients of tumor cell growth, stress from the tumor stroma (including fibroblasts, mesenchymal cells, and immune cells), and high interstitial fluid pressure can contribute to the impediment of contrast agent delivery [88–90]. Tumor vasculature abnormalities often result in areas of poor and heterogeneous perfusion throughout the tumor. While the leaky tumor vasculature may contribute to contrast agent retention, heterogeneous blood flow can impede the homogenous delivery of contrast agents in the tumor tissue [90]. These variations in blood supply also lead to obscure gradients in tumor cell growth. While tumor cells proliferate rapidly near the vasculature, proliferation decreases at sites distant to the vasculature. The high density of proliferating cells surrounding the vasculature can compress blood vessels and lymphatic vessels, preventing the convection of contrast agents in certain regions of the tumor [91–93]. Increasing density of tumor cell growth combined with poor lymphatic drainage result in very high interstitial pressure inside of the tumor.

While the dense tumor center has a very high interstitial fluid pressure, there is a significant drop in pressure at the tumor periphery, which may result in the leakage of

contrast agents into the peritumoral tissue [90, 94, 95]. The dense extracellular matrix of the tumor stroma further amplifies the solid stress in the tumor, constructing a collagen-rich network that hinders uniform contrast agent deposition [89, 90, 96]. Given the extent of the biological barriers, the EPR must be validated and improved upon. Otherwise, insufficient and unpredictable contrast agent delivery may render passive targeting an obsolete strategy for FGS.

1.2.3 Proposed Strategies for Improved Implementation

While there is significant controversy surrounding the prevalence and usefulness of the EPR effect, current research has demonstrated potential strategies to reorganize the tumor microenvironment to improve the EPR as well as to use the presence of the EPR as a biomarker. Microenvironment alteration strategies include modifying tumor vasculature and blood flow, increasing vascular permeability, modulating the tumor stroma, and killing cancer cells [88, 89, 97–99]. Isolating biomarkers for the presence of the EPR effect has also been suggested to identify potential candidates for receiving nanotherapeutics and passive delivery of contrast agents [100–102]. The implications of the EPR in personalized medicine, as well as the regulatory appeal, recognize the potential and translational importance of the EPR effect. Compared to highly specific targeted probes, passive targeting via the EPR effect is advantageous in its use of generic fluorescent probes, such as Methylene Blue and ICG. These agents have already been approved for use in the clinic, whereas targeted probes have yet to see regulatory approval [103]. Despite the significant barriers to implementation of the EPR effect as a delivery strategy for FGS, current research has validated the potential for strategic improvements and clinical translation of utilizing the effect.

1.3 Tumor Targeting Strategies – Active

The strategy of active targeting in FGS is based on the recognition of a fluorescent moiety-conjugated ligand by its target receptor on a tumor. This technique harnesses the unique microenvironment of a tumor, focusing on using ligands to target differentially expressed proteins in tumors for increased, and more precise, contrast agent delivery. The accessibility of the tumor receptor and its level of expression are important factors to consider in active targeting. Ligands used to target the overexpressed receptor on the tumor should have a high binding affinity and low toxicity, exhibit high specificity, and present groups for conjugation to a contrast agent for imaging [104]. As shown in **Figure 3**, antibodies, antibody fragments, proteins, peptides, aptamers, small molecules, and nanoparticles are examples of commonly used ligands used to target tumor receptors for FGS. While active targeting probes may achieve a higher degree of specificity for the tumor target than passive targeting, background noise and non-specific binding still occur, suggesting the need for further improvement. High background noise and non-specific binding can significantly limit the detection capabilities of FGS, inhibiting the surgeon's ability to differentiate cancerous tissue and metastatic lesions. The pharmacokinetic properties of the probe are a contributing factor to the background noise and non-specific binding. Many dyes that are used for FGS are cleared from the body through the liver, which can result in a high level of background signal in the gastrointestinal tract. Further investigations to reduce background noise, as well as non-specific binding, are important for improving the accuracy and signal of FGS [105]. Finally, one of the biggest limitations of FGS is that it lacks the ability to image preoperatively in most cases, and it cannot image at all clinically relevant depths. It is essential to continue developing active targeting methods that can functionally integrate preoperative and intraoperative imaging, as well improve the signal to background ratio (SBR) for FGS.

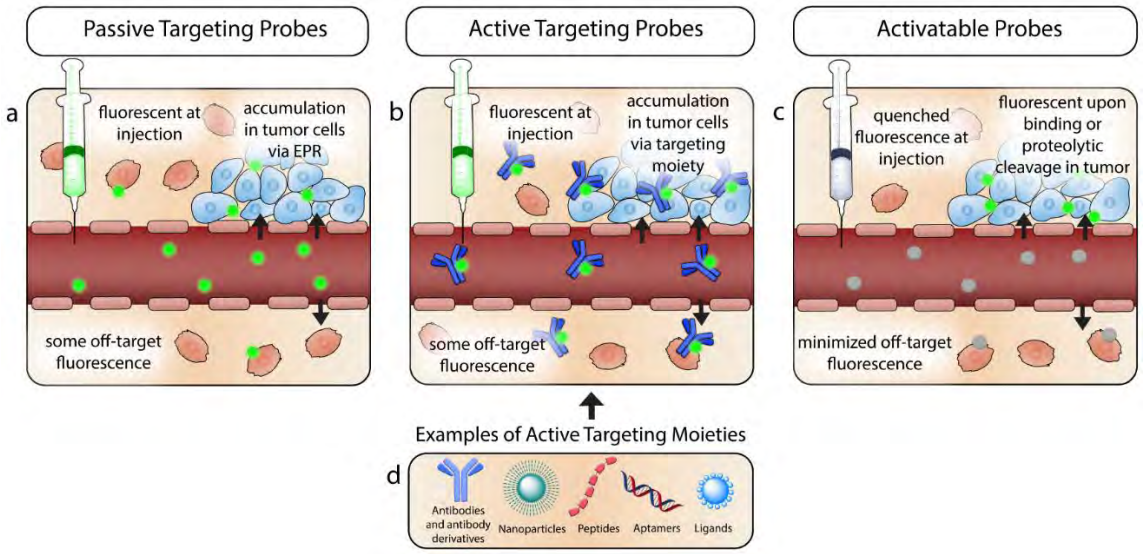

Figure 3: Tumor targeting strategies: **(A)** passive targeting relies on the selective accumulation of contrast agents in the tumor tissue, via leaky vasculature and absent lymph drainage. The contrast agents used in this targeting strategy are fluorescent at injection and can result in non-specific binding when the contrast agent is deposited outside the confines of the tumor. **(B)** Active targeting probes rely on a targeting moiety conjugated to a contrast agent to specify fluorescence. **(C)** Activatable probes exhibit quenched fluorescence when they are injected or topically applied. Binding to specific antigens or cleavage by a tumor protease results in the activation of these probes. Therefore, only cells that are targeted fluoresce. **(D)** There are many moieties available to use for active targeting, including but not limited to antibodies, antibody derivatives, nanoparticle scaffolds, peptides, ligands, and aptamers. (Originally published by Olson, Ly, and Mohs [5], reprinted with permission from © 2018, World Molecular Imaging Society)

1.3.1 Antibodies and Antibody Derivatives

The use of antibodies as an FGS-targeting strategy is widely investigated and, while the vast majority of these investigations for FGS are pre-clinical, several antibody-fluorophore conjugates are in clinical trials [106–109]. Cetuximab and Panitumumab, targeting human epidermal growth factor receptor (EGFR), and Bevacizumab, targeting vascular endothelial growth factor (VEGF), are common antibodies used for fluorescence imaging in current clinical trials for a variety of different cancers (NCT02583568, NCT02415881, NCT03134846) [62, 110]. In addition to imaging, antibodies have the potential to be useful tools for diagnostics, therapeutics, and drug delivery. However, the pharmacokinetic requirements differ for each of these uses [111, 112]. For instance, slow circulation is preferential for therapeutic antibodies, but fast clearance is necessary for imaging purposes. Therefore, dual function antibody probes must balance the requirements for its desired function. The binding sites of antibodies can be modified to achieve high specificity for a given target, a favorable trait for an imaging agent. However, antibodies have limitations in FGS. This is in part due to their large size (~150 kDa) and long circulation time, resulting in impaired tumor penetration and increased background signal during imaging. Engineered antibody fragments provide a compromise to full antibodies. Fragments are smaller in size (25-100 kDa), and therefore have faster clearance and decreased background signal during imaging, but sacrifice the extent of tumor uptake. These fragments have shown efficacy in recent studies of prostate cancer [113, 114]. Nanobodies and affibodies have also shown efficacy as alternatives to full antibodies. Affibodies, tiny protein scaffolds, are an advantageous alternative to full antibodies because of their small size (2-20 kDa), which allows for deeper tissue penetration, as well as their fast circulation time. These characteristics, in addition to their cheaper cost, make affibodies excellent candidates for imaging [115, 116]. An IRDye800CW-labeled synthetic affibody, ABY-029, has recently

demonstrated success in preclinical studies for labeling EGFR-positive regions in gliomas, and is currently undergoing microdosing clinical trials for multiple cancer types [117, 118]. Nanobodies (~12-15kDa) are typically constructed from the variable region of an antibody's heavy chain. The advantages of nanobodies are similar to affibodies in many regards, featuring high penetration and targeting, and rapid clearance [119, 120]. Recent trends in antibody-based targeting strategies for FGS may favor the smaller fragments and derivatives of antibodies rather than their fully assembled parents, because of their increased compatibility with imaging requirements.

1.3.2 Peptides

Peptides are linear or cyclic amino acid chains linked by peptide bonds. This type of probe is advantageous as an imaging agent because of rapid distribution, small size, ease and scalability of synthesis, specificity, and stability [121]. Despite their many advantages, peptides must be optimized in order to demonstrate translational potential. Their short half-life and degradation may prevent peptides from reaching their target. To combat this, peptides can be chemically modified to slow renal clearance and increase target affinity. Methods for modifying peptide probes for FGS have been previously described [122]. There is a wide variety of peptides being investigated in laboratory settings, including Arg-Gly-Asp (RGD), Somatostatin (SST), Gastrin releasing peptide (GRP) and Neurotensin (NT) among many others. In a recent study, a cyclic RGD-ZW800-1 was investigated as a generic tracer for multiple cancer types and proved to be efficacious for both tumor and ureter identification [123]. The use of a zwitterionic dye such as ZW800 can overcome problems with background noise in FGS. Because this dye is eliminated through renal filtration rather than liver clearance, studies have shown improved SBR and decreased background noise, especially in the gastrointestinal tract [105, 124]. Neurotensin conjugated to IRDye800 also showed value as a fluorescence imaging agent for potential use in screening pancreatic cancer patients [125]. Another

peptide probe of recent interest is the pHLIP-derived probe, or the pH low insertion peptide probe. This targeting strategy utilizes the characteristic acidic pH found in the tumor environment. The probe is designed so that upon sensing a change in pH, the probe is protonated and becomes more hydrophobic, thus folding and forming a transmembrane helix inserted in the membranes of the cancerous cells [126]. Recent studies have employed this technology for detecting bladder cancer and improving fluorescence signal in a breast cancer model [127, 128].

1.3.3 Aptamers

Aptamers are single stranded DNA or RNA sequences that are capable of binding to targets by forming three-dimensional structures. Aptamers are typically selected *in vitro* using a method called systematic evolution of ligands by exponential enrichment (SELEX), as well as variations on this technology. Explanations of aptamer selection using these libraries have been previously described [129, 130]. Aptamers have shown great potential for serving as a targeted probe for FGS because of the small size (5-40 kDa), ease of synthesis and modification, wide range of targets, and stability. Drawbacks to using these sequences as targeting agents for FGS are that aptamers are regularly degraded by nucleases, and not all aptamers have a high binding affinity. This can result in weak signal generation for imaging. However, this can be improved upon by using scaffolds, such as nanoparticles or quantum dots, to improve the binding affinity of the aptamer, thus providing increased specificity and enhanced signal [131]. A recent study demonstrated the efficacy of aptamer-conjugated quantum dots for identifying margins in glioma by binding to EGFR variant III on the tumor cell surface [132]. A different study employed the use of a silica-based nanoparticle and aptamer conjugate to act as a theranostic agent to image and inhibit tumor angiogenesis [133]. Beyond FGS, aptamers have shown great potential for use in a variety of applications, especially in drug delivery. Aptamers are prevalent in clinical trials, but not yet in relation to FGS.

Most of the current clinical trials investigate aptamer use in macular degeneration, though recently posted clinical trials propose identifying aptamers to identify biomarkers in bladder cancer (NCT02957370), as well as using a Ga68-aptamer conjugate to test its diagnostic capabilities in PET/CT (NCT03385148).

1.3.4 Ligand-Based Targeting

There are several ligand-based targeting strategies that are typically used to functionalize and specialize the surface of nanoparticles. Two commonly explored examples of this strategy include proteins like transferrin, and small molecules such as folic acid. Small molecules are advantageous as a targeting strategy because of their size, cost, and stability. However, they are scarce because of the difficulty of finding a ligand, and the intense screening process involved [77, 134]. These molecules are typically used to functionalize the surface of nanoparticles for more specific targeting. Folic acid is perhaps the small molecule most commonly reported in the literature as useful for functionalization. Folic acid-conjugated quantum dots have proved successful as a theranostic agent in human cervical carcinoma cells [135]. Additionally, OTL38, a folate receptor-targeted contrast agent, has shown success in multiple cancer models [136, 137]. A recent study used a folate-targeted contrast agent to identify lung cancer in large animal models [138]. Protein ligand-based strategies, such as transferrin, are advantageous in their specificity, but present problems because of bulk and ability to trigger an immune response. A recent study described the use of holo-transferrin ICG nanoassemblies for imaging and photothermal therapy in gliomas [139].

1.3.5 Improving Active Targeting

Despite the wide variety of targeting ligands explored in pre-clinical studies, there are still many limitations to active targeting for FGS. While active targeting exhibits

increased specificity of the probe for its target, non-specific binding still occurs, as shown in **Figure 3**. Active probes constantly emit fluorescence with excitation, regardless of their proximity to the target, producing elevated background noise in FGS [140, 141]. Additionally, off-target binding can occur if the targeted receptor is expressed in non-cancerous tissues. While each type of targeting strategy has its own strengths and weaknesses, there are several widely adapted strategies to improve the efficacy of these probes, including the use of nanoparticles and activatable probes. Nanoparticles may play a significant role in FGS, especially in acting as a scaffolding system for many of the aforementioned targeting strategies. The large surface area to volume ratio of nanoparticles provides a large area to attach a wide range of targeting moieties. However, the long-term effects of nanoparticle administration are still not fully understood. Biocompatibility, biodegradability and toxicity properties must be carefully considered on a case-by-case basis [142]. Nanoparticle size, shape, charge, and hydrophobicity can all influence the conjugation with a ligand [77]. Using a nanoparticle as a scaffold for a targeting ligand allows for multiple interactions, and thus increased specificity with the target. Nanoparticle-entrapped dyes have shown enhanced fluorescence and tumor contrast, and nanoparticles are effective carriers for drug delivery [58]. Previous studies have also shown that careful modification of nanoparticle size and surface coating can alter their biodistribution to favor renal filtration, allowing for increased SBR and decreased background noise [143]. Further investigation of nanoparticle modifications to alter the pharmacokinetic properties has the potential to improve the detection capabilities of FGS. Given their functionality, current research for FGS has demonstrated increased use of nanoparticles for more effective delivery, as well as brighter contrast.

There are two main categories of active targeting probes: ‘always on’ probes, and ‘activatable’ probes. Activatable probes offer several advantages over probes that

are always on, such as higher contrast, lower background noise, and improved sensitivity. As shown in **Figure 3**, the fluorescent properties of these probes remain quiescent until they receive a signal to fluoresce, such as enzymatic cleavage or cellular internalization. Probes such as these that are activated by biomolecules in the local tumor environment have the potential to overcome some of the pitfalls of FGS, such as background noise and low SBR, by eliminating non-specific binding and subsequent off-target fluorescence. Difficulties with implementation of these probe types depend on the specifics of the probe. High molecular weight activatable probes cannot be sprayed onto the surface of the tumor and must be injected intravenously. It may take days for the necessary tumor to background ratio to be achieved. Molecular binding-based activatable probes are typically conjugated to an antibody and are therefore significantly large in size. However, enzymatic activity-controlled probes can be small in size, and therefore some can be applied with a spray [140]. The use of a matrix metalloprotease, and γ-glutamyltranspeptidase as agents for inducing probe enzymatic cleavage and activating fluorescence have been recently explored for cancer detection [144].

Many of the aforementioned active targeting mechanisms have potential applications in the field of drug delivery, as well as FGS. For instance, antibody drug conjugates are being utilized in both preclinical studies as well as early and late-stage clinical trials. These studies have shown increased ability to target diseased cells and increased antitumor potency [145–148]. Peptide and aptamer-based delivery systems have also shown efficacy in reducing off-target effects and increasing drug delivery to the tumor [149–151]. Therefore, there is an opportunity for parallel development of imaging probes and drug delivery systems that target the same receptor or biomarker. Furthermore, there is an opportunity to improve active targeting by incorporating multimodality imaging probes. One of the biggest limitations with FGS is that it can only be used intraoperatively, and cannot be used for preoperative planning. However

multimodal active targeting probes that use FGS in conjunction with Magnetic Resonance Imaging (MRI), Positron Emission Tomography (PET), Photoacoustic Imaging (PAI), or Computed Tomography (CT) can potentially improve preoperative detection, and intraoperative resection [152–160]. Current multimodal probes employ many of the active targeting strategies to achieve a high level of accuracy for probe delivery and overcome some of the limitations of single modality active targeting.

While the variety of targeted probes continues to expand in versatility and function, regulatory restrictions are significant considerations into successful implementation into clinical settings. In addition, each type of probe comes with its own set of developmental difficulties. Given the wide successes of different types of probes in the laboratory, it seems that there is not one type of probe that exceeds all others in terms of clinical potential. Instead, the functional imaging and targeting requirements should dictate the type of probe used, as each carry its own advantages. Further toxicity and feasibility studies, as well as appearance in clinical trials are needed to progress targeted probes for FGS into routine clinical usage.

1.4 In Vivo *vs.* Ex Vivo Imaging

Surgical resection of tumors typically consists of three components. The primary tumor is assessed before the initial resection, the surgical margin is analyzed for remaining tumor, and the surgical field is assessed for regional metastasis [161]. As mentioned previously, remaining tumor at the surgical margin can result in disease recurrence. There are several strategies available to analyze the surgical margin for the presence of microscopic disease to achieve negative margins. Two common methods for intraoperative pathological examination of the surgical margin include intraoperative frozen section analysis (IFSA) and imprint cytology. Both methods have demonstrated reduced rates of positive margins after surgery, but the technology has limitations. IFSA, the current gold standard in margin detection, is highly variable in terms of sensitivity,

and requires confirmation of negative margins on multiple tissue samples by a pathologist, which can add significant time onto the surgical procedure [162–164]. Imprint cytology is a faster and more cost-effective method of analysis in comparison to IFSA. However, it also has variable levels of sensitivity, and has a high probability of false-negative results [165]. The use of fluorescence imaging is increasingly being considered as an alternative method of histological analysis. Typically, FGS is associated with intravenous administration of contrast agents for tumor detection, as the advantages of intraoperative real-time feedback of the surgical field are evident. However, significant investigations of fluorescent probe toxicity, dosage, optimal imaging time, and accuracy of molecular targeting must be conducted and approved before this technology can become the standard of care for eligible cancer patients.

As an alternative use of FGS, recent studies have demonstrated the use of *ex vivo* contrast agent administration to perform real-time fluorescence guided histology [41, 166–168]. This technique lacks some of the intraoperative advantages such as preventing excessive tissue resection but avoids some of the rigorous regulatory approval and testing, while still providing critical feedback on margin and nodal status. *Ex vivo* techniques are particularly useful for sentinel lymph node and positive margin detection. This strategy is efficacious and avoids extended operating time and potentially re-excision. A recent study employed dual probe difference specimen imaging to differentiate between tumor and benign tissue using both a targeted and a non-targeted probe, as shown in **Figure 4** [166]. *Ex vivo* analysis provides an opportunity to utilize many of the targeted probes being developed in the labs into the clinic without extensive regulatory hurdles.

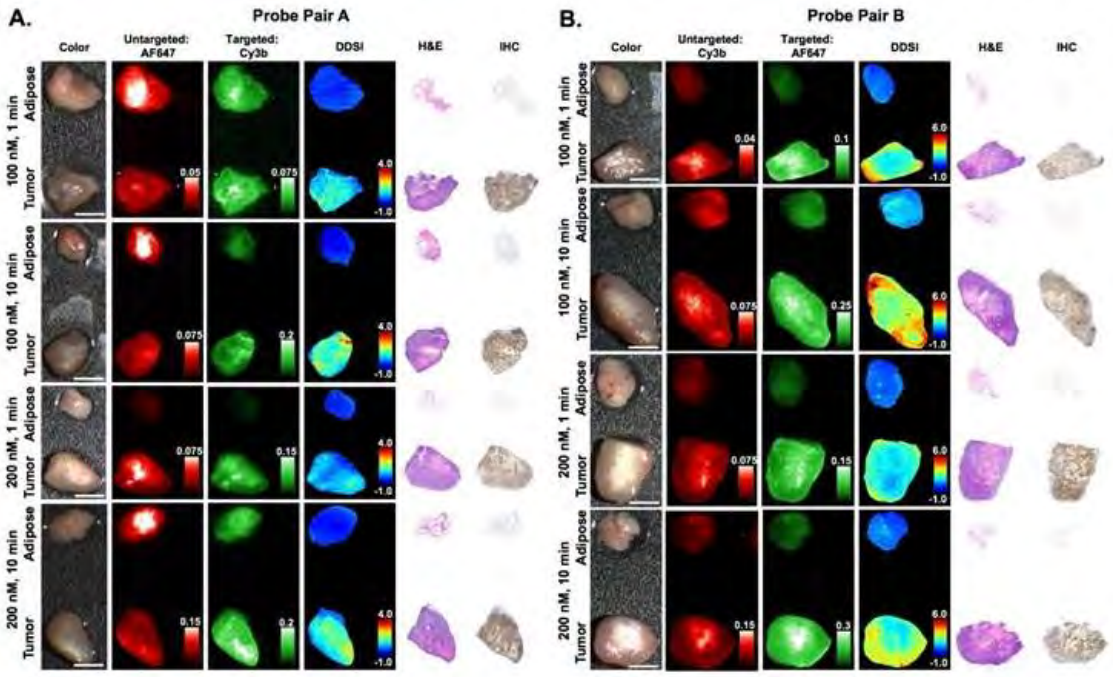

Figure 4: Dual probe ex vivo specimen imaging: representative color, fluorescence, DDSI (dual probe difference specimen imaging), H&E, and HER2-targeted IHC images of tumor and adipose tissue pairs following staining using a range of dual-stain soak concentrations and incubation times for a probe pair A (Herceptin-Cy3b, DkRb-AF647) and probe pair B (HerceptinAF647, DkRb-Cy3b). All images are representative of data collected for n = 6 tumor and adipose tissue pairs per staining condition. All untargeted and targeted channel images are background corrected, normalized by their exposure time and calibration drop intensity. DDSI images are displayed with equivalent color scales across staining conditions. H&E and IHC images were acquired from serial sections of the same tissue face imaged in the whole specimen DDSI images. H&E, hematoxylin and eosin; IHC, immunohistochemistry. Scale bars = 5 mm. Adapted with permission from [166], © Ivyspring International Publisher, 2017.

1.5 Clinical Translation

The number of new clinical trials involving FGS has increased dramatically over the past decade [169]. The adoption of target-specific probes and NIR dyes requires strict regulatory review to ensure patient safety. To fulfill these regulatory requirements, many current clinical trials are centralized around investigating the safety and efficacy of the FGS agents. The majority of clinical trials for FGS are Phase 1 and Phase 2 trials, though there are several agents that have progressed to Phase 3 trials [170]. Endpoints to developing successful contrast agents, devices, and procedures need to be well-defined in order to see faster progress of FIGS into patient care [171]. Current clinical trials for FIGS vary widely in terms of contrast agent, device, ligand conjugation, and objective, as shown in **Table 2**. While many current clinical trials still employ free dye, there are increasing numbers and diversity of probes that utilize targeting moieties for imaging, including antibodies, proteins, affibodies, nanoparticles, peptides, and small molecules [170]. ICG remains the most prominent contrast agent used in clinical trials, which is unsurprising due to its low toxicity and current FDA approval status. ICG is also significantly less expensive than other available contrast agents. SLN detection is currently under investigation for many cancer types with ICG, and there are some intriguing implementations of new technology. For example, in a fluorescence imaging study for multiple cancer types, the use of a hands-free goggle system is being explored as an alternative to traditional monitor display FIGS devices as shown in **Figure 5** (NCT03297957, NCT02807597, NCT02316795, NCT04105062) [172, 173]. IRDye800 has become another prominent contrast agent on the clinical trial stage. This dye is used in conjugation with several different antibodies across the spectrum of clinical trials including panitumumab, cetuximab, and bevacizumab, allowing for theoretically more precise tumor localization. Besides antibody conjugated-IRDye800, there are several clinical trials studying IRDye800 conjugated to peptides. Recently a synthetic protease-activated peptide dye conjugate entitled AVB-620, has entered a Phase 2 trial for tumor

and lymph node metastasis detection. Additionally, an anti-EGFR IRDye800 labeled affibody peptide has completed early Phase 1 trials in patients with recurrent gliomas, head and neck cancers, and soft tissue sarcomas (NCT02901925, NCT03282461, NCT03154411). A Phase 1/2 study is beginning to investigate multimodality imaging to combine SPECT/CT with FIGS (NCT03699332). While FIGS has become widely investigated across clinical trials for adults, the implementation of FIGS for the pediatric cancer population is still in its infancy [174, 175]. However, several trials have been newly initiated to investigate several imaging agents (ICG, BLZ-100, and panitumumab-IRDye800) for solid tumors, central nervous system tumors and brain tumors in the pediatric population (NCT04084067, NCT03579602, NCT04085887 respectively).

Four targeted probes have progressed to Phase 3 clinical trials and shown potential as prominent candidates for FGS and cancer detection: Surgimab (SGM-101), LUM015, OTL38, and BLZ-100. SGM-101 is a fluorescent anti-carcinoembryonic (CEA) monoclonal antibody probe. A Phase 1 trial for colon, rectal, and pancreatic cancer has been completed (NCT02973672), and results suggested that the SGM-101 probe was safe and efficacious in detecting cancer [176]. Furthermore, a clinical trial investigating SGM-101 for use in detecting peritoneal carcinomatosis was recently completed (NCT02784028). Additional Phase 1 and 2 trials have been initiated with SGM-101 for pulmonary nodules (NCT04315467), colorectal brain metastases (NCT04755920), and colorectal lung metastases (NCT04737213). A Phase 3 study has also been initiated for investigating the performance of SGM-101 for colorectal tumors (NCT03659448), and a Phase 2/3 study is evaluating SGM-101 in rectal cancer (NCT04642924). LUM015 is a targeted probe which contains a Cy5 fluorophore linked to a cathepsin activatable peptide. LUM015 and the LUM imaging system have completed Phase 1 and 2 trials for soft tissue sarcoma and breast cancer (NCT02438358, NCT03321929, NCT01626066). Currently, LUM015 is in active trials for the detection of prostate cancer, brain cancer,

and peritoneal surface malignancies (NCT03441464, NCT03717142, NCT03834272). A Phase 2 trial for breast cancer patients after neoadjuvant therapy, a trial for feasibility for pancreatic cancer detection, a Phase 1/2 study for detection of gastrointestinal cancers, and a Phase 3 study for breast cancer are all currently recruiting patients (NCT04440982, NCT04276909, NCT02584244, NCT03686215). OTL38 is a folate-receptor-targeted fluorescent moiety that has completed a study for application in renal cell carcinoma (NCT02645409), a Phase 2 study for imaging a folate receptor-positive lung nodules (NCT02872701), a study for solid tumors (NCT02852252), as well as Phase 2 and Phase 3 studies for ovarian cancer during cytoreduction, interval debulking, or recurrent surgeries (NCT02317705, NCT03180307). Ongoing and upcoming trials include a Phase 1 study for ovarian cancer, which investigates a single dose of OTL38 and compares camera imaging systems to better determine sensitivity and positive prediction value of the probe (NCT04941378). A Phase 1 study for intraoperative identification of pulmonary nodules (NCT02602119), and a Phase 3 study to determine efficacy of OTL38 in detecting lung cancer are also currently recruiting (NCT04241315). BLZ-100, also known as ‘tumor paint’ or tozuleristide, is a probe made up of the peptide chlorotoxin and ICG. Phase 1 trials have been completed for skin neoplasms, solid tumors, pediatric central nervous system (CNS) tumors, and gliomas (NCT02097875, NCT02496065, NCT02462629, NCT02234297). Initial results of several of these studies demonstrate the safety and feasibility of BLZ-100 as a fluorescent probe [177]. The success of these probes in progressing to later phase clinical trials and the significant increase in clinical trials for FIGS for many tumor types overall suggests the potential for clinical implementation in the future.

Table 2: Representative Clinical Trials for FGS

Imaging Agent	Disease Indication	Clinical Trials Identifier			
		Unlisted Phase	Phase 1	Phase 2	Phase 3+

5-ALA	Brain Cancer			NCT04738162	
		NCT02379572			
		NCT04556929			
		NCT04712214			
		NCT04780009			
					NCT04937244
		NCT04055688			
		NCT02632370			
			NCT00870779		
			NCT02473380		
			NCT02755142		
			NCT01128218		
				NCT01310868	
				NCT00752323	
					NCT00241670
					NCT01167322
		NCT01445691			
	Meningioma				NCT04305470
	Pituitary Carcinoma	NCT04390802			
	Breast Cancer				NCT04815083
				NCT01837225	
ICG	Lung, Esophageal, and Gastric	NCT04734821			
		NCT03931044			
		NCT04400292			
		NCT04943484			
		NCT01034670			
			NCT04173676		
			NCT02570815		
			NCT02611245		
	Melanoma	NCT02142244			
			NCT01295931		
			NCT01121718		
	Head & Neck	NCT03021200			
				NCT04842162	
		NCT03297957			
			NCT03745690		
	Breast Cancer	NCT04438577			
		NCT03619967			
					NCT03200704
					NCT03294330
					NCT02279108
		NCT02419807			
		NCT01468649			
			NCT02316795		
			NCT02027818		
		NCT02802553			
	Colon Cancer	NCT04220242			
		NCT04351009			
		NCT04207489			
				NCT01662752	
				NCT02850783	
	Gynecological	NCT04972682			
		NCT04514289			
		NCT04663412			
		NCT04224467			
					NCT02598219
					NCT04878094
		NCT02209532			
		NCT01562106			
		NCT02068820			
		NCT02131558			
		NCT01818739			

		NCT01673022			
	Brain Cancer		NCT03262636		
	Pediatric Solid Tumors		NCT04084067		
	Thyroid	NCT04424485			
	Sarcoma			NCT04719156	
	Peritoneal mets	NCT04352894			
				NCT02032485	
	GI stromal cell			NCT04761172	
	Kidney		NCT01281488		
	Liver		NCT01738217		
	Prostate				NCT04882618
			NCT02119858		
IRDye800					
Cetuximab-IRDye800	Rectal Cancer		NCT04638036		
	Esophageal		NCT04161560		
	Head and Neck		NCT03134846		
			NCT01987375		
	Pancreatic			NCT02736578	
Bevacizumab-IRDye800	Sinonasal Inverted Papilloma		NCT0392585		
	Pituitary Tumors		NCT04212793		
	Colorectal Cancer	NCT04101292			
			NCT01972373		
	Esophageal		NCT03558724		
				NCT03877601	
			NCT02129933		
	Cholangiocarcinoma		NCT03620292		
	Breast Cancer		NCT02583568		
			NCT01508572		
	Pancreatic Cancer		NCT02743975		
Panitumumab-IRDye800	Lung Cancer		NCT03582124		
	Pancreatic cancer		NCT03384238		
	Pediatric Neoplasms		NCT04085887		
	Glioma		NCT03510208		
	Head and Neck		NCT03733210		
				NCT04511078	
			NCT02415881		
Nimotuzumab-IRDye800	Lung Cancer		NCT04459065		
Indium-111-Dota-Labetuzumab-IRDye800	Colon cancer and peritoneal mets		NCT03699332		
ABY-029	Glioma		NCT02901925		
	Head and Neck		NCT03282461		
	Soft Tissue Sarcoma		NCT03154411		
Other					
cRGD-ZW800-1	Oral Cancer			NCT04191460	
ONM-100	Solid Tumors			NCT03735680	
	Peritoneal Mets			NCT04950166	
SGM-101	Colorectal, Pancreas			NCT04642924	
					NCT03659448
				NCT04737213	
				NCT04755920	
			NCT02973672		
	Peritoneal Mets	NCT02784028			
	Lung		NCT04315467		
LS301	Breast Cancer		NCT02807597		
	Liver, Pancreatic, gastric		NCT04105062		
LUM015	Prostate	NCT03441464			
	Brain	NCT03717142			
	Peritoneal Mets	NCT03834272			
	Colon, Pancreatic, Esophageal, Gastric		NCT02584244		
		NCT04276909			
	Sarcoma		NCT01626066		
	Breast				NCT03686215
				NCT04440982	

		NCT02438358			
				NCT03321929	
OTL38	Ovarian		NCT04941378		
				NCT02317705	
					NCT03180307
	Renal Cell Carcinoma	NCT02645409			
	Lung		NCT02602119		
					NCT04241315
				NCT02872701	
	Bladder, Gastric	NCT02852252			
	Pituitary Carcinoma		NCT02629549		
BLZ-100	CNS Tumors			NCT03579602	
			NCT02234297		
			NCT02462629		
	Solid Tumors		NCT02496065		
	Skin		NCT02097875		
PARPi-FL	Oral Cancer		NCT03085147		
AVB-620	Breast			NCT03113825	
HS-196	Solid Tumors		NCT03333031		
EMI-137	Esophageal		NCT03205501		
	Thyroid Cancer		NCT03470259		

Legend: green = recruiting, actively recruiting or active; blue = completed; red = terminated or suspended

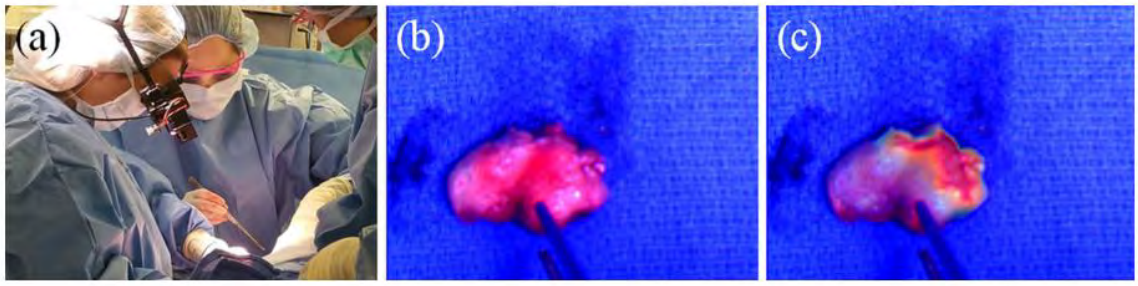

Figure 5: Goggles used for FIGS and cancer detection: fluorescence-guided SLN biopsy. **(A)** The surgeon wearing the goggles during SLN visualization in a breast cancer patient. **(B)** The color image of the excised SLN. **(C)** The superimposed colorfluorescence image of the excised SLN as seen by the surgeon. Adapted with permission from [173], Copyright © 2017, Society of Surgical Oncology.

1.6 Opportunities in Image-Guided Surgery

FGS has emerged as an imaging technology with significant potential for clinical efficacy, especially in the field of surgical oncology. Despite its progress, there are still many opportunities for growth in the field. Given below are a few potential examples:

- **Multimodal imaging:** Using a combination of several imaging modalities to diagnose a patient increases diagnostic accuracy. Several recent studies investigated the use of targeted nanoparticles for MRI and FGS, providing the surgeon concurrence between preoperative planning and intraoperative resection [178, 179]. Combining photoacoustic imaging with FGS is another area of interest for multimodal imaging [180]. It has been demonstrated that the use of multiple imaging modalities has a synergistic effect on the ability to detect and differentiate cancer both preoperatively and intraoperatively [181].
- **Photodynamic therapy:** FGS has theranostic capabilities, especially with using NIR contrast agents to induce an immune, chemical, or thermal response in cancer cells. Recent photoimmunotherapy to induce immunogenic cell death with an antibody-conjugated NIR dye has demonstrated an interesting theranostic path to further investigate [182, 183]. Moreover, early studies have begun to explore photodynamic therapy and photothermal therapy as combined imaging and therapy strategies for cancer treatment [184, 185] (**Figure 6**).

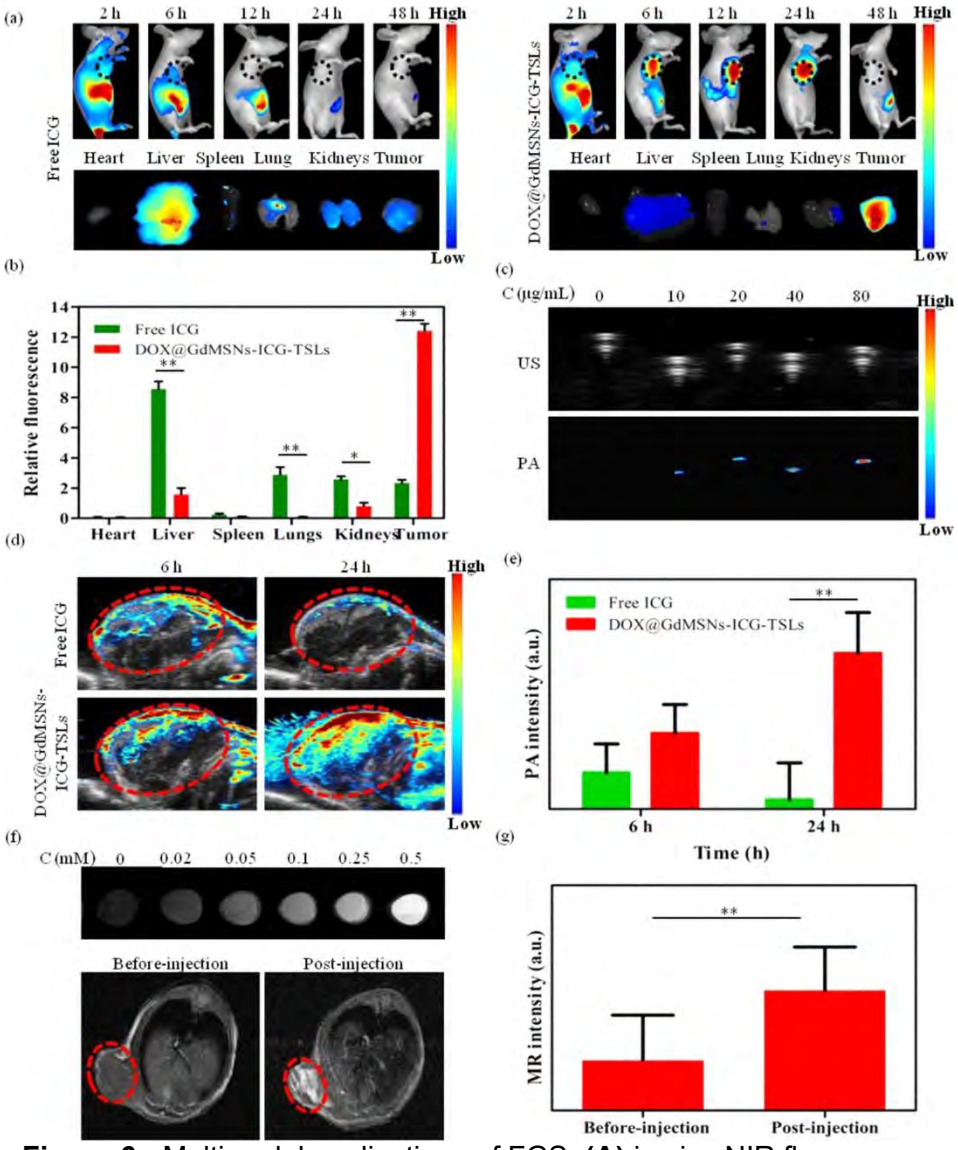

Figure 6: Multimodal applications of FGS: **(A)** in vivo NIR fluorescence images after intravenous injection of free ICG and DOX@GdMSNs-ICG-TSLs in tumor-bearing mice at 2, 6, 12, 24, and 48 h, and the corresponding fluorescence images of different tissues after treated with free ICG and DOX@GdMSNs-ICG-TSLs at 24 h. **(B)** Relative fluorescence intensity of ICG in major organs induced by 808 nm laser (1.5 W/cm2) irradiation at 24 h after i.v. administration. **(C)** US and PA images of DOX@GdMSNs-ICG-TSLs at various concentrations of ICG. **(D)** PA images of tumor-bearing mice after 6 and 24 h intravenous injection via tail of free ICG and DOX@GdMSNs-ICG-TSLs, respectively. **(E)** PA intensity of tumor sites after treatment with free ICG and DOX@GdMSNs-ICG-TSLs at 6 and 24 h. **(F)** T1-weighted MR images (7 T, spin–echo sequence; repetition time, TR = 500 ms; echo time, TE = 14.92 ms) of DOX@GdMSNs-ICGTSLs nanoparticles at various Gd concentrations. And T1- weighted MR images of tumor-bearing mice before and after injected with DOX@GdMSNs-ICG-TSLs for 24 h. **(G)** Relative MR intensity before and after injecting DOX@GdMSNs-ICGTSLs. Data are presented as means ± SD (n = 5); *P G 0.05, **P G 0.01. Adapted with permission from [184], © 2018 American Chemical Society.

- **NIR II window:** Typical NIR probes fall in the range of 700-1000 nm, whereas NIR-II agents emit in the 1000-1700 nm range. This shift in emission spectra has demonstrated deeper light penetration depths as well as higher contrast. These preliminary successes suggest a need for further NIR-II probe development [186, 187].
- **Nanotechnology:** Nanotechnology continues to play a key role in FGS, and offers significant opportunities in terms of conjugation, targeting, and dye encapsulation for enhanced FGS and multimodality performance. Current research has begun to explore the use of biodegradable nanoparticles for imaging and therapy in cancer treatment [188, 189]. Success in these experiments tackles the concern of toxicity of non-biodegradable nanoparticles, strengthening their potential for translation. [150, 151].
- **Refinement of Imaging Probes:** Further refinement of contrast agents and bulky passive, active, and activatable probes for FGS is essential to provide the precision and clarity necessary for clinical translation.
- **Applications in advanced cancer models:** In order to apply FGS technology to highly metastatic and advanced cancers like pancreatic and ovarian, the discovery of early detection biomarkers to target is of utmost importance. Furthermore, the use of large animal models and comparative studies on companion animals as part of standard veterinary treatment may be beneficial.

In the interest of providing the most comprehensive and precise patient care, FGS may eventually align with the implementation of highly personalized medicine. The future of FGS may involve isolating specific cancer biomarkers for a patient, and selecting the corresponding targeted fluorescence probe that would most effectively detect their cancer and metastases. Increased probe specificity and functionality would allow for more complete and thus potentially curative surgical resections for many cancer types.

Though many opportunities for growth in the field still exist, FGS has the potential for widespread implementation as a critical tool for improving surgical resection of cancer.

Chapter 2: Development and Investigation of AR9.6-IRDye800 for PDAC

This chapter is adapted from a previous publication by Olson, Wojtynek, et al. Reprinted with permission from [190], © 2020, American Association for Cancer Research.

2.1 Introduction

Pancreatic ductal adenocarcinoma (PDAC) remains a highly lethal and aggressive disease, characterized by its poor response to therapy, and advanced stage of disease at diagnosis. Surgical resection is currently the only curative option for patients with this disease [191, 192]. However, difficulties in differentiating between cancerous and non-cancerous tissue result in high rates of R1 resections, or resections with positive margin involvement, and thus high rates of recurrence [193, 194]. Pathological determination of resection status is defined by a minimum of a 1 mm tumor-cell free margin between the closest cancer cell and all resection margins to achieve a complete resection, or an R0 resection [195]. Patients who undergo a complete R0 resection have improved survival compared to R1 resections, which exemplifies the importance of comprehensive intraoperative tumor detection and resection [196]. While preoperative imaging modalities play a critical role in initial staging, detection, and surgical planning, translating these images into an intraoperative setting can be challenging, leading to missed lesions [197]. Thus, the 5-year survival rate for patients that undergo surgical resection is only approximately 25% [191]. Fluorescence-guided surgery (FGS) has emerged as a method to reduce irradical resections and improve intraoperative assessment of lesions [35]. FGS relies on the preferential accumulation of a contrast agent in tumors, to differentiate malignant tissue from adjacent non-cancerous tissue with fluorescence. The implementation of FGS has the potential to improve outcomes of pancreatic cancer resections by improving the detection of the primary tumor, surgical margins, and residual disease [198]. While FGS has clear potential for improving surgery in resectable cases, image guidance could also be employed to

prevent unnecessary surgeries in unresectable cases, by highlighting metastatic lesions that have been missed in initial staging.

Near-infrared (NIR) dyes are preferentially employed for FGS because they exhibit low autofluorescence, reduced light scattering, and improved depth of penetration [28, 70]. These properties are critical, particularly in malignancies like pancreatic cancer, where the tumor is often deeply seated in the abdominal cavity. FGS systems required to visualize fluorophores intraoperatively have been extensively reviewed here [74]. A wide variety of targeting vehicles have been developed preclinically and in clinical trials to direct contrast agents to specific tumor targets, or tumor phenotypes, resulting in improved contrast agent specificity [5]. Antibodies have been frequently used, particularly in clinical trials, because the high stability and target specificity, potentially low toxicity, and well-established conjugation strategies are favorable for probe development [112, 199].

Current clinical trials in pancreatic cancer are investigating fluorescent antibody conjugates that target epidermal growth factor receptor (EGFR), vascular endothelial growth factor (VEGF-A), and carcinoembryonic antigen (CEA) for FGS [3, 200]. These initial clinical trials have demonstrated feasibility in delineating primary and metastatic disease. However, these studies also suggest the need to identify and expand alternative targeted probes to address the heterogeneity of biomarkers present in pancreatic tumors and improve intraoperative imaging [200]. To address this problem, we investigated a new potential target for FGS in pancreatic cancer.

MUC16, also known as CA125, is overexpressed in 60–80% of pancreatic cancer [201]. MUC16 is overexpressed in many different cancers, including colon, stomach, and esophageal, but has been most widely studied for its aberrant expression in ovarian cancer [201, 202]. Recent studies in pancreatic cancer have demonstrated

that MUC16 expression is positively correlated to disease progression and poor prognosis [203, 204]. While MUC16 has shown promise as a prognostic and diagnostic biomarker for pancreatic cancer, it has not yet been investigated for FGS. Thus, the goal of this work was to develop a MUC16-targeted antibody probe that could achieve optimal delivery to identify pancreatic cancer intraoperatively with FGS. To achieve this, we utilized AR9.6, a monoclonal antibody (mAb) that targets isoforms of MUC16 (either fully glycosylated or aberrantly glycosylated). We hypothesized that targeting MUC16 with the AR9.6 fluorescent antibody probe would improve the detection of pancreatic cancer and provide strong contrast against surrounding tissue. In this study, we employ the antibody AR9.6, conjugated to the near infrared dye, IRDye800 to target pancreatic cancer. Our findings demonstrated strong fluorescence enhancement of pancreatic tumor xenografts with the AR9.6-IRDye800 probe and suggested the potential utility of this fluorescent probe for improved intraoperative imaging of pancreatic cancer.

2.2 Materials and Methods

2.2.1 Antibody Conjugation

Mouse AR9.6 (Quest PharmaTech, Inc., Edmonton, Canada) and mouse IgG1 isotype (ThermoFisher Scientific, 02-6100; Waltham, MA) antibodies were reconstituted to 1 mg/ml in phosphate-buffered saline (PBS). A Zeba™ spin desalting column (ThermoFisher Scientific, 89891) was used to remove 0.1% sodium azide from the IgG1 antibody. Mouse AR9.6 did not contain sodium azide. 100 µl of 1M potassium phosphate was added to each mg of antibody to raise the pH to 8.5. IRDye800 N-hydroxysuccinimide (NHS) ester (0.5 mg, LI-COR Biosciences, 929-70020; Lincoln, NE) was dissolved in 50 µl of nanopure water, and vortexed briefly. 10 µl of the dye was added to 1 mg of antibody, and vortexed briefly to mix. Dye and antibody were incubated for 2 h at room temperature. Zeba™ spin desalting columns were used to remove excess dye, according to the instructions from the manufacturer. A 1 cm cuvette

(Eppendorf, E0030106300; Hauppauge, NY) was loaded with a 1:10 dilution of the antibody in a 1:1 ratio of PBS and methanol. A Thermo Scientific Evolution 220 UV-visible spectrophotometer was used to determine dye: protein ratio (D/P), such that $\frac{D}{P} = \left[\frac{A_{780}}{\varepsilon_{Dye}}\right] \div \left[\frac{A_{280}-(0.03 \times A_{780})}{\varepsilon_{Protein}}\right]$, where ε_{Dye} = 270,000 M^{-1} $cm^{-1}$and $\varepsilon_{Protein}$ = 203,000 M^{-1} cm^{-1}. The concentration of the antibody after conjugation was determined such that $\left(\frac{mg}{ml}\right) = \left[\frac{A_{280}-(0.03 \times A_{780})}{\varepsilon_{Protein}}\right] \times MW\ protein \times Dilution\ factor$. Conjugation resulted in an average of 3 dyes per antibody. The emission of the antibody conjugates was determined using a FluoroMax 4 spectrofluorometer (Horiba Scientific; Irvine, CA).

2.2.2 Cell Culture

Pancreatic cancer cell lines acquired 2/2018 including HPNE (CVCL_C466), Colo357 (CVCL_0221), T3M4 (CVCL_4056), Capan1 (CVCL_0237), CFPAC (CVCL_1119), and HPAC (CVCL_3517) were obtained from Dr. Michael A. Hollingsworth, and OVCAR3 (CVCL_0465) cells acquired March 2018 were obtained from Dr. Adam R. Karpf. Cells were last tested for mycoplasma on March 21, 2018, using a PCR mycoplasma detection kit (ABM, G-238; Vancouver, CA). All cells were grown in RPMI 1640 (Corning, 10–040-CV; Tewksbury, MA), supplemented with 10% fetal bovine serum, 100 I.U./ml penicillin, and 100 µg/ml of streptomycin (P/S) (Corning, 30–002-CI). Cells were maintained at 37° C in a humidified incubator with 5% CO2. In general, all cells were passaged fewer than 20 times, or for no more than one month after thawing before experimental use.

2.2.3 Western Blot

Cells were lysed with radioimmunoprecipitation assay (RIPA) buffer (ThermoFisher Scientific, 89900) supplemented with Halt protease inhibitor (ThermoFisher Scientific, 78440). 25 µg of protein were separated on a 4–15%

polyacrylamide gel (Bio-Rad, 4568084; Hercules, CA) and transferred onto a nitrocellulose membrane (Bio-Rad, 1620115). The membrane was blocked with 5% Blotting-Grade Blocker (Bio-Rad, 170–6404) in Tris-Buffered Saline and Polysorbate 20 (TBST) and incubated with AR9.6 (1:1000, 1mg/ml stock solution) and GAPDH antibody (1:2000, Cell Signaling Technology, 2118S; Danvers, MA) overnight at 4° C. The membrane was incubated with goat-anti mouse HRP secondary antibody (1:2000, Jackson Immunoresearch, 115–035-003; West Grove, PA), or goat-anti rabbit HRP secondary antibody (1:2000, Jackson Immunoresearch, 111–035-003) in 5% Blotting-Grade Blocker for 1 h on a rocker and was visualized with enhanced chemiluminescent (ECL) substrate (Bio-Rad, 1705060S).

For fluorescent western blotting, the membrane was blocked with 5% blotting grade blocking buffer in TBS. AR9.6-IRDye800 (1:5000 1mg/ml stock solution) and IgG-IRDye800 (1:2500 0.5 mg/ml stock solution) were incubated with the membrane overnight at 4 °C in 5% blotting grade blocker in TBST. After washing, the membrane was incubated with goat anti-mouse IRDye800 (1:20,000, LI-COR Biosciences, 926–33210) in 5% blotting grade blocker in TBST, washed, and imaged on an Odyssey CLx (LI-COR Biosciences).

2.2.4 Immunofluorescence

HPNE, Colo357, T3M4, and OVCAR3 cells were seeded at 30,000–40,000 cells per chamber of an 8-chamber slide (ThermoFisher Scientific, 154534), and allowed to adhere overnight. Cells were washed 3x with 1X PBS and fixed in ice-cold methanol at −20° C for 20 min. After fixation, cells were washed with 1X PBS and blocked with 3% bovine serum albumin (BSA) in TBS for 1 h at room temperature. 5 µg/ml of AR9.6 and 5µg/ml of IgG1 were incubated with cells for 1 h at room temperature in 3% BSA in TBST. Cells were washed 3x with PBS. Fluoroshield mounting medium with 4’,6-diamidino-2-phenylindole (DAPI) (Abcam, ab104139; Cambridge, MA) was added to

cover each chamber, and chambers were covered with a glass coverslip. Cells were imaged at 400X magnification on an Olympus DP80 Digital Camera and cellSens Dimension software.

2.2.5 Antibody Internalization

Colo357 cells were seeded as indicated above. Cells were incubated with AR9.6-IRDye800 for 1 hour at 37° C, followed by incubation with 60 nM of LysoTracker Deep Red (ThermoFisher Scientific, L12492) for 1 hour, and Hoescht nuclear stain (ThermoFisher Scientific, 62249) for 5 minutes. Cells were imaged as described above.

2.2.6 Animal Models

All animal work was performed under a protocol approved by the University of Nebraska Medical Center (UNMC) Institution of Animal Care and Use Committee (IACUC). Subcutaneous tumor models were generated by injecting 1×106 T3M4 or Colo357 cells suspended in 100 µl of 1:1 growth media and Matrigel (Corning, 356234) into the left flank of 6–8 week old female NU/J mice (Jackson Laboratories, 002019; Bar Harbor, ME). T3M4 tumors were allowed to grow for 11 days, and Colo357 tumors were allowed to grow for 30 days. Orthotopic tumor models were established by injecting 2.5 × 10^5 T3M4 cells suspended in 30 µl of PBS into the pancreas of 6–8 week old female NU/J mice as previously described [205]. Surgery was conducted on a sterile drape, and a TP700 TPump Professional Core Warming and Cooling System (Stryker Corp; Kalamazoo, MI) maintained at 37° C. The surgical field was prepped by alternating swabs of povidone iodine and alcohol swabs. Mice were allowed to recover and were monitored after surgery. Buprenorphine (Bupranex®, Reckitt Benckiser Pharmaceuticals, 955531; Hull, England) (0.1 mg/kg) was administered twice per day for three days after surgery.

2.2.7 Fluorescence Imaging Dynamics

2 nmol of IRDye800 (free dye control, LI-COR Biosciences, 929–08972), IgG-IRDye800 isotype control or AR9.6-IRDye800 were injected via tail vein into female NU/J mice bearing subcutaneous tumors. Images were taken at 4, 24, 48, 72, 96, 120, and 144 h post-injection with the 800 nm channel and white channel on the Pearl® Trilogy small animal imaging system (LI-COR Biosciences). Full necropsies were performed at 144 h. Digestive organs were perfused with PBS, and all organs were imaged on the Pearl® Trilogy. Images were analyzed using Image Studio software version 5.0 (LI-COR Biosciences). Briefly, a region of interest (ROI) was drawn around the tumor, and a secondary ROI was drawn around the unaffected flank. Tumor to background ratios (TBR) were calculated as follows: (mean fluorescent signal in tumor / mean fluorescent signal in unaffected flank). SNR were calculated as follows: (mean fluorescent signal in the tumor / standard deviation of the background) [206].

2.2.8 Fluorescence-Guided Surgery

T3M4 orthotopic tumor cells were implanted and allowed to proliferate for 20 days. Mice were injected with 1 nmol (based on dye) of AR9.6-IRDye800 or IgG-IRDye800 via tail vein injection. Mice were euthanized 144 h after antibody conjugate administration, and images were collected on the Pearl® Trilogy, Fluobeam 800 (Fluoptics; Cambridge, MA), and the Lab Flare RP1 (Curadel; Natick, MA) FGS systems. Tumor was resected with image guidance using the Fluobeam and Lab Flare imaging systems, and complete necropsies were subsequently conducted. AR9.6-IRDye800 and IgG-IRDye800 groups were resected using the same exposure time (500 ms). Fluobeam images were analyzed to calculate intraoperative TBR using Image J software (version 1.52a, NIH; Bethesda, MD). Briefly, intraoperative TBR (mean fluorescent signal in tumor/ mean fluorescent signal in normal pancreas or adjacent peritoneal tissue) was calculated by manually defining a ROI around the suspected tumor and adjacent

background and analyzing the mean signal in each identified region. Dissected organs were imaged on the Pearl® Trilogy. Organ signal was quantified with Image Studio software by manually defining ROI around each tissue and obtaining the mean fluorescent signal, and SNR was calculated as described above. Necropsied organs were spectrally analyzed using a wavelength-resolved semi-quantitative surgical detection system [207]. The handheld probe was positioned 1 cm above resected tissues. Points across the length of the tumor and pancreas were excited at 785 nm using 8 mW (low) laser power. Emission spectra were collected from 800–950 nm, consistent with previous reports [205, 206].

2.2.9 Orthotopic Tumor Histology

Organs and tumors resected at 144 h after injection of antibody conjugates were embedded in optimal cutting temperature compound (OCT) blocks and stored at −20° C until processing for histology. Tissues were cut into 10 μm thick sections using a cryostat (Leica; Buffalo Grove, IL) and mounted on charged microscope slides (ThermoFisher, 22–037-246). Slides were dried at room temperature for 20 min and fixed with chilled acetone for 10 min, and allowed to dry at room temperature for 20 min. To detect the presence of AR9.6-IRDye800 or IgG-IRDye800 at 144 h, slides were imaged with an Olympus DP80 Digital Camera and cellSense Dimension Software in the FITC channel (tissue autofluorescence), and the 800 nm channel (AR9.6-IRDye800 or IgG-IRDye800). Hematoxylin and Eosin (H&E) staining was conducted according to standard procedures and imaged under brightfield microscopy.

2.2.10 Human Pancreatic Cancer Samples

Tumors resected at the time of surgery were flash-frozen and embedded in OCT. Immunohistochemistry was conducted using standard procedures for frozen tissues, and the AR9.6 antibody (1:125 dilution, 1 mg/ml stock solution). Tumors resected at autopsy

were obtained from the University of Nebraska Medical Center's Tissue Bank through the Rapid Autopsy Pancreatic (RAP) program in compliance with IRB 091–01. To ensure specimen quality, organs were harvested within three hours postmortem, and the specimens placed in formalin for immediate fixation. Sections were cut from paraffin blocks of formalin-fixed tissue into 4-micron thick sections and mounted on charged slides. Slides were stained with OC125 (Roche, 760–2610; Basel, Switzerland) according to standard protocols for paraffin-embedded tissues. Slides were imaged on an Olympus DP80 Digital Camera and cellSense Dimension software.

2.2.11 Statistical Analysis

All statistical analyses were conducted using Graph Pad Prism software version 7.03 (GraphPad Software). 2-way ANOVA was used, followed by Tukey's test for multiple comparisons to compare differences in SNR and TBR between AR9.6-IRDye800, IgG-IRDye800, and unconjugated IRDye800. Multiple t-tests were used to compare the biodistribution of AR9.6-IRDye800 to IgG-IRDye800. The SNR of AR9.6-IRDye800 and IgG-IRDye800 were compared with an unpaired t-test. All values are reported as the mean ± standard deviation.

2.3 Results

2.3.1 MUC16 in Pancreatic Cancer Patients

MUC16 has been implicated as a potential target for pancreatic cancer. To investigate the expression of MUC16 in patients, immunohistochemistry was conducted on patient samples. Human pancreatic cancer samples shown in **Figure 7A**, **7B**, and **7C** were obtained from the UNMC rapid autopsy pancreas program, and samples shown in **Figure 7D** and **7E** were collected during surgical resection. These specimens were stained for MUC16 expression with mAb AR9.6. All patient samples were analyzed by a board-certified pathologist (G.A.T). Normal pancreas samples obtained at surgery and

autopsy and pancreatitis samples obtained at autopsy showed no expression of MUC16 **(Figure 7A, 7B, 7E)**. Conversely, pancreatic cancer samples collected at autopsy showed strongly positive apical staining as well as diffuse cytoplasmic and membrane staining of MUC16 **(Figure 7C)**. Precursor lesions termed pancreatic intraepithelial neoplasms, or PANIN, lesions were also present in the pancreatic cancer sections. These lesions displayed weak MUC16 staining. Samples collected at surgical resection showed MUC16-positive cytoplasmic staining in the stromal fibroblasts, and apical cytoplasmic staining in the tumor **(Figure 7D)**. These results indicate that MUC16 is a feasible target for FGS in the key patient population of interest.

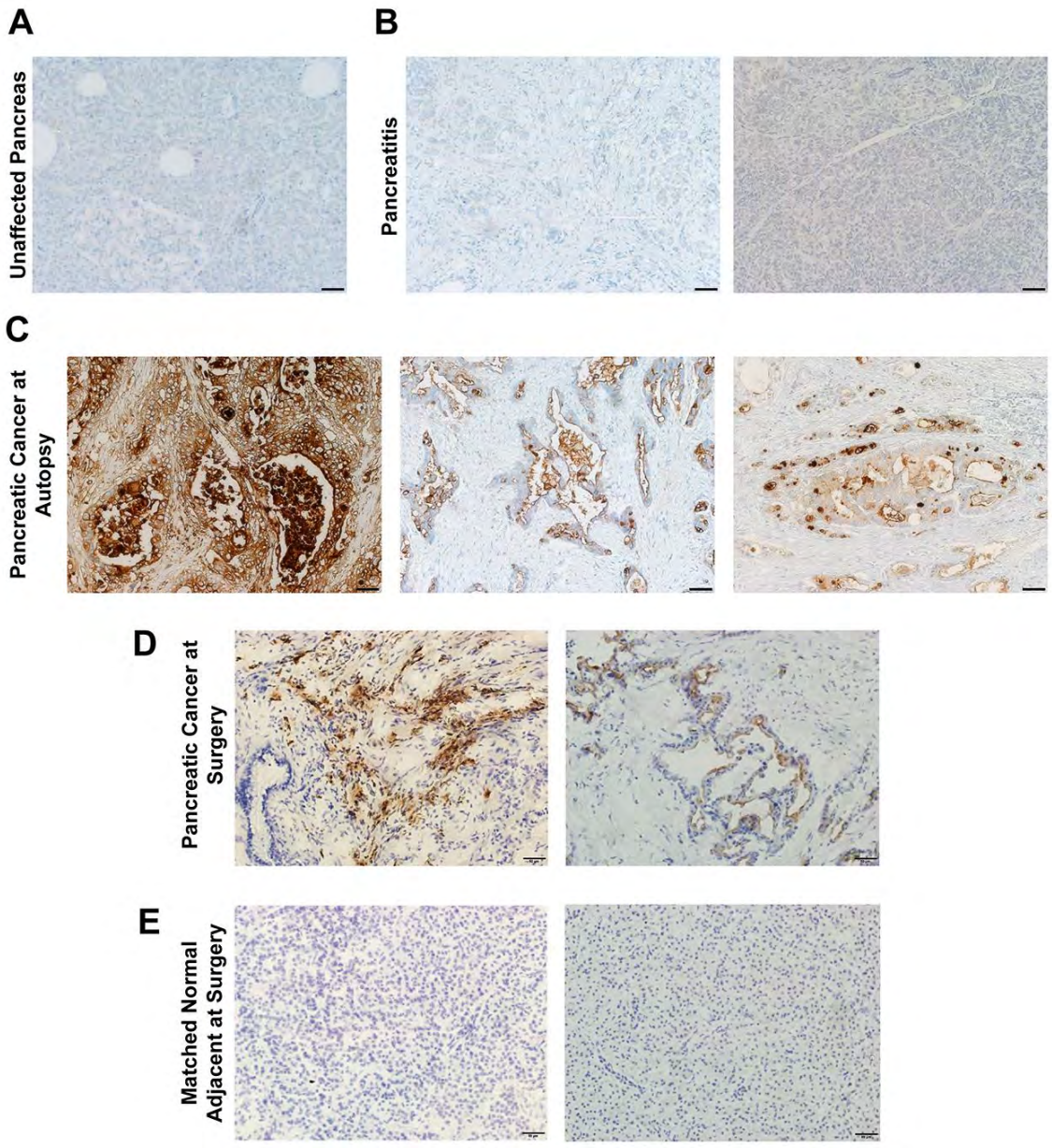

Figure 7: MUC16 expression in human pancreatic ductal adenocarcinoma samples. **(A)** Unaffected pancreas **(B)** pancreatitis **(C)** pancreatic cancer samples collected at autopsy. **(D)** Pancreatic cancer resected at the time of surgery and **(E)** matched normal adjacent tissue collected at the time of surgery. All images acquired at 200X magnification. Scale bar = 50 μm. Originally printed in Olson, Wojtynek, et al. [190], reprinted with permission from © 2020, American Association for Cancer Research.

2.3.2 Synthesis and *In vitro* Validation of MUC16 Expression

To develop a targeted FGS probe, AR9.6 and isotype-specific IgG control antibody were conjugated to the NIR dye, IRDye800 NHS Ester. AR9.6-IRDye800 and IgG-IRDye800 antibody conjugates were synthesized by reacting NHS ester dye with free amines on the antibody to form stable amide bonds **(Figure 8A)**. IgG was used as a non-specific isotype control throughout this study. Conjugation reactions resulted in an average of 3 dyes per protein as determined by absorbance spectroscopy **(Figure 8B)**. Fluorescence spectra of the antibody conjugates demonstrated that fluorescence was not quenched upon conjugation to the protein.

The expression of MUC16 was assessed by western blot in 5 pancreatic cancer cell lines: T3M4, Capan1, Colo357, CFPAC, and HPAC **(Figure 8C)**. An immortalized pancreas cell line (HPNE) served as a negative control, and the ovarian cancer cell line, OVCAR3, which has well-documented MUC16 expression, served as a positive control [208, 209]. A range of moderate to high expression of MUC16 was seen across all pancreatic cancer cell lines. To confirm that conjugation of AR9.6 to IRDye800 did not drastically impact antigen recognition and cell binding, a fluorescent western blot and fluorescence microscopy were conducted, as shown in **Figure 8D and 8E**. Fluorescent western blotting in the 800 nm channel demonstrated that AR9.6-IRDye800 could still recognize MUC16 after dye conjugation. Secondary antibody binding (700 nm channel) confirmed that the fluorescence seen in the 800 nm channel was due to the presence of AR9.6-IRDye800 binding, as shown by colocalization between the 700 and 800 nm channels in **Figure 8D**. As expected, the non-specific IgG-IRDye800 conjugate did not bind to MUC16, and secondary antibody staining confirmed that AR9.6 was not present. Fluorescence microscopy showed strong fluorescence signal from AR9.6-IRDye800 in MUC16-expressing pancreatic cancer cell lines, which was consistent with OVCAR3 cells (positive control). AR9.6-IRDye800 did not bind to MUC16-negative HPNE cells,

and the IgG-IRDye800 control did not bind to cells, regardless of MUC16 expression levels **(Figure 8E)**.

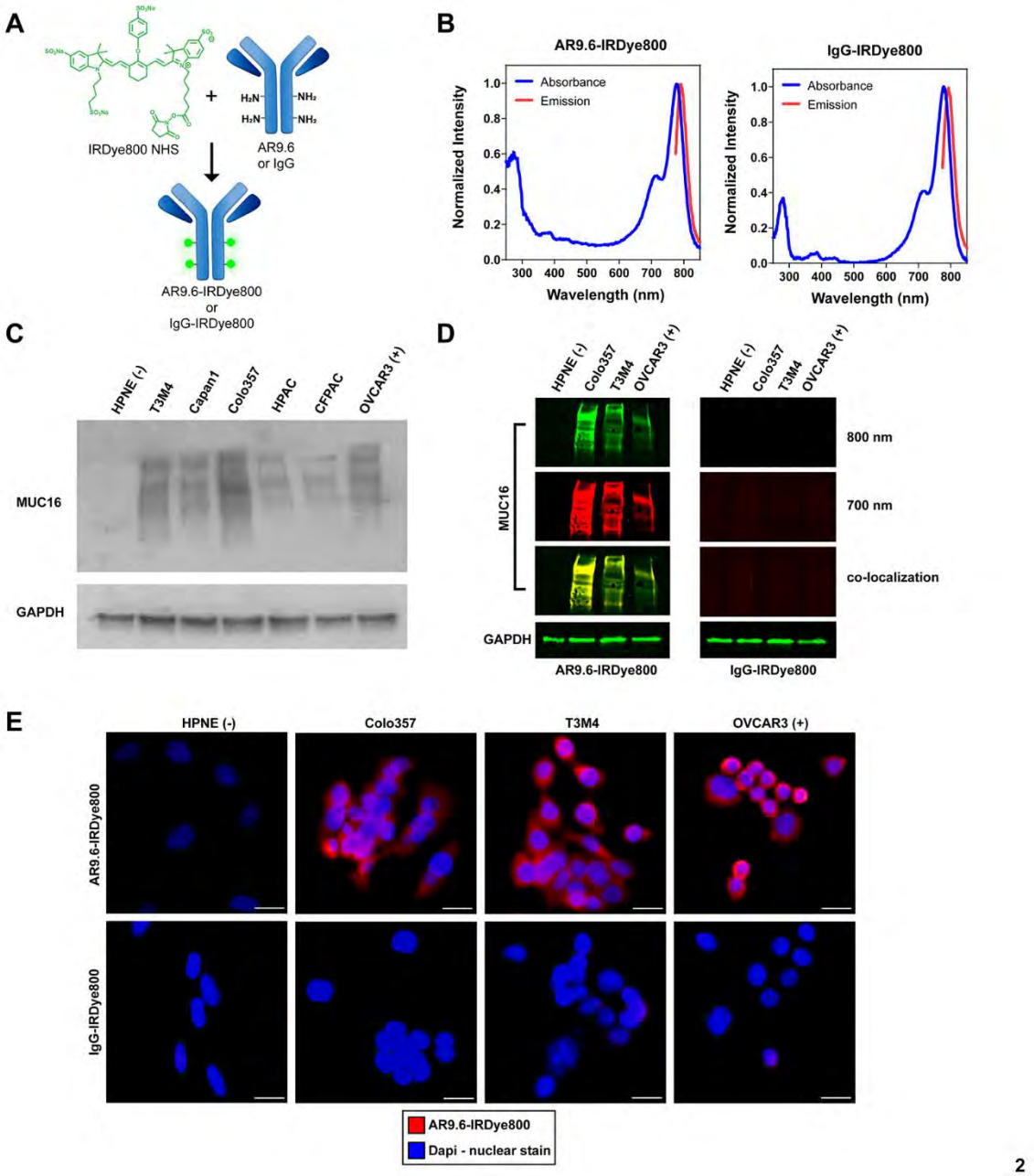

Figure 8: Synthesis and in vitro characterization of antibody conjugates. **(A)** Schematic of IRDye800 NHS Ester conjugation to AR9.6 and IgG. **(B)** Representative absorbance and emission spectra from both antibody conjugates. **(C)** Western blot of MUC16 expression in human pancreatic cancer cell lines. **(D)** Fluorescent western blot confirming binding of AR9.6-IRDye800, and lack of binding in IgG control. **(E)** Immunofluorescence of antibody conjugate binding. Images acquired at 400X magnification. Scale bar = 20 μm. Originally printed in Olson, Wojtynek, et al. [190], reprinted with permission from © 2020, American Association for Cancer Research.

2.3.3 Determination of AR9.6-IRDye800 Optimal Imaging Time from Tumor Signal Dynamics

To monitor the tumor accumulation of the antibody conjugates over time, AR9.6-IRDye800, IgG-IRDye800, and unconjugated IRDye800 were assessed for 6 days in a subcutaneous T3M4 xenograft model of pancreatic cancer. **Figure 9A** depicts representative images of tumor accumulation from the three groups over 144 h based on images acquired daily on the Pearl® Trilogy. Strong fluorescence signal was observed throughout the mouse at 4 h, while robust enhancement of the tumor was observed within 24 h after injection of AR9.6-IRDye800, and signal was retained in the tumor at 144 h. Diffuse signal was observed with IgG-IRDye800 at 24 h, while unconjugated IRDye800 was cleared within 24 h as expected [210]. TBRs were highest for AR9.6-IRDye800 at 144 h after injection (4.47 ± 1.43), as compared to 2.12 ± 0.12 for the IgG-IRDye800 control and 0.89 ± 0.11 for the unconjugated IRDye800 **(Figure 9B)**. The TBR for AR9.6-IRDye800 was significantly higher ($p < 0.0001$) than IgG-IRDye800 at 144 h (the peak TBR for the IgG control). SNRs were also calculated for the three groups **(Figure 9B)**. At 144 h, AR9.6-IRDye800 still showed significantly higher ($p = 0.0492$) SNR (94.35 ± 33.66) than IgG-IRDye800 (48.18 ± 6.68) and IRDye800 (5.56 ± 1.24). Tumor accumulation of AR9.6-IRDye800 in Colo357 xenografts **(Figure 10)** resulted in comparable TBR (N=4, TBR =5.63 ± 0.70) to the T3M4 xenografts. The function of both the TBR and SNR metrics for imaging has been previously reviewed [211]. In vitro analysis of the cellular kinetics of AR9.6-IRDye800 binding shown in **Figure 11** suggests that antibody internalization, and lysosomal degradation, may contribute in part to the decrease in fluorescence signal over time [212].

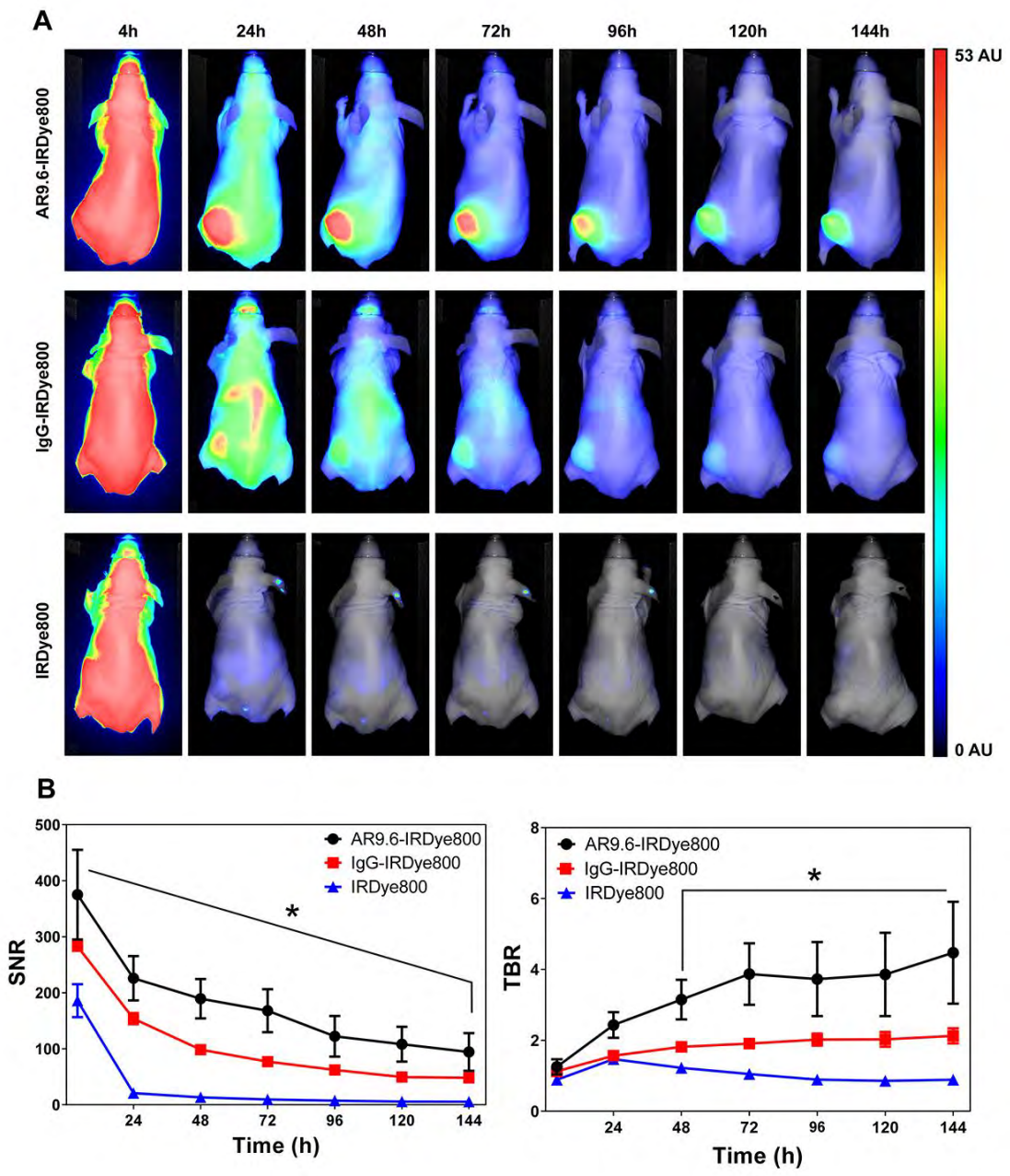

Figure 9: Tumor accumulation of fluorescent antibody conjugates. **(A)** Representative images from the biodistribution of the fluorescent conjugates AR9.6-IRDye800, IgG-IRDye800, and unconjugated IRDye800, from 4 −144 h (N = 4). Normalized arbitrary units (AU) depicted on the color bar is representative of all images. **(B)** Signal to noise ratios and tumor to background ratios of AR9.6-IRDye800, IgG-IRDye800, and unconjugated IRDye800 over 144 h. Originally printed in Olson, Wojtynek, et al. [190], reprinted with permission from © 2020, American Association for Cancer Research.

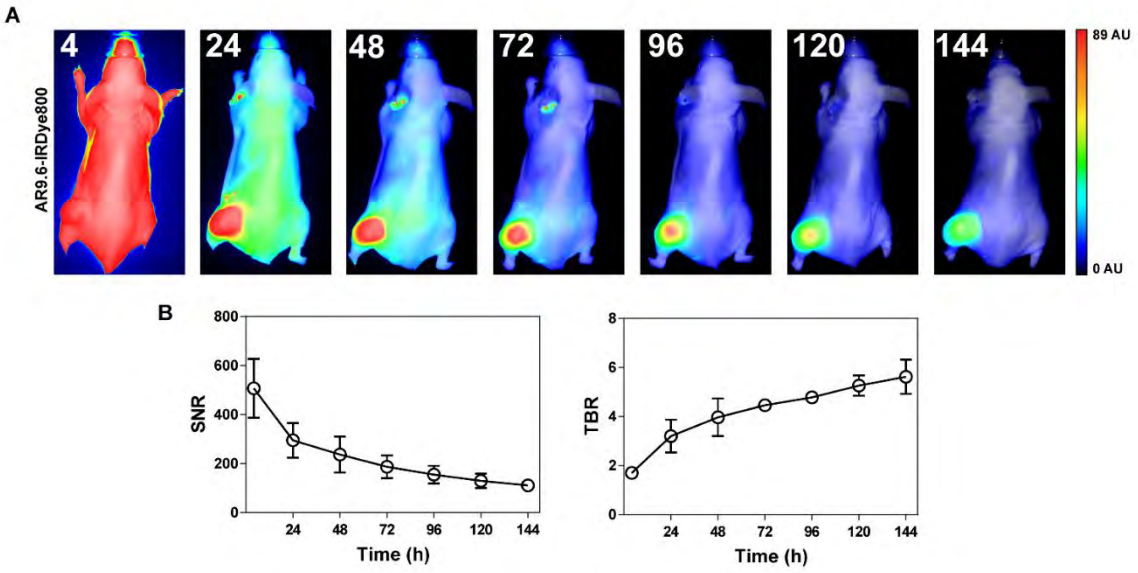

Figure 10: Biodistribution of AR9.6 in a Colo357 subcutaneous xenograft model over 144 h. **(A)** Representative images from LI-COR Pearl imaging, images on color bar scaled to arbitrary units (AU). **(B)** Tumor signal to noise ratio (SNR) and tumor to background ratio (TBR) over 144 h (*N*=4). Originally printed in Olson, Wojtynek, et al. [190], reprinted with permission from © 2020, American Association for Cancer Research.

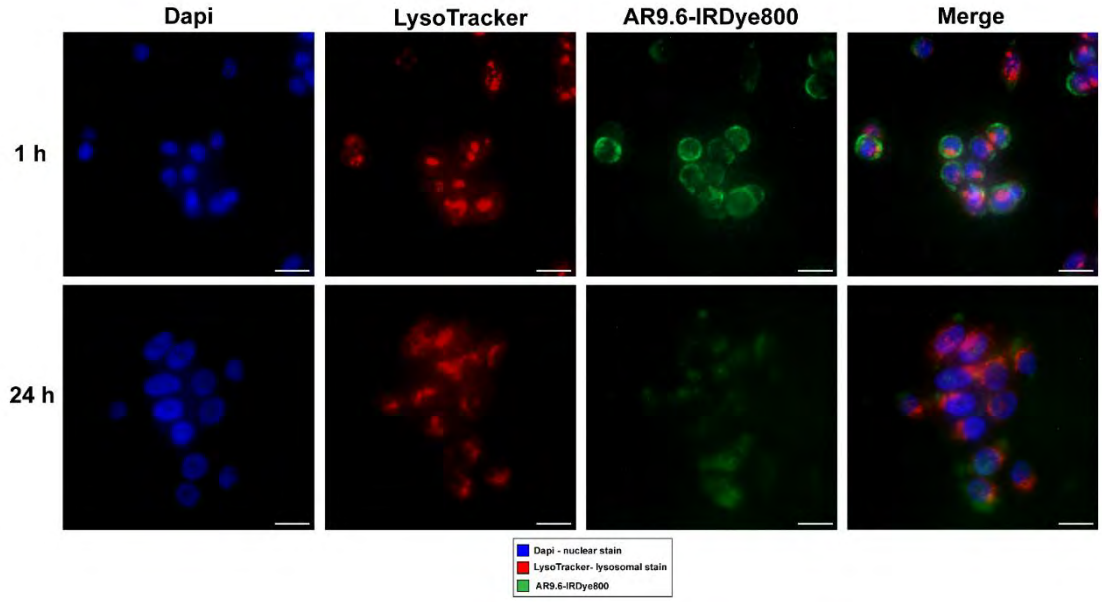

Figure 11: Internalization of AR9.6-IRDye800 at 1 hour and 24 hours after incubation. Originally printed in Olson, Wojtynek, et al. [190], reprinted with permission from © 2020, American Association for Cancer Research.

To further assess the specificity of the AR9.6 conjugate for the tumor, all T3M4 xenograft tumors and clearance organs were collected at 144 h post-injection and imaged on the Pearl® Trilogy to analyze fluorescence signal in key clearance organs as shown in **Figure 12**. Quantification of tumor signal demonstrated a significant 2.18-fold increase in mean fluorescence intensity in the AR9.6-IRDye800 tumors compared to the IgG-IRDye800 ($p<0.0001$). AR9.6-IRDye800 also showed significantly lower signal in the liver at the 144 h time point when compared to the IgG control ($p= 0.0120$). AR9.6-IRDye800 displayed a 2.65-fold increase in tumor signal compared to AR9.6-IRDye800 liver signal ($p<0.0001$). Conversely, the IgG-IRDye800 control showed higher liver signal than tumor signal. These results demonstrate the specificity and retention of the AR9.6 conjugate for tumor detection. Additionally, higher fluorescent signal was observed in the tumor compared to the liver, suggesting that AR9.6-IRDye800 could potentially highlight metastatic lesions on key background tissues in future studies.

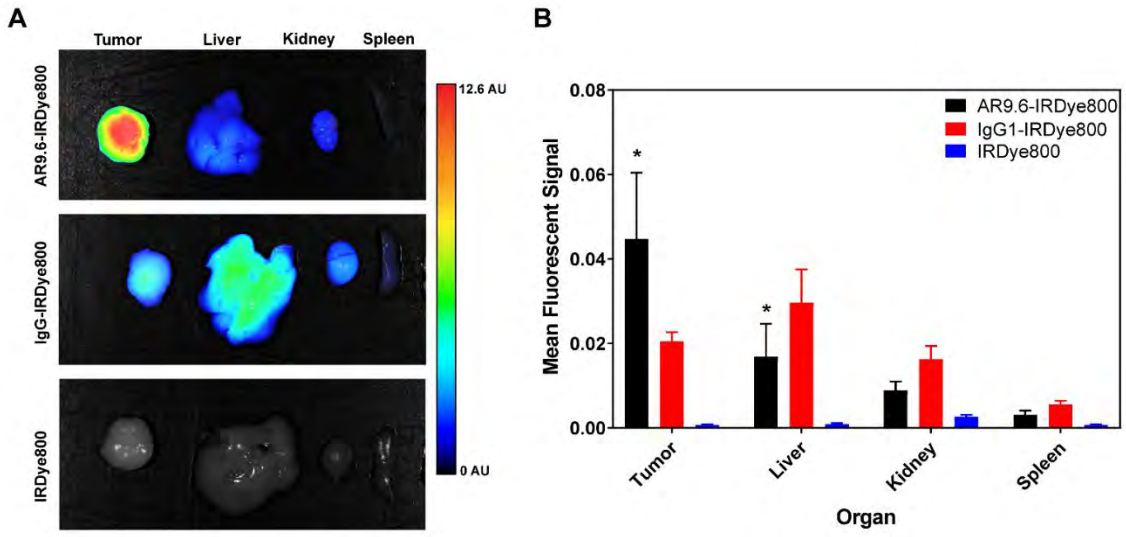

Figure 12: (A) Biodistribution of AR9.6-IRDye800, IgG-IRDye800, and unconjugated IRDye800 in key clearance organs at 144 h in subcutaneous T3M4 model from optimal imaging time study. Color bar scaled to normalized arbitrary units for all images. **(B)** Mean fluorescent signal in key clearance organs at 144 h (*N*=4). Significance determined by Two way ANOVA, followed by Tukey's test for multiple comparisons. Tumor to tumor comparison: $p<0.0001$ for AR9.6-IRDye800 compared to IgG-IRDye800 and IRDye800. Tumor to liver comparison: $p<0.0085$ for AR9.6-IRDye800 compared to IgGIRDye800, and $p<-0009$ for AR9.6-IRDye800 compared to IRDye800. Originally printed in Olson, Wojtynek, et al. [190], reprinted with permission from © 2020, American Association for Cancer Research.

2.3.4 Fluorescence-Guided Surgery

FGS of orthotopic pancreatic cancer xenografts was conducted on multiple FGS systems. These systems are summarized in **Figure 13**. The FDA-approved Fluobeam 800 imaging system provided real-time intraoperative feedback via a single 800 nm channel display system [74]. Using Fluobeam 800 guidance, AR9.6-IRDye800 provided robust tumor enhancement against background organs, including the liver **(Figure 14A)**. Conversely, there was variable and negligible fluorescence in the IgG-IRDye800 group, and the signal in the liver was brighter than tumor signal **(Figure 14B)**. As shown in **Figure 14C**, the mean intraoperative TBR for AR9.6-IRDye800 (3.75 ± 0.29) was significantly higher than the mean intraoperative TBR for IgG-IRDye800 (1.89 ± 0.55) ($p = 0.0010$). The Lab Flare RP1 image-guided surgery system (currently restricted to preclinical studies) was used to confirm AR9.6-IRDye800 signal with real-time NIR-color channel display. Images on this system also showed strong contrast-enhancement with AR9.6-IRDye800. Tumor was clearly delineated against healthy pancreas, and additional lesions could be seen on the posterior surface of the pancreas **(Figure 14D)**.

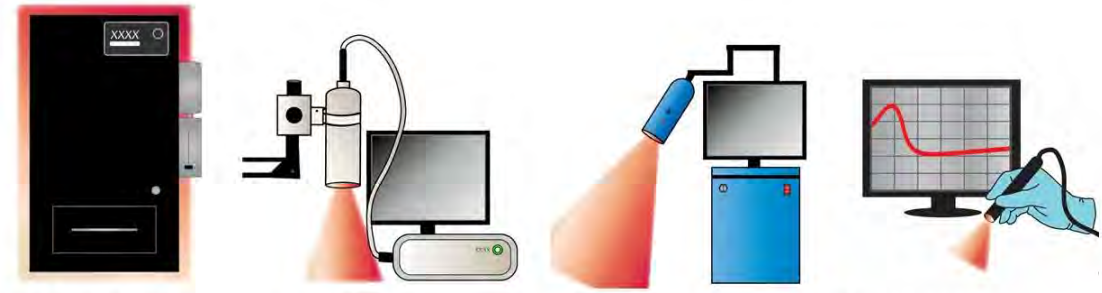

LI-COR Pearl
- Indication: Small Animal Imaging
- Pre-clinical use
- Highly sensitive

Fluobeam
- Indication: Image-Guided Surgery
- FDA approved
- Only 800 nm channel

Curadel
- Indication: Image-Guided Surgery
- Pre-clinical use
- Pseudocolor channel

Spectropen
- Indication: Spectral acquistion
- Pre-clinical use
- Quantitative

Figure 13. Summary of imaging systems used to conduct fluorescence-guided surgery studies.

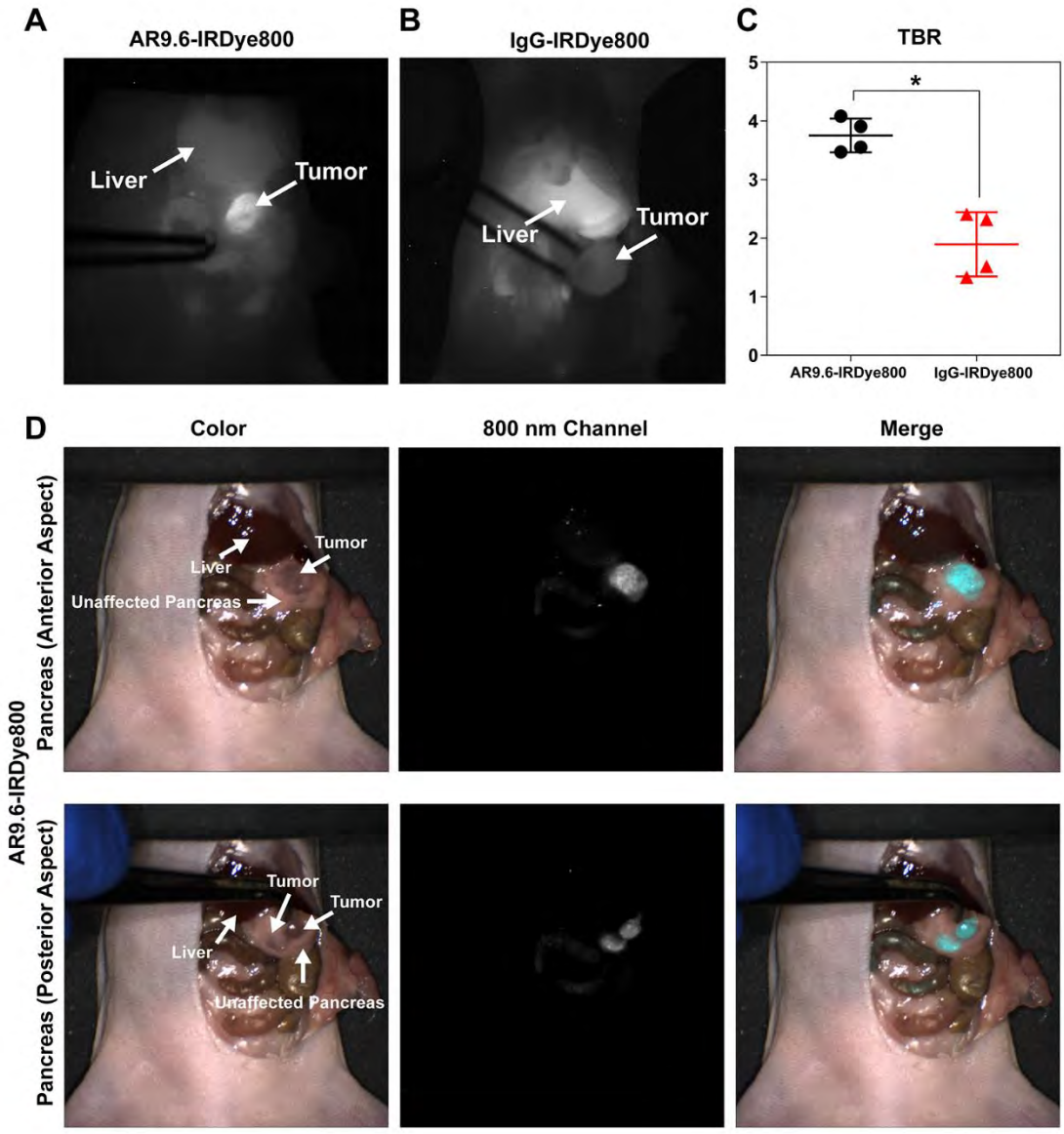

Figure 14: Fluorescence-Guided Surgery in orthotopic pancreatic cancer. Representative Fluobeam images of FGS with **(A)** AR9.6-IRDye800 and **(B)** IgG-IRDye800. **(C)** Calculated TBR (tumor signal/ adjacent normal pancreas or adjacent peritoneal tissue) in tumors ($p = 0.0010$). **(D)** Representative images of anterior and posterior pancreas imaging with AR9.6-IRDye800 using the Lab Flare RP1. Originally printed in Olson, Wojtynek, et al. [190], reprinted with permission from © 2020, American Association for Cancer Research.

Biodistribution of fluorescent antibody conjugates was analyzed in necropsied organs after FGS **(Figure 15A)**. Quantification of the biodistribution demonstrated significantly higher mean fluorescent signal in the tumors with AR9.6-IRDye800 (0.05 ± 0.006) compared to the IgG-IRDye800 control (0.014 ± 0.009) ($p = 0.0009$) **(Figure 15B)**. There were no significant differences in mean signal between any of the other organs. Variable fluorescent signal was observed in the stomach due to autofluorescence from the mouse diet. Signal in the liver and kidneys can be attributed to clearance of the antibody-dye conjugate and released dye, respectively. The mean tumor SNRs of AR9.6-IRDye800 (94.09 ±11.95) and IgG-IRDye800 (28.33 ± 18.67) were also significantly different ($p = 0.0010$).

Necropsied organs were also analyzed with a spectrophotometric device. Spectra were collected at defined points across the tumor. **Figure 16A** and **16B** depict the integrated fluorescence emission spectra that correspond to each point excitation. Fluorescent enhancement of the tumor tissue corresponded to an increase in area under the curve from spectral acquisition. Furthermore, colocalization between fluorescent signal and the presence of tumor tissue can be seen in H&E staining. Resected specimens were confirmed as poorly differentiated tumors by a board-certified pathologist (G.A.T). AR9.6-IRDye800 showed increased signal from fluorescence images as well as wavelength resolved measurements compared to the IgG-IRDye800 control. Tumor sections embedded in OCT were analyzed for the presence of AR9.6-IRDye800 and IgG-IRDye800 **(Figure 16C)**. NIR fluorescence was detected in tumors from mice that were administered AR9.6-IRDye800, while NIR fluorescence was not detected in tumor sections from mice administered IgG-IRDye800.

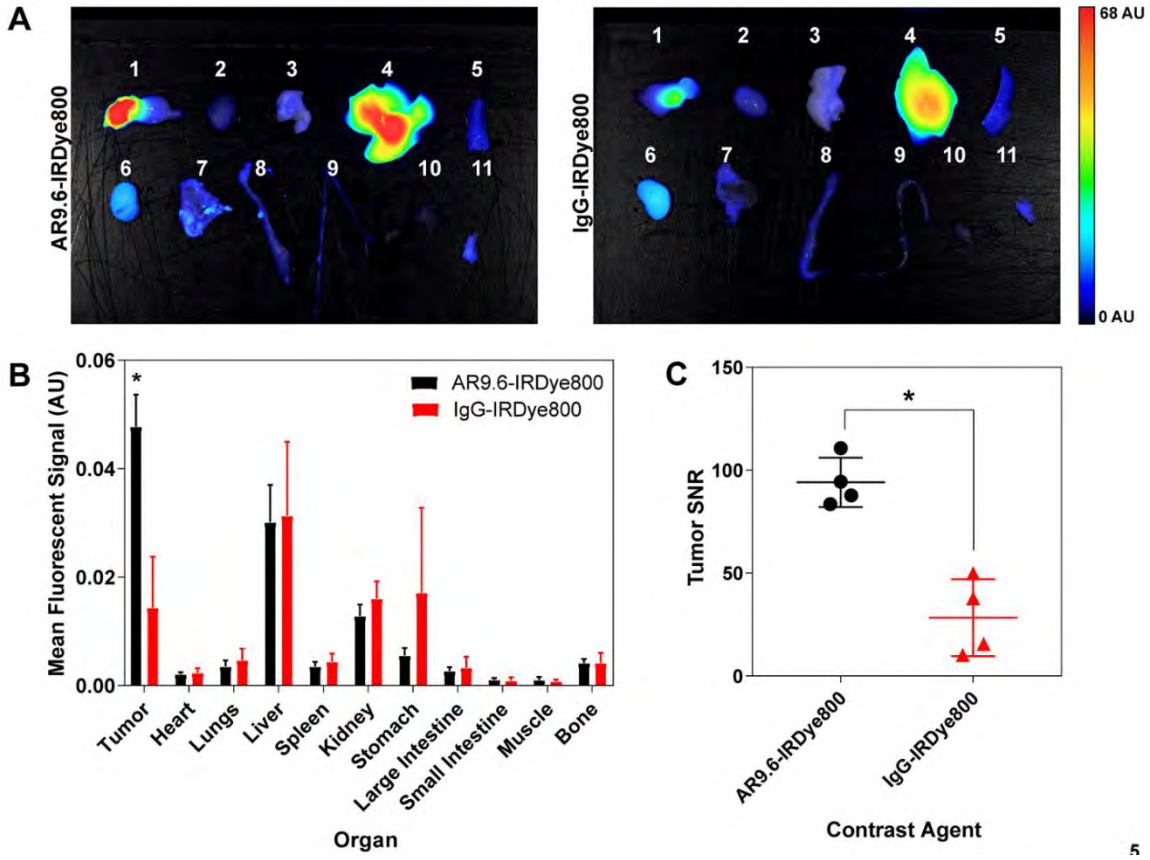

Figure 15: Biodistribution and signal of AR9.6-IRDye800 and IgG-IRDye800 in an orthotopic xenograft model. **(A)** Biodistribution of AR9.6-IRDye800 and IgG-IRDye800 at 144 h post-injection in necropsied organs. (N=4)) 1=Tumor and Unaffected Pancreas, 2=Heart, 3=Lung, 4=Liver, 5=Spleen, 6=Kidney, 7=Stomach, 8=Large Intestine, 9=Small Intestine, 10=Muscle, 11=Bone. **(B)** Mean fluorescent signal across necropsied organs. ($p = 0.00095$) **(C)** Calculated SNR (tumor signal/ standard deviation of background) in tumors ($p = 0.0010$). Originally printed in Olson, Wojtynek, et al. [190], reprinted with permission from © 2020, American Association for Cancer Research.

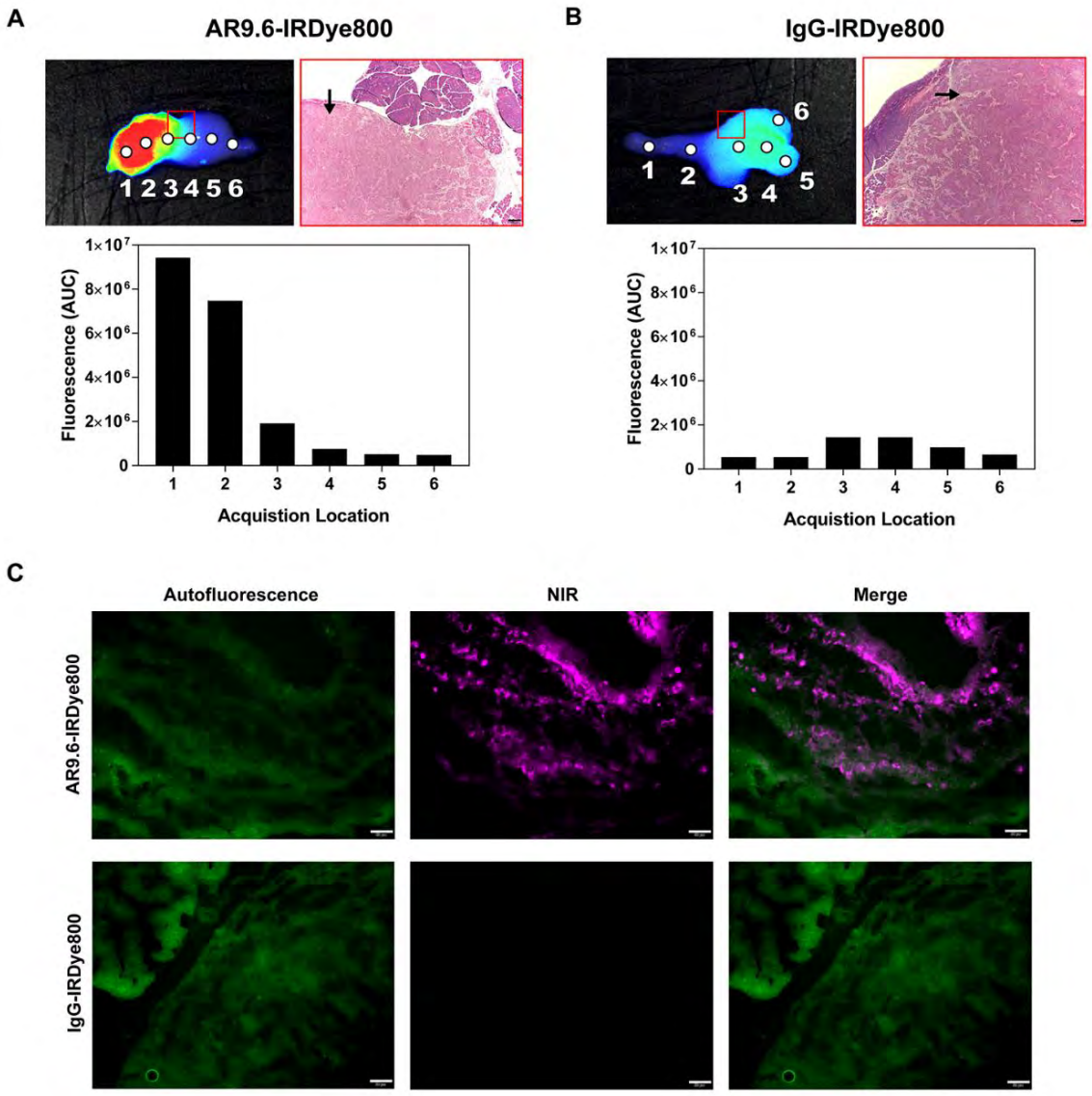

Figure 16: Spectral analysis of tumors and fluorescent histology. **(A)** Pearl® Trilogy imaging, H&E staining, and acquired spectra for AR9.6-IRDye800 tumor. The red box denotes the area depicted by the H&E image, and the black arrow denotes tumor. **(B)** Pearl® Trilogy imaging, H&E staining and acquired spectra for IgG-IRDye800 tumor. **(C)** Fluorescence microscopy in tumors. Images acquired at 200X magnification. Scale bars = 50 μm. Originally printed in Olson, Wojtynek, et al. [190], reprinted with permission from © 2020, American Association for Cancer Research.

As shown in **Figure 17**, micro-metastatic lesions were identified during AR9.6-IRDye800-guided resection. NIR signal was readily detected in spleen, muscle, and lung metastases. H&E staining of resected OCT embedded specimens demonstrated the presence of tumor tissue in the detected metastatic lesions. Metastatic lesions were confirmed by a board-certified pathologist (G.A.T). Fluorescence microscopy demonstrated the presence of AR9.6-IRDye800 in the tumor tissue. Fluorescent signal from AR9.6-IRDye800 was consistent with the location of the metastatic lesions, whereas adjacent resected tissue had no visible fluorescence present. Fluorescence localization in the metastatic lesions demonstrated high specificity of AR9.6-IRDye800 for the tumor tissue.

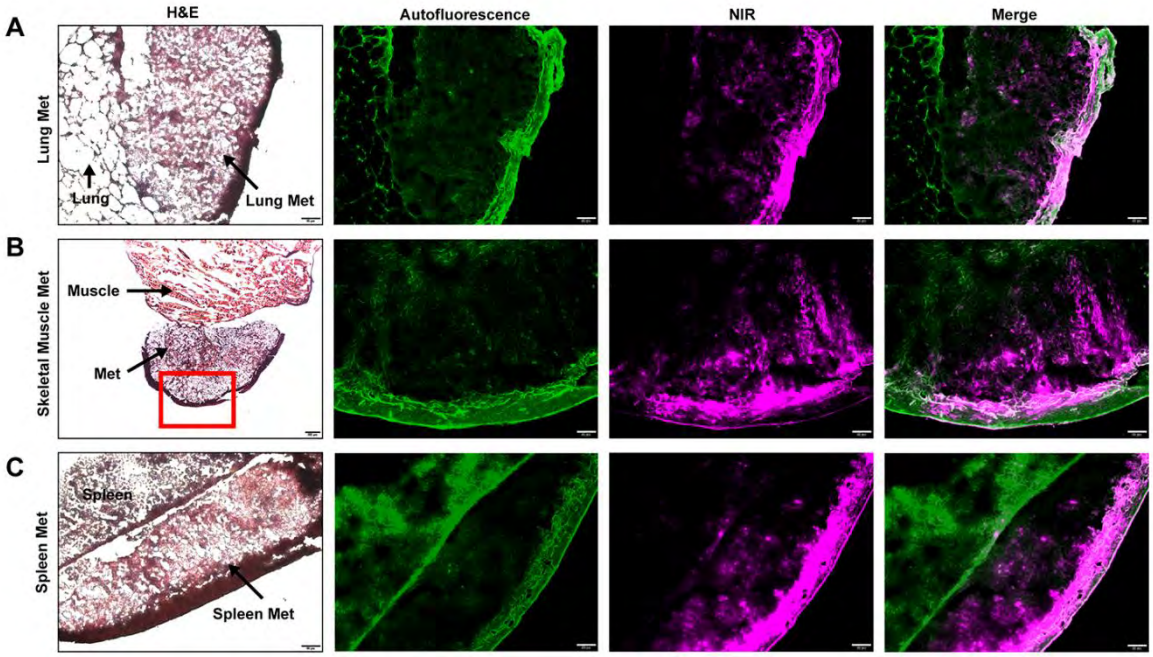

Figure 17: Identification of micro-metastases. OCT embedded **(A)** lung metastasis, **(B)** skeletal muscle metastasis, and **(C)** spleen metastasis. Images acquired at 200X magnification. Scale bar = 20 μm. Skeletal muscle H&E image acquired at 40X magnification. Scale bar = 200 μm.

2.4 Discussion

MUC16 is widely expressed in the tumors of patients with pancreatic, ovarian, gastric, esophageal, and colon cancer, among others [201]. Since MUC16 is natively expressed in normal bronchial, ovarian, endometrial, and corneal cells in the body, there is high potential for low background signal from key organs during pancreatic cancer imaging [202]. Furthermore, in comparison to other targets in pancreatic cancer such as CEA and CA-19–9, MUC16 can better differentiate between chronic pancreatitis and pancreatic cancer [204]. Thus, there is compelling evidence to support the development of MUC16 as a target for image-guided surgical intervention of pancreatic cancer.

Compared to current FGS probes in clinical trials, AR9.6-IRDye800 has several potential advantages. EGFR, the target of cetuximab-IRDye800 and panitumumab-IRDye800, has variable expression levels across pancreatic cancer [213]. EGFR is also expressed in the healthy pancreas, chronic pancreatitis, and normal stomach and duodenal tissues, which could contribute to elevated background signal during intraoperative pancreatic cancer imaging [3, 214]. In comparison, MUC16 is highly expressed in pancreatic cancer tissues, is not expressed in the normal pancreas, and is not expressed in key background tissues within the peritoneal cavity, which could improve contrast with FGS. However, results from the Phase I/II cetuximab-IRDye800 trial showed promising results for using EGFR as a target for imaging pancreatic cancer (NCT02736578). One of the major strengths of this study was the use of multimodal imaging in combining FGS with photoacoustic imaging to improve the depth of penetration. EGFR is also advantageous in that it is present in a wide variety of malignancies, and can be used as a tumor-agnostic FGS target. Additionally, SGM-101 is another antibody-targeted probe that has demonstrated success in a Phase I clinical trial by targeting the tumor antigen CEA (NCT02973672) [200]. However, the use of a 700 nm NIR dye in SGM-101 limited the depth of penetration of FGS and introduced

problems with autofluorescence. Results have not been reported, to date, from the panitumumab-IRDye800, or bevacizumab-IRDye800 (PENGUIN) studies (NCT03384238, NCT02743975). While MUC16 is relatively unexplored as an imaging target in comparison to EGFR and CEA, there is similar potential to utilize this probe to guide resection of a variety of solid tumors.

AR9.6-IRDye800 demonstrates comparable or improved tumor delineation in comparison to imaging agents used in other preclinical studies. Preclinical studies conducted with panitumumab-IRDye800 (now in a Phase I/II trial for pancreatic cancer) in a subcutaneous model of head and neck cancer showed TBRs of 2.9 using an IRDye800 optimized system [215]. Comparatively, with AR9.6-IRDye800 in a subcutaneous pancreatic cancer model, an IRDye800 optimized imaging system yielded a TBR of 4.7 and 5.6 across two different cell types. Both AR9.6-IRDye800 and panitumumab IRDye800 had significantly higher tumor signal using the targeted agent as compared to an IgG control [215]. In an orthotopic model, panitumumab-IRDye800 had a mean intraoperative TBR of 4.2 compared to a mean intraoperative TBR of 3.75 with AR9.6-IRDye800in the orthotopic model. Preclinical studies with SGM-101 (completed Phase 1 clinical trial), performed similarly to AR9.6-IRDye800 with intraoperative TBRs to of 3.5 in an orthotopic pancreatic cancer model [216]. Preclinical studies with a humanized CEA antibody (hM5A) conjugated to IRDye800 also showed a mean TBR of 3.5 in a patient-derived orthotopic xenograft model [217]. Similar results have also been shown in studies using targeting agents other than antibody conjugates in preclinical pancreatic cancer FGS studies. An αvβ6 integrin targeting peptide yielded TBR of 2.7 intraoperatively in an orthotopic model [218]. An antibody fragment, ssSM3E/800CW, targeting CEA, displayed a mean TBRs of 2.37 in an orthotopic model of pancreatic cancer [219]. TBRs achieved under AR9.6-IRDye800 guidance in this

study met the recommended TBR of >3.0 for preclinical studies, suggesting that this probe is a potential candidate for clinical translation [211].

Pancreatic cancer surgeries are complex and often result in recurrence. Despite the challenges of targeting this aggressive tumor model, there is an unmet clinical need to improve surgical outcomes. Due to the heterogeneity of pancreatic tumors, initial clinical trials with existing targeted probes have seen only modest tumor enhancement under FGS [200]. Future clinical trials in pancreatic cancer will likely incorporate a panel of FGS probes to more accurately capture the tumor heterogeneity and improve intraoperative contrast and enhancement for improved resections [57]. However, the feasibility of incorporating multiple probes needs to be investigated to determine if multiple targets improve overall contrast. Because of the well-documented role of mucins in pancreatic cancer, AR9.6-IRDye800 has strong potential to improve current FGS in pancreatic cancer. Thus, we have identified an additional target for FGS that is widely expressed in pancreatic cancer patients.

Identification of occult peritoneal metastases is critical in FGS. Preoperative imaging modalities can accurately predict unresectability in pancreatic cancer but fall short in detecting small metastatic lesions, identifying vascular involvement, and differentiating benign conditions [220]. Thus, FGS can be beneficial in identifying metastases that may have been missed on initial imaging scans. This will impact the course of treatment for pancreatic cancer patients, as the presence of metastatic lesions determines the resectability of the tumor [221]. In this study, AR9.6-IRDye800 identified multiple metastatic lesions in the muscle, lung, and spleen. This suggests that AR9.6-IRDye800-guided resection could potentially improve the identification of missed lesions during surgery. Further studies are needed to investigate the detection capabilities of micro-metastases in patient samples.

This study demonstrates the feasibility and proof-of-concept for MUC16 as a potential target and warrants further investigation. The AR9.6 antibody used here was a murine antibody that can recognize both mouse and human MUC16 and is thus limited in its translational potential, because of potentially high levels of immunogenicity. Immunogenicity can occur after a single dose, but risk increases with repeating doses. Because of the high potential for immunogenicity, murine antibodies make up only 2.8% of antibodies in the clinic to date [222–224]. However, this antibody was chosen for investigation because a humanized AR9.6 antibody is under development, and future studies will investigate the humanized antibody for clinical translation. Additionally, because of variations in tumor size, not all of the orthotopic xenografts had sufficient unaffected healthy pancreas remaining at the time of FGS. Thus, TBR was calculated using either remaining adjacent normal pancreas or adjacent peritoneal tissue as background signal. Future studies will standardize tumor size and calculate TBR in the adjacent healthy pancreas or inflammatory tissue. Additionally, the optimal dye: protein ratio for AR9.6-IRDye800 imaging of pancreatic cancer, as well as methods for site-specific conjugation, will also be investigated. Furthermore, this study does not address the role of tumor heterogeneity on intraoperative fluorescence contrast. Since dense stroma and heterogeneous cell populations can impact the deposition of antibody probes as well as drugs, particularly in pancreatic cancer, further studies are needed to explore FGS in the context of varying cell populations. Discrepancies between experimental studies and clinical results in pancreatic cancer can be attributed in part to inaccurate or ineffective recapitulation of the tumor stroma and microenvironment [225]. Genetically engineered mouse models or patient-derived xenograft models must be employed to more accurately depict the complexity of both the tumor and stroma in pancreatic cancer, though these models have limitations as well. The presence of dense stroma

may also impede the delivery of antibodies, and smaller antibody fragments should be investigated to optimize tumor penetration and intratumoral distribution [226–228].

Additionally, the identification of metastatic lymph nodes during surgery is a key component of treating pancreatic cancer patients [229]. Lymph node status is an important predictor of survival, and identification of regional lymph node involvement (N1 disease) may influence the course of adjuvant therapy [230]. Thus, robust identification of N1 disease and the extent of node involvement with FGS could be beneficial in determining treatment, and sufficient nodal resection. This study did not specifically investigate the presence of MUC16 in metastatic lymph nodes. Future studies are needed to explore the prevalence of MUC16 in positive lymph nodes, and the potential for AR9.6-IRDye800 to identify positive lymph nodes during surgery. Finally, the ectodomain of MUC16 can be cleaved and has been found to circulate in the bloodstream in several cancers, which could impact the feasibility of MUC16 as a target in cancer. Cleavage and subsequent circulation of the antigen may impact the amount of the antibody that actually reaches the tumor. However, a large body of work has demonstrated feasibility for targeting and imaging various cleaved antigens [231–234]. Herein, we developed a MUC16-targeted NIR fluorescent antibody probe and demonstrated its efficacy in delineating pancreatic cancer intraoperatively in vitro and in vivo by FGS. AR9.6-IRDye800 imaging resulted in significantly higher tumor signal compared to an IgG-IRDye800 control. Enhanced tumors could be distinguished from healthy tissue and key background organs relevant to pancreatic cancer. AR9.6-IRDye800 guidance also enabled the detection of micro-metastatic lesions in an orthotopic xenograft tumor model. This data suggests that AR9.6-IRDye800 has the potential for clinical translation as a probe for surgical resection of pancreatic cancer.

Chapter 3: Determining Translational Potential with huAR9.6-IRDye800 for FGS

3.1 Introduction

Pancreatic cancer is currently the fourth leading cause of cancer-related deaths in the United States, and has an extremely low 5-year survival rate of 10% [1]. Globally, the incidence of pancreatic cancer-related deaths is projected to increase, with predictions that pancreatic cancer will be the second leading cause of cancer-related deaths by 2030 [235, 236]. Surgery remains the only potentially curative option for patients with this disease, but only 20% of pancreatic cancer patients have resectable disease at the time of diagnosis [237]. However, an additional 30% of patients present with borderline resectable or locally advanced disease, in which the tumor either abuts or invades adjacent vasculature and may involve locoregional lymph nodes, but has not yet spread to distant organs. Neoadjuvant therapy has become increasingly implemented for this subset of patients in an effort to downstage tumors, decrease disease complexity, and increase eligibility for surgery [238, 239]. Under current standard of care chemotherapy regimens, neoadjuvant therapy has shown initial efficacy in substantially increasing patient eligibility for resection [240–244]. Therefore, surgical resections continue to impact a growing patient population in a cancer that has no other potentially curative treatment options, highlighting the importance of successful resections.

Pancreatic cancer surgeries are complicated by infiltrative disease, peritumoral inflammation, and dense desmoplastic stroma, and surgeons are limited by visual and tactile clues to differentiate normal tissue from cancerous tissue [2, 198, 245]. While many preoperative imaging modalities like MRI, CT, PET, and ultrasound can provide initial staging and diagnostic information, translating these images to the intraoperative setting can be difficult, resulting in missed lesions. Furthermore, in the context of

neoadjuvant therapy, traditional imaging modalities like CT may be unreliable in determining resectability and staging of PDAC, due to limitations in differentiating treatment-induced fibrosis from infiltrative disease [246, 247]. Since therapeutic response and the presence of additional lesions may alter the course of treatment for the patient and preclude them from initial surgery, or may lead to disease recurrence, identification of the extent of the disease during surgery is of critical importance. R1, or incomplete resections occur at high rates, reported as high as 70%. R0, or complete resections, in which there is a distance greater than 1 mm between the tumor and the surgical margin, have demonstrated an improved survival benefit [195]. Currently, up to 85% of patients that undergo surgical resection succumb to disease recurrence, due to both undetected lesions, and incomplete resections. Thus, there is an unmet need for intraoperative methods to detect lesions for surgical resections in pancreatic cancer.

Fluorescence-guided surgery (FGS), or the use of fluorescent contrast agents and cameras in the surgical suite to detect tumors, has demonstrated efficacy for intraoperative identification of cancer in many clinical trials for a variety of cancer types. Several clinical trials have been conducted investigating FGS for PDAC, and have demonstrated initial safety, efficacy, and feasibility for improved surgical resections [2, 3, 200]. These studies have largely employed antibody-based probes to target specific biomarkers for imaging of pancreatic cancer. However, due to the characteristic heterogeneity of pancreatic cancer, several of these studies have suggested a need for additional biomarkers to be investigated for FGS to increase available targeted agents. In our preliminary studies, we showed that MUCIN16, or MUC16, a glycoprotein that is expressed in 60-80% of pancreatic cancers, has potential as a novel target for FGS of pancreatic cancer with a murine MUC16-targeted antibody conjugated to a NIR dye, termed AR9.6-IRDye800 [190]. Our initial studies showed significantly improved contrast enhancement of tumors with AR9.6-IRDye800 as compared to a non-specific IgG control

in subcutaneous and orthotopic mouse models. Following recommendations for the development of optical imaging agents, the resulting data from this agent warranted further investigation to refine and evaluate the agent for clinical translation [211].

Herein our objective was to improve translational potential, assess the preclinical efficacy of AR9.6-IRDye800 to support potential clinical translation, and to investigate the role of antigen expression and tumor microenvironment on accumulation and contrast. To that end, we developed a humanized variant of this antibody conjugate to minimize potential immunogenicity and undesirable adverse reactions [224]. We assessed this agent for feasibility of clinical translation by optimizing the dye to protein ratio *in vitro* and *in vivo*, and dynamic contrast enhancement over time. To address the impact of variable biomarker expression on tumor contrast, we evaluated three subcutaneous tumor models with differential expression of MUC16. Finally, we incorporated a patient-derived xenograft model to recapitulate clinical disease presentation and critically evaluate the efficacy of utilizing huAR9.6-IRDye800 for FGS. The results of this study provide further evidence of the success of huAR9.6-IRDye800 as an imaging agent and demonstrate the potential of this agent as a probe for FGS of pancreatic cancer.

3.2 Materials and Methods

3.2.1 Cell Culture:

Pancreatic cancer cell lines including HPNE, T3M4, and Colo357 were obtained 2/2018 from Dr. Michael A. Hollingsworth. OVCAR3 cells were obtained 3/2018 from Dr. Adam Karpf. Panc1 cells were obtained 8/2019 from Dr. Joyce Solheim. All cells were grown in RPMI 1640 (Corning, 10–040-CV; Tewksbury, MA), supplemented with 10% fetal bovine serum, 100 I.U./ml penicillin, and 100 µg/ml of streptomycin (P/S) (Corning, 30–002-CI). Cells were maintained at 37° C in a humidified incubator with 5% CO_2. Cells

were regularly tested for mycoplasma (Myco-Sniff Mycoplasma PCR Detection Kit, 093050201, MP Biomedicals; Irvine, CA).

3.2.2 Antibody Conjugation

HuAR9.6 was conjugated to IRDye800 N-hydroxysuccinimide (NHS) ester (0.5 mg, LI-COR Biosciences, 929-70020; Lincoln, NE) according to the instructions of the manufacturer. Briefly, 100 µl of 1 M potassium phosphate was added to each mg of antibody to raise the pH to 8.5. Dye was dissolved in 50 µl of nanopure water and added to 1 mg of antibody and incubated for 2 hours at room temperature. Addition of 0.12 mg of dye consistently resulted in ~1:1 dye:protein. Excess dye was removed by Zeba spin desalting columns (ThermoFisher Scientific, 89891). Antibody diluted 1:5 in 1:1 PBS:methanol was loaded into a 1 cm cuvette (Eppendorf, E0030106300; Hauppauge, NY). Conjugation ratios were determined spectrophotometrically with a Thermo Scientific Evolution 220 UV-visible spectrophotometer, and fluorescence was confirmed with a FluoroMax 4 spectrofluorometer (Horiba Scientific; Irvine, CA). An SDS page gel (4-20% gradient gel, Bio-Rad, 4568094; Hercules, CA)) was run to confirm that free dye had been removed. 0.5 µg of AR9.6-IRDye800 conjugates at increasing dye:protein ratios and free unconjugated IRDye800 control (LI-COR Biosciences, 929-08972; Lincoln, NE) were loaded onto the gel, and gel was run at 90-125V. Gel was immediately imaged on the LI-COR Odyssey® M imaging system in the 800 nm channel.

3.2.3 Binding Assessment

Binding of murine, chimeric, and humanized antibody and antibody conjugates to recombinant MUC16 were assessed with an ELISA in which a 96 well plate (Fisher Scientific, 21-377-203; Waltham, MA) was coated overnight at 4° C with recombinant MUC16 antigen (100 ng of Trx-TEV-TR6-SEA5-TR4 in PBS). The plate was blocked with BSA (1% in PBS, 1 h, room temperature). Primary antibody was added at a starting

concentration of 100 nM and serially diluted (5-fold in PBS + 0.1% tween-20) down the plate and incubated (1 h, RT). The plate was washed 5 times (PBS + 0.1% Tween-20). Secondary antibody (1:40000 dilution, Anti-human IgG Kappa Horseradish Peroxidase, B7466, Novus Bio-techne; Littleton, CO) was added and incubated for 1h at RT, and the plate was washed again. TMB Substrate Solution (Thermo Scientific, N30; Waltham, MA) was added and incubated for ~ 30-60s and developed by the addition of an equal volume of 0.18 M Sulfuric Acid. The plate was read at 450 nm and 540 nm on a plate reader. For estimation of apparent antibody affinity, (EC50), the log concentration of antibody was plotted vs. absorbance and fit to a four-parameter logistic curve in GraphPad Prism (Graph Pad Software).

3.2.4 Western Blotting

Cells were lysed with radioimmunoprecipitation assay (RIPA) buffer (ThermoFisher Scientific, 89900) supplemented with Halt protease inhibitor (ThermoFisher Scientific, 78440). 20 µg of protein were separated on a 4–20% polyacrylamide gel (Bio-Rad, 4568094; Hercules, CA) and transferred onto a nitrocellulose membrane (Bio-Rad, 1620115). The membrane was blocked with 5% Blotting-Grade Blocker (Bio-Rad, 170–6404) in TBST and incubated with humanized AR9.6 (1:1000, 1 mg/ml stock solution) and GAPDH antibody (1:2000, Cell Signaling Technology, 2118S; Danvers, MA) overnight at 4° C. The membrane was incubated with goat anti-rabbit HRP secondary antibody for detecting the GAPDH loading control (1:5000, Jackson Immunoresearch, 115–035-144; West Grove, PA), and goat anti-human HRP secondary antibody to detect huAR9.6 (1:5000, Jackson Immunoresearch, 109–035-003). Secondary antibodies were diluted in 5% Blotting-Grade Blocker for 1 h on a rocker and were visualized with enhanced chemiluminescent (ECL) substrate (Bio-Rad, 1705060S).

3.2.5 Fluorescent Microscopy

HPNE, Colo357, and OVCAR3 cells were seeded at 30,000–40,000 cells per chamber of an 8-chamber slide (ThermoFisher Scientific, 154534), and allowed to adhere overnight. Cells were washed 3x with 1X PBS and blocked with 3% BSA in TBS for 1 h at room temperature. 5 µg/ml of AR9.6-IRDye800 was incubated with cells for 1 h at room temperature in 3% BSA in TBST. Cells were washed 3x with PBS. 1 µg/ml of Hoescht 3342 stain (ThermoFisher, 62249) was added to cells, and cells were imaged in Live Cell Imaging Buffer (ThermoFisher, A14291DJ). Cells were imaged at 200X magnification on an Olympus DP80 Digital Camera and cellSens Dimension software. For antibody internalization studies, AR9.6-IRDye800 was conjugated to pHrodo™ iFL green (ThermoFisher, P36015) dye according to the instructions of the manufacturer. Colo357 cells were plated at 35,000 cells/ well of an 8-well plate as described above, and blocked with 3% BSA in PBS. Cells were incubated with 5 µg/ml of the pHrodo™ iFL-labeled antibody. After 24 hours of constant incubation, cells were washed 3X with PBS, incubated with 60 nM of Lysotracker dye for 1 hour, and washed again before imaging in Live Cell Imaging Buffer (ThermoFisher, A14291DJ). Internalization of the antibody was observed in the FITC channel. Cells were imaged at 200X magnification as described above.

3.2.6 Animal Models

All animal work was performed under a protocol approved by the UNMC Institution of Animal Care and Use Committee IACUC. Subcutaneous tumor models were generated by injecting 1×10^6 T3M4 or 1.5×10^6 Colo357 or Panc1 cells suspended in 100 µl of 1:1 media and Matrigel (Corning, 356234) into the left flank of 6–8 week old male NU/J mice (Jackson Laboratories, 002019; Bar Harbor, ME). T3M4 tumors were allowed to grow for ~11 days, and Colo357 and Panc1 tumors were allowed to grow for ~30 days.

A patient-derived xenograft model (J000115419, passage 4) was obtained from Jackson Laboratories. The PDX model was delivered in a female NSG mouse (NOD.Cg-Prkdcscid Il2rgtm1Wjl/SzJ, 005557), screened for pathogens and confirmed to be pathogen and opportunist free. Tumor was initially engrafted on June 30th, 2021. Tumor was resected at ~1000 m^3 in size (approximately 7 weeks after initial engraftment) and propagated in recipient 6-8 week old female NSG mice according to protocols provided by the manufacturer [248].

3.2.7 Optimal Dye: Protein Ratio Assessment:

6–8-week-old female CD-1 mice (Charles River, Crl:CD1(ICR); Wilmington, MA) were injected via tail vein with 50 µg of huAR9.6-IRDye800, conjugated with either 0.3, 1, 2, or 4 dyes per protein. Conjugate was allowed to circulate for 48 hours post-injection. Cardiac punctures and necropsies were conducted, and organs were imaged on the LI-COR Pearl whole animal imaging system. Organs were quantified in Image Studio as previously described [190].

3.2.8 Dynamic Contrast Enhancement:

6-8 week old male NU/J mice were injected subcutaneously with T3M4 ($1x10^6$), COLO357 ($1.5X\ 10^6$), or Panc1 ($1.5X\ 10^6$) cells in 50% Matrigel in the left flank. After tumor formation, 50 µg of huAR9.6-IRDye800 was injected via tail vein. Mice were imaged from 4 hours post-injection up to 9 days with the LI-COR Pearl whole animal imaging system. TBR and Signal to noise ratios SNR were calculated as previously described [190, 206]. After 9 days, mice were euthanized, and necropsies were conducted. Necropsied organs were imaged on the LI-COR Pearl.

3.2.9 Immunohistochemistry

Paraffin-embedded tissues were cut into 4 µm thick sections and placed on glass microscope slides (Fisher Scientific, 22-037-246; Waltaham, MA).

Immunohistochemistry was conducted as described elsewhere. OC125 staining was conducted according to the instructions of the manufacturer (Roche, 760-2610; Basel, Switzerland). Staining of cell line xenografts was conducted with rabbit polyclonal CA125/MUC16 antibody, as both mouse and human antibodies had high background staining (Novus, 25450002; Littleton, CO). Antigen retrieval was conducted with 10 mM citrate buffer, pH 6, for 20 minutes in a rice cooker between 95-100º C. Samples were blocked for 45 minutes with 10% goat serum in TBS, and primary antibody (1:1000) was incubated with samples overnight at 4º C in TBS with 5% goat serum. Goat-anti rabbit HRP secondary antibody (1:1000, Jackson Immunoresearch, 115–035-144) was added for one hour in TBS with 5% goat serum at room temperature. Impact® DAB substrate (Vector Laboratories, SK4105; Burlingame, CA) was added to tissues for ~4 minutes. Tissues were washed and counterstained with Hematoxylin (IHC World, IW-1400; Ellicott City, MD), and imaged on the Olympus DP80 digital microscope with cellSens Dimension software. Staining of murine tissues for MUC16 expression was conducted with huAR9.6 (Quest PharmaTech; Edmonton, Canada). Antigen retrieval was conducted as described above. Primary antibody incubation (1:150) was conducted overnight at 4º C, and goat-anti human HRP secondary antibodies (1:1000 Jackson Immunoresearch, 109–035-003) were incubated with the samples for 1 hour at room temperature.

3.2.10 Fluorescence-Guided Surgery

NSG mice were implanted with PDX tumor model subcutaneously. Tumors were allowed to propagate for 21 days. When tumors reached 200-300 mm^3, 50 µl of huAR9.6-IRDye800 (dye:protein 1:1) were diluted into PBS for a total injection volume of 100 µl, and injected via tail vein. Images were collected daily using the LI-COR Pearl® Trilogy. Mice were euthanized 72 hours post-injection, and tumors were resected under image guidance using the Fluobeam 800 (Fluoptics; Cambridge, MA), and the Lab Flare

RP1 (Curadel; Natick, MA) FGS systems. Interim images and videos were collected during surgical resection. Necropsies were subsequently conducted, and resected tumors and organs were imaged on the LI-COR Pearl. Fluobeam images were analyzed to calculate intraoperative TBR using Image J software (version 1.52a, NIH; Bethesda, MD). Resected tumors were either frozen in OCT, or formalin-fixed and paraffin embedded for histological analysis.

3.2.11 Statistical Analysis

All statistical analyses were conducted using Graph Pad Prism software. Nonlinear regression was used to analyze data from ELISA assays for binding of huAR9.6 and huAR9.6 conjugates. A Two-way ANOVA was implemented, followed by Tukey's test for multiple comparisons to compare differences in mean fluorescent signal in resected organs, and to compare TBR between Panc1, T3M4, and Colo357 tumor models. All values are reported as the mean ± standard deviation.

3.3 Results

3.3.1 HuAR9.6 and HuAR9.6-IRDye800 Bind MUC16

Our previous studies developed a MUC16-targeted FGS agent that utilized a murine antibody as a targeting moiety [190]. However, the use of murine antibodies has limited translational potential [249]. Patients injected with murine antibodies have a rapid human anti-mouse antibody response (HAMA), which can cause adverse allergic reactions, increase clearance, and impact tumor penetration [224]. To improve the translational potential of AR9.6 and minimize the potential immunogenicity from a murine antibody, a humanized antibody, huAR9.6, was developed using complementary determining region (CDR) grafting techniques (C.B). Humanized AR9.6 binding was compared to chimeric and murine variants and showed no significant differences in binding recombinant MUC16 **(Figure 18A)**. This suggests that the process of

humanizing this antibody did not impact the affinity of huAR9.6 for MUC16. To further confirm the retained affinity for MUC16, a western blot was conducted, shown in **Figure 18B**, which demonstrated that the huAR9.6 variant bound MUC16 in MUC16-expressing pancreatic cancer cell lysates, as well as in lysates of a MUC16-expressing ovarian cancer cell line (OVCAR3) positive control, consistent with western blots previously conducted with the murine AR9.6 variant [190]. Binding was not observed in HPNE negative control cells.

HuAR9.6 was conjugated to IRDye800CW NHS Ester at varying ratios of 0.3, 1, 2, and 4 dyes per protein (**Figure 19A**). To determine if increasing dye to protein ratios had any impact on binding, an ELISA was conducted. The results from this assay in **Figure 19C** showed that there were no significant differences in binding of the conjugates to recombinant MUC16 regardless of the dye to protein ratio. This is an important consideration, especially since the methodology used for conjugation herein was non-specific, and dyes could be conjugated near antibody-binding regions, thus impacting affinity. The range of dye to proteins was selected based on upper and lower limits of ratios used with other antibody-based probes, both preclinically and clinically in the literature [3, 200, 250]. Analysis of samples on an SDS-PAGE gel, shown in **Figure 19B**, confirmed that the absence of free dye in all of the varying dye:protein conjugates. Fluorescent microscopy was conducted, as shown in **Figure 20**, to demonstrate binding of huAR9.6-IRDye800 to pancreatic cancer cells. Furthermore, internalization of huAR9.6-IRDye800 was observed via fluorescence microscopy in cells after 24 hours **(Figure 21).**

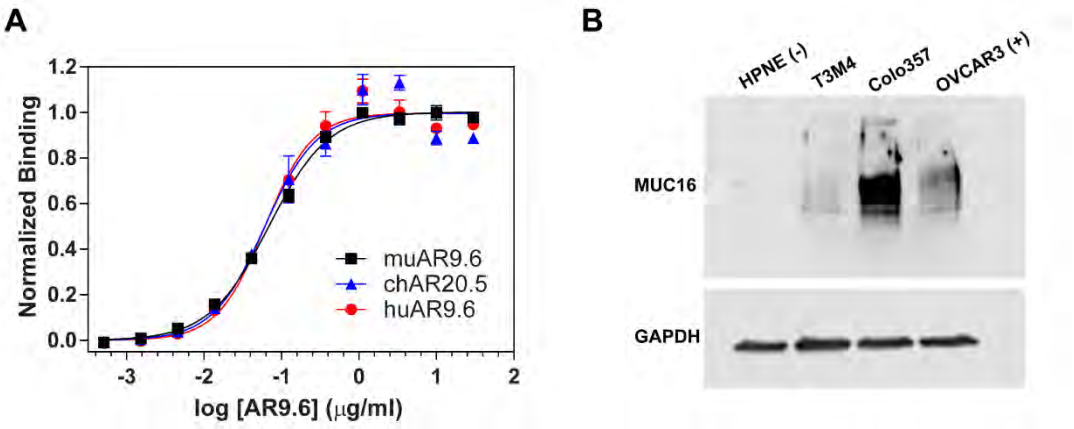

Figure 18: (A) Humanized, chimeric, and murine AR9.6 binding to recombinant MUC16 **(B)** Binding of huAR9.6 to human pancreatic cancer cell lines.

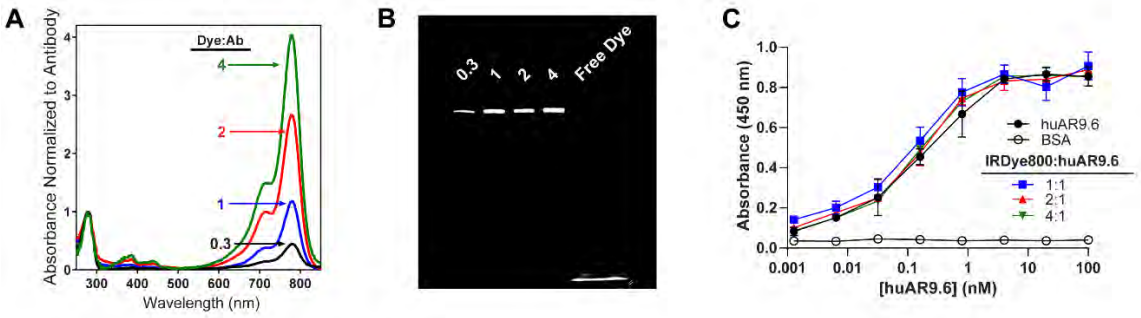

Figure 19. Characterization of huAR9.6-IRDye800 conjugates. **(A)** Representative absorbance spectra from huAR9.6-IRDye800 at 0.3,1,2, and 4 dyes: protein. **(B)** SDS page of huAR9.6-IRDye800 at various dye: protein ratios. **(C)** Binding of huAR9.6-IRDye800 conjugates to recombinant MUC16 via ELISA.

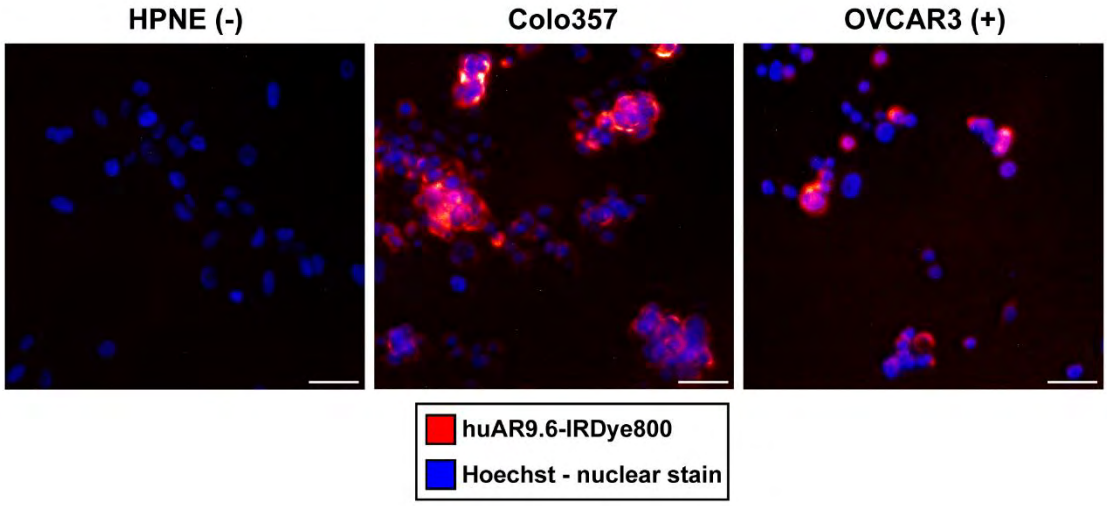

Figure 20: Fluorescence microscopy of huAR9.6-IRDye800 binding to human pancreatic cancer cells.

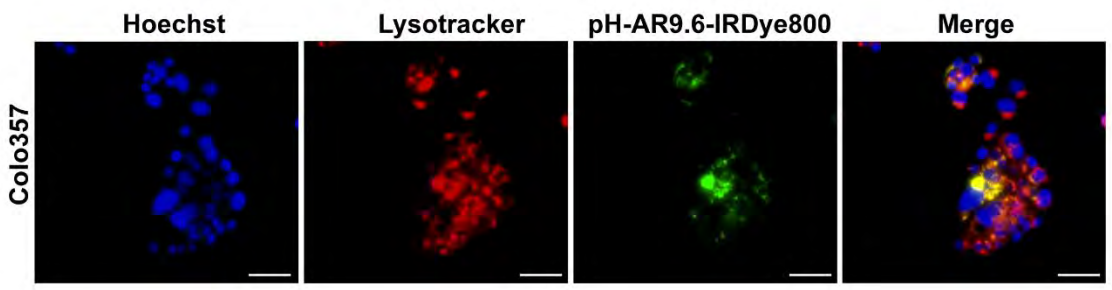

Figure 21: Internalization of huAR9.6-IRDye800 within MUC16 expressing PDAC cells after 24 hours.

3.3.2 Impact of Dye to Protein Ratio on Biodistribution

While increasing dye to protein ratios did not impact binding to recombinant MUC16 protein *in vitro*, the impact of conjugation ratios *in vivo* necessitated evaluation. Reports in the literature have suggested that dye:protein ratios can significantly impact pharmacokinetics and distribution of fluorescently labeled IgGs [124, 251, 252]. Most importantly, these reports have shown that liver signal is significantly increased with increased dye:protein ratios greater than 1 D:P. This is a critical factor to consider for imaging pancreatic cancer because the liver is a key background organ for imaging, as well as a site of frequent metastasis [253]. Thus, it is critical to keep background signal in the liver as low as possible in order to minimize interference with primary tumor detection, and to assist in potentially identifying metastatic lesions. To optimize the dye:protein ratio for huAR9.6-IRDye800, the overall biodistribution of a no-injection control was compared to antibody equivalent (50 µg) injections of 0.3, 1, 2, and 4 dyes:protein after 48 hours of circulation. Representative images of the necropsied organs shown in **Figure 22** highlight the increase in liver signal observed with increasing dye:protein ratios, consistent with previous reports. The quantified mean fluorescent signal in each resected organ shown in **Figure 23** further exemplifies the significant increase in liver signal with increasing dye to protein ratios. However, minimizing the impact of conjugate ratio on biodistribution has to be considered in conjunction with sufficient signal for tumor detection on imaging systems. Other reports have shown sufficient detection with 1:1 dye:protein ratios [254]. Resected clearance organs were compared under multiple imaging systems to demonstrate the variability in signal with different dye to protein ratios. Resected organs under Fluobeam and Curadel imaging are shown in **Figure 24** and **Figure 25** to offer a comparison of the differences in key background organs under differing imaging systems. Current dye:protein ratios used in clinical trials for IRDye800 agents were also considered in the evaluation of huAR9.6-

IRDye800. The majority of dye:protein ratios for IRDye800-conjugated antibodies used in clinical trials ranged from 1 to 2 [3, 200, 250]. In order to minimize the impact of dye:protein ratios on biodistribution, retain sufficient signal for deep seated tumors, and maintain consistency with current clinical trials, a dye:protein ratio of 1:1 was chosen for further investigation in this study.

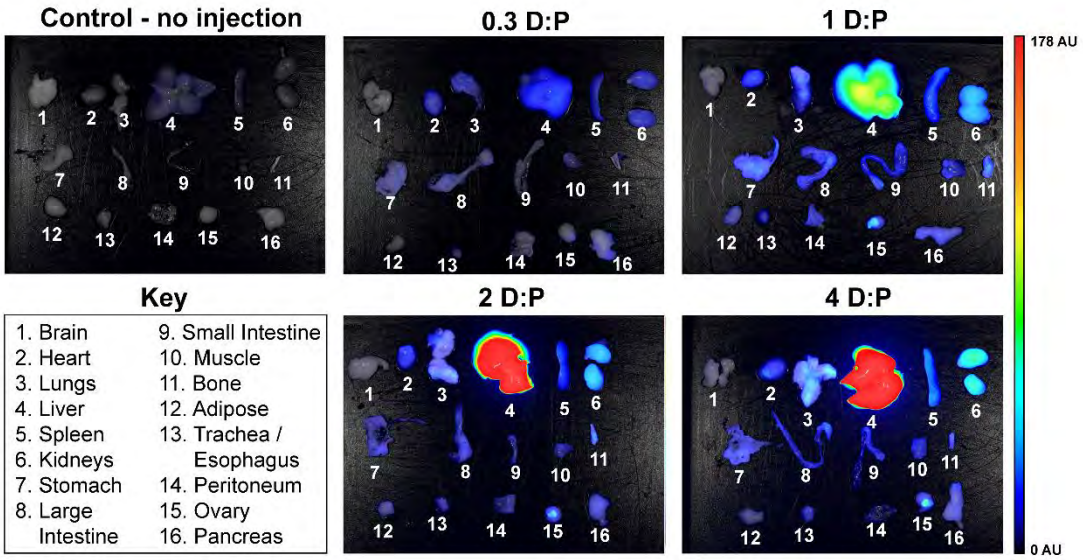

Figure 22: Representative images from necropsied organs 48 hours after injection of control (no injection), or 50 µg or 0.3, 1, 2, or 4 dye:protein huAR9.6-IRDye800 (N=5).

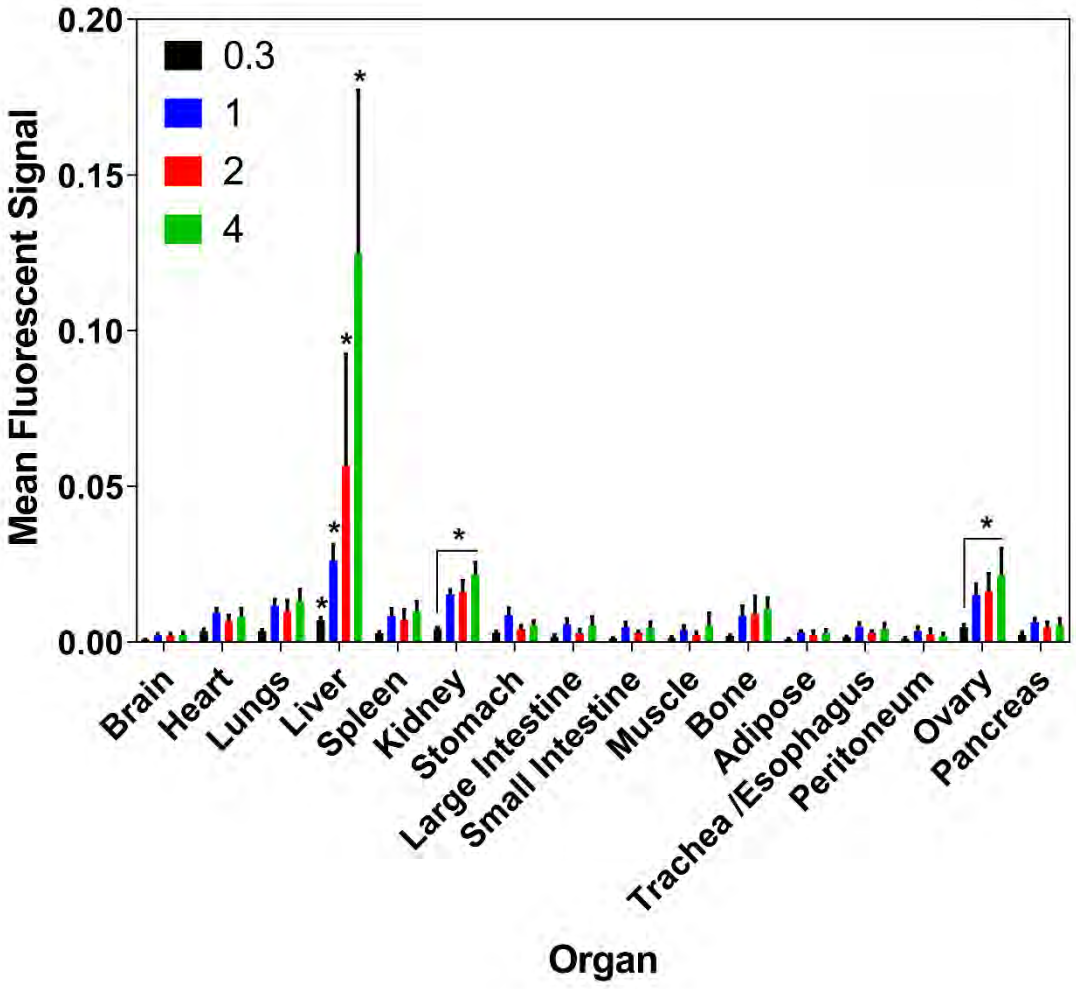

Figure 23: Quantified signal from organs resected 48 hours after injection with a control (no injection) or 50 µg of 0.3, 1, 2, or 4 dye:protein of huAR9.6-IRDye800. (N=5)

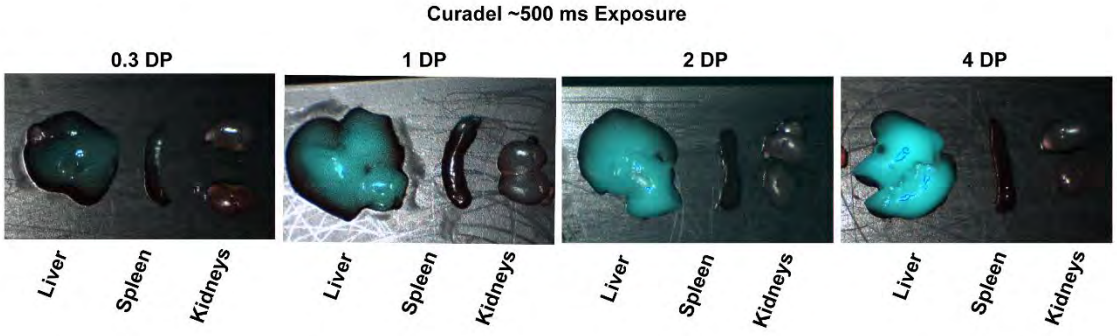

Figure 24: Key clearance organs from varying dye to protein ratios imaged with the Curadel Image Guided Surgery System.

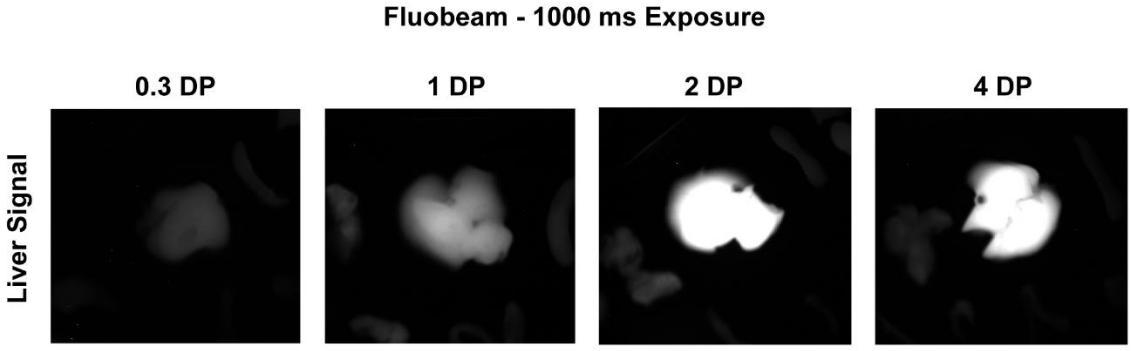

Figure 25: Signal from resected livers with 0.3, 1, 2, and 4, dye:protein ratios, under Fluobeam imaging.

3.3 3 Dynamic Contrast Enhancement and Role of Biomarker Expression in Accumulation of huAR9.6-IRDye800

To evaluate the tumor accumulation of huAR9.6-IRDye800 after injection, a dynamic contrast enhancement time course study was conducted. Three subcutaneous PDAC xenograft models were selected based on the *in vitro* expression of MUC16 as shown in **Figure 26. Figure 27** shows immunohistochemistry staining of MUC16 expression in each of the tumor models used. Panc1 cells do not express MUC16 *in vitro* and served as a biomarker negative control. This control was used to assess the impact of biomarker expression on tumor accumulation of huAR9.6-IRDye800. T3M4 and Colo357 served as the MUC16-expressing models. These cell lines were chosen in tandem because of their differential expression of MUC16. Colo357 cells expressed high levels of MUC16 *in vitro,* and T3M4 cells expressed moderate levels of MUC16. Mice were imaged for 9 days after the injection of huAR9.6-IRDye800 on the LI-COR Pearl. Representative images from each of the tumor models over time are shown in **Figure 28**. Results from the MUC16-expressing tumor cell lines were consistent with the results from muAR9.6-IRDye800, in that increasing tumor to background ratios were observed over time [190]. The biomarker control model, Panc1 **(Figure 28C)**, demonstrated significantly lower tumor to background ratios from 24 hours after injection until 9 days after injection as compared to both MUC16-expressing tumor models **(Figure 29)**. Current recommendations for the development of optical imaging probes suggest that a TBR of >3.0 in preclinical studies is a sufficient metric to warrant further investigation [211]. Tumor to background ratios with huAR9.6-IRDye800 were greater than 3.0 from 24 hours through 9 days, with peak TBRs reaching 6.95 ± 0.39 and 7.72 ± 1.96 for T3M4 tumors and Colo357 tumors respectively at 9 days post-injection. Comparatively, Panc1 MUC16-negative tumors had maximum TBRs of 1.93 ± 0.53 at 9 days post-injection. The significant differences in TBRs observed in MUC16-expressing compared to MUC16

-negative tumor models demonstrated the specificity of huAR9.6-IRDye800 for MUC16. However, considering MUC16 moderate-expressing (T3M4) and MUC16 high-expressing (Colo357) models did not have significantly different TBRs at most time points, TBR cannot be solely attributed to differences in biomarkers expression. Rather, factors such as tumor size and vascularity likely play a role in tumor to background ratio as well, as has been suggested in other FGS studies [255]. At 9 days post-injection, tumors and key clearance organs were resected. Representative images from each group and quantified signals from resected organs are depicted in **Figure 30**. At 9 days post-injection, tumor signal in MUC16-expressing tumors (Colo357 and T3M4) was significantly higher than in all resected clearance organs ($p<0.0001$). Conversely, Panc1 tumors that did not express MUC16 did not have significantly higher tumor signal compared to resected clearance organs. The optimal imaging time window for a given FGS agent should optimize high tumor to background ratios, low background signal, and sufficient overall signal for detection of lesions on multiple imaging systems [216]. To assist in the selection of an optimal imaging time window within the 9-day time frame investigated, a pilot interim necropsy study was conducted at 72 hours post-injection **(Figure 31)**. At 72 hours, tumor signal was much brighter than signal in key background and clearance organs. Fluorescence localization was observed macroscopically and microscopically in resected tumors at the 72-hour time point **(Figure 32)**. Based on the dynamic contrast enhancement study, current clinical trial procedures, and interim necropsy data, a range of 3-6 days was selected as an optimal imaging window for further studies.

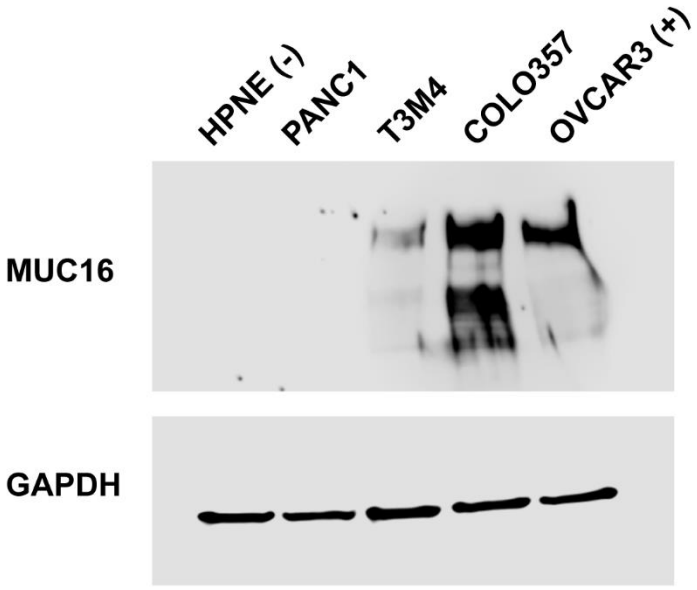

Figure 26: Expression of MUC16 in human PDAC cell lines evaluated for subcutaneous tumor models.

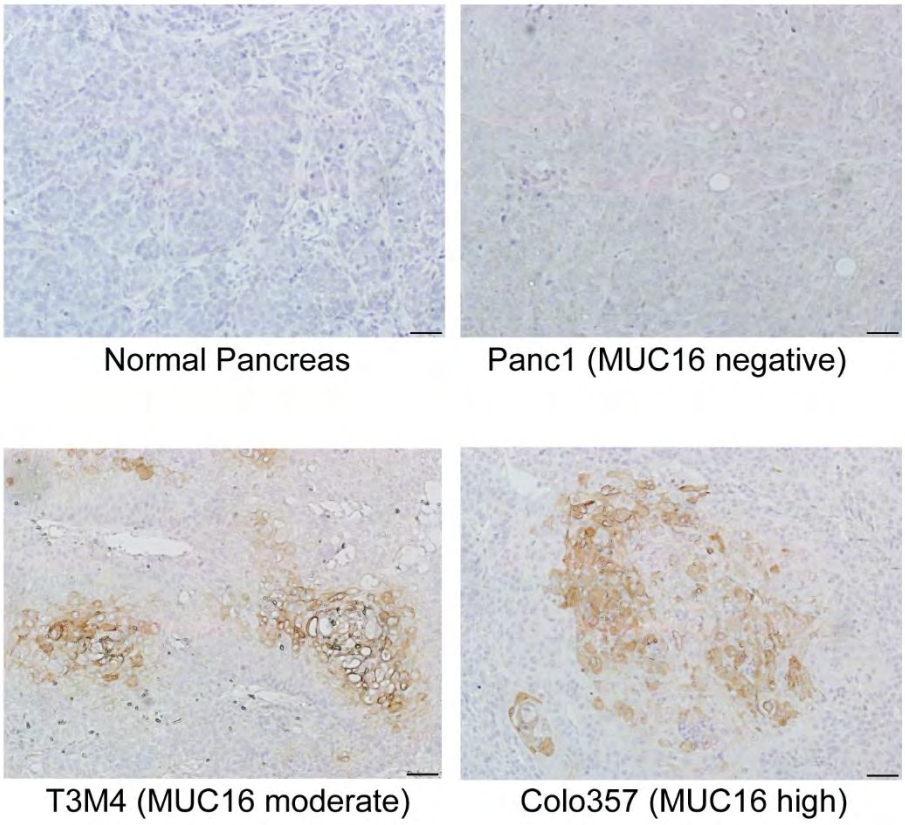

Figure 27: Expression of MUC16 in normal pancreas control and subcutaneous tumor models.

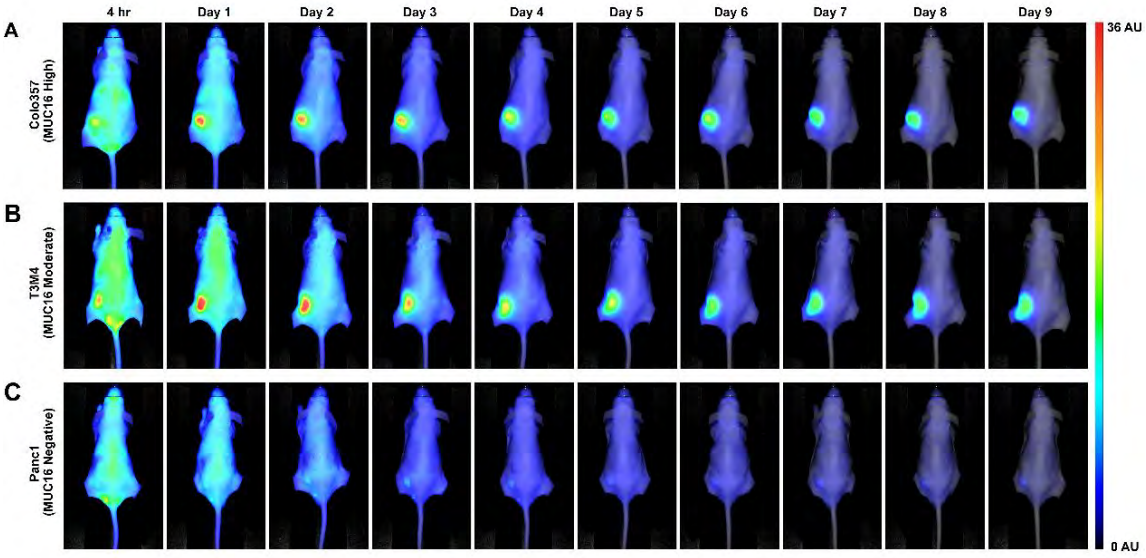

Figure 28: Dynamic contrast enhancement in mice bearing **(A)** MUC16 high-expressing Colo357 subcutaneous tumors **(B)** MUC16 moderate-expressing T3M4 subcutaneous tumors and **(C)** MUC16-negative Panc1 subcutaneous tumors. N=5.

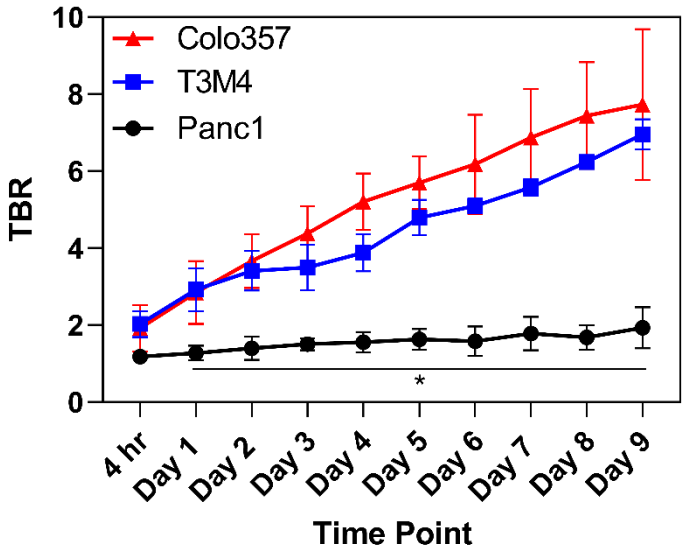

Figure 29: Tumor to background ratios in Colo357, T3M4, and Panc1 subcutaneous tumors over 9 days after injection. N=5.

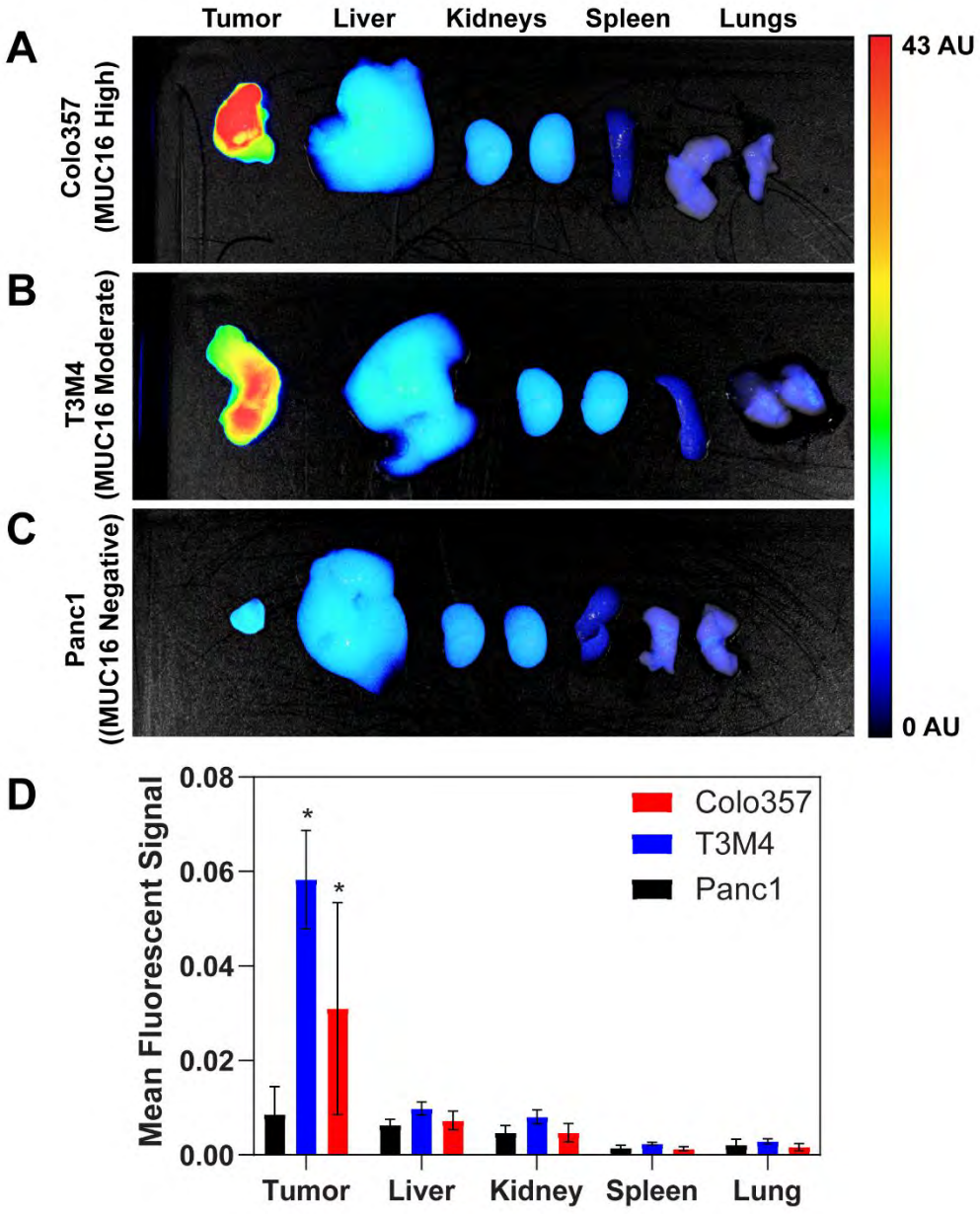

Figure 30: Biodistribution in key clearance organs 9 days post-injection of huAR9.6-IRDye800. **(A)** Representative images of resected tumors and key clearance organs from mice bearing Colo357 tumors. **(B)** Representative images of resected tumors and key clearance organs from mice bearing T3M4 tumors. **(C)** Representative images of resected tumors and key clearance organs from mice bearing Panc1 tumors. **(D)** Quantified mean fluorescent signal from resected organs. N=5.

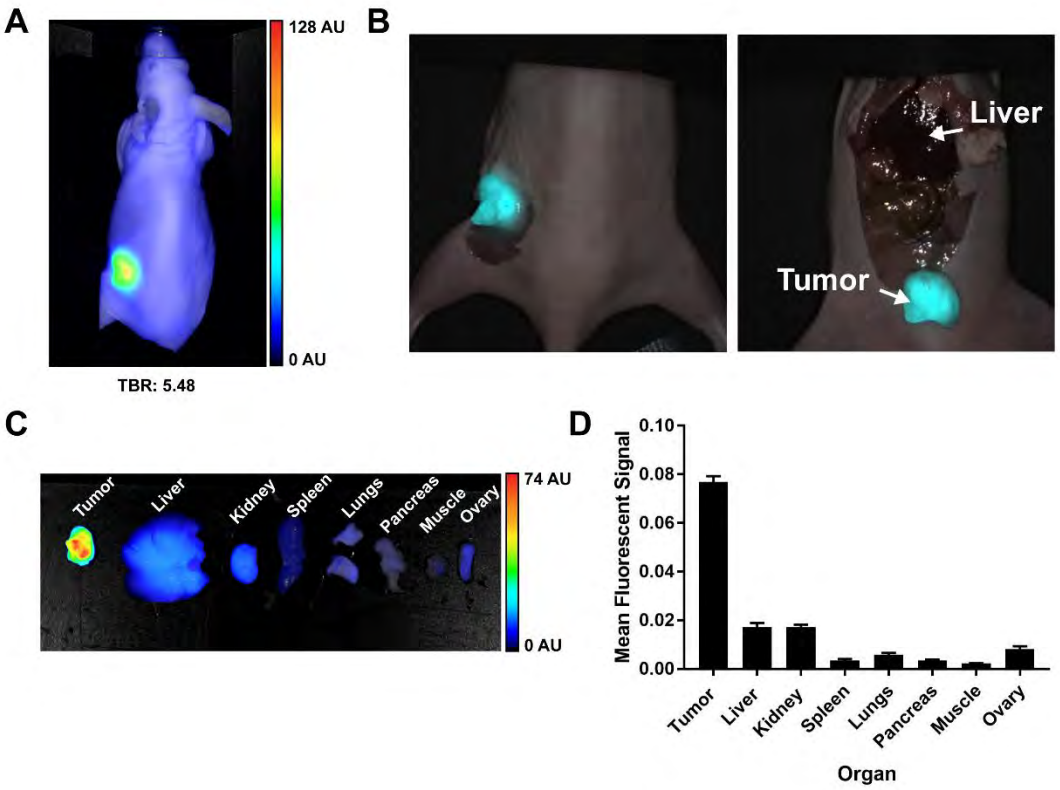

Figure 31: Interim necropsy conducted at 72 hours post-injection in T3M4 subcutaneous tumor model. **(A)** LI-COR imaging of mouse at 72 hours **(B)** Curadel Imaging of resected tumor **(C)** Necropsied organs **(D)** quantified signal from resected tumor and organs (N=2)

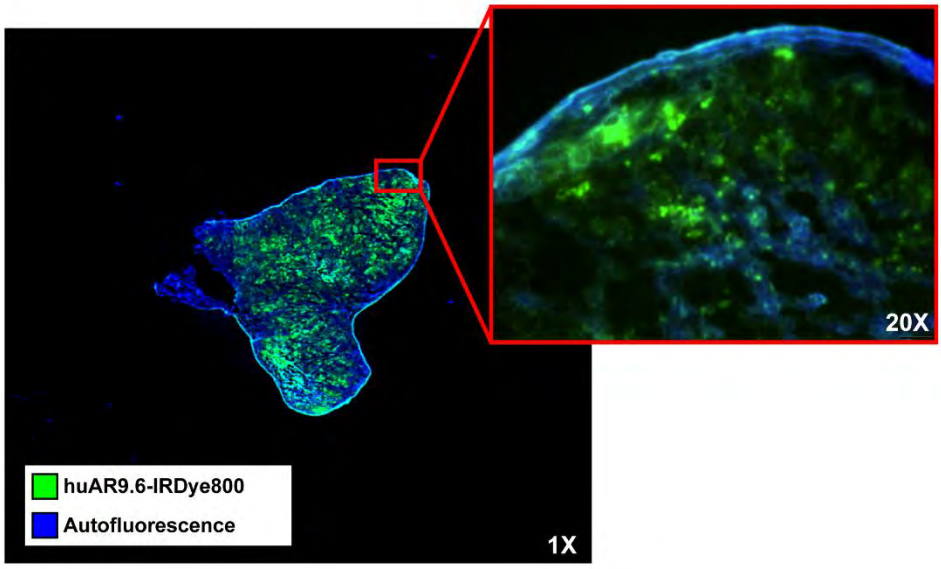

Figure 32: Macroscopic and microscopic imaging of huAR9.6-IRDye800 fluorescence localization in tumors 72 hours post-injection.

3.3.4 FGS

Translating fluorescent probes from preclinical studies into the clinic can pose many challenges. In pancreatic cancer, the depth of disease, tumor heterogeneity, and dense desmoplasia can complicate FGS and intraoperative tumor detection, but these disease characteristics are not frequently represented in preclinical models. A major weakness in preclinical testing of FGS probes is the overreliance on simplified xenograft models that have overwhelmingly high expression of the biomarker of interest [256]. While relying on such models is useful to show specificity of the targeting moiety, these models fail to recapitulate some of the complexities of tumor heterogeneity and surgical imaging that arise during clinical translation. Translation of FGS probes into the clinic introduces massive variation in tumors, including fluctuation in biomarker expression, degree of stroma, tumor vascularity, and disease localization. The use of patient-derived xenografts in preclinical studies may improve preclinical appropriation of clinical FGS by more closely recapitulating the tumor microenvironment as compared to single high biomarker expressing cell line xenografts. To better understand the impact of tumor complexity on intraoperative contrast and imaging, several patient-derived xenograft models from Jackson Laboratories were screened for MUC16 expression, as shown in **Figure 33**. Models varied in staining intensity and percent of cells expressing MUC16. Model J000115419 was selected, and images of this screened tumor specimen are shown in **Figure 34**. This tumor, diagnosed as pancreatic ductal adenocarcinoma, was resected during surgery from an 85-year-old male patient. Because this sample was surgically resected, this represented the key patient population in our study – patients eligible for surgical resection who could benefit from FGS. This tumor specimen was propagated in female NSG mice. Mice received injection of the contrast agent after tumors reached 200-300 mm3 in size.

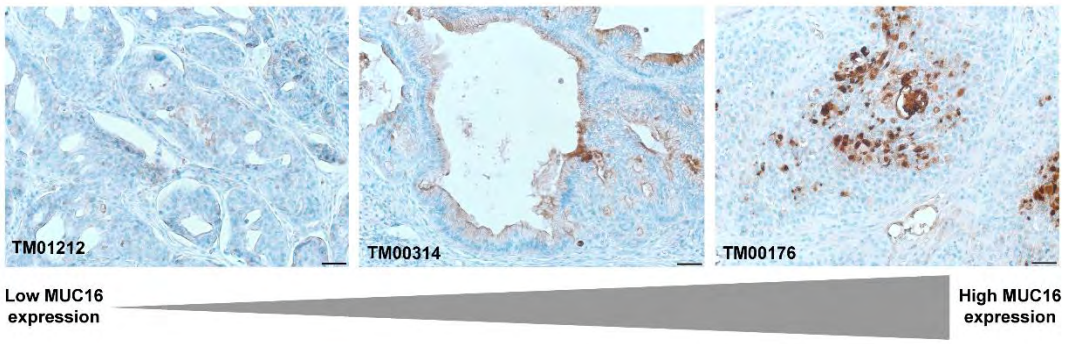

Figure 33: Representative pancreatic cancer PDX models screened from JAX, and analyzed for MUC16 expression (20X magnification).

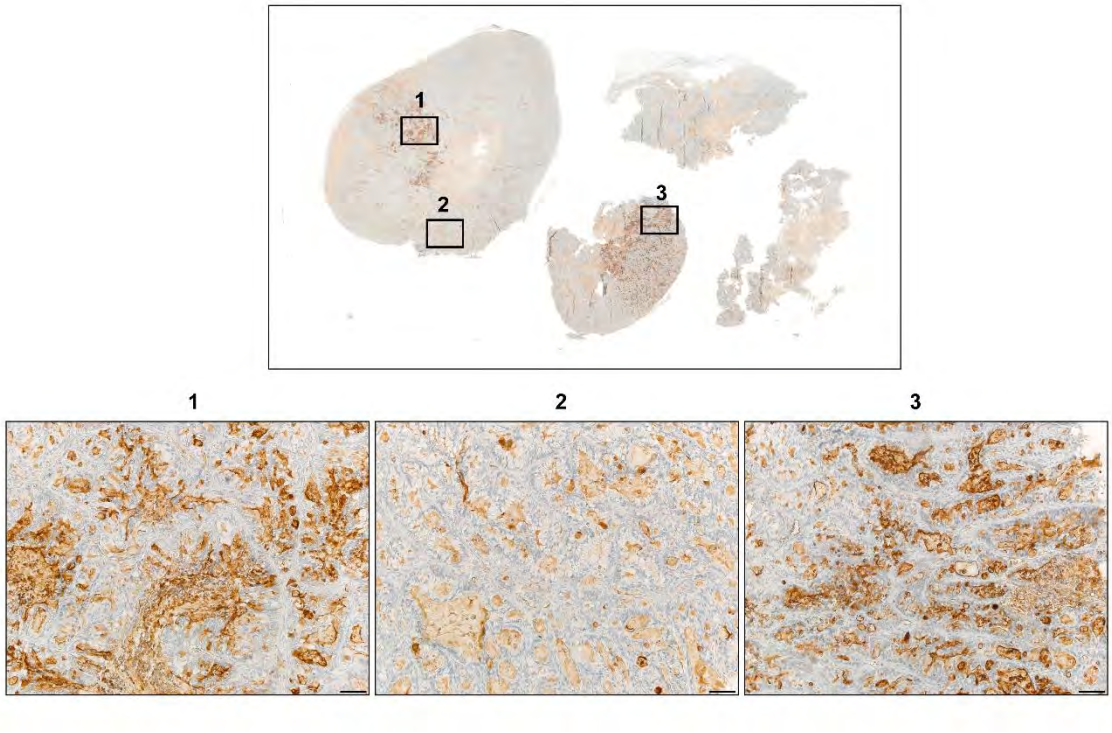

Figure 34: Images from selected tumor model J000115419 screened for MUC16 expression. (Top image taken at 1X magnification, bottom images taken at 20X magnification).

72 hours post-injection, mice were imaged on the Fluobeam, Curadel, Spectropen and LI-COR imaging systems described in **Figure 13**. Fluorescence localization was observed in subcutaneous tumors on all imaging systems, depicted by representative Curadel images in **Figure 35A** (N=3). Spectral analysis showed significantly higher fluorescent signal in the tumors as compared to pancreas ($p<0.0001$) as shown in **Figure 35B**, and represented by LI-COR images in **Figure 35C.** Fluorescence localization was also observed microscopically in frozen tumor sections, shown in **Figure 35D.** To analyze the tumor microenvironment and intratumoral distribution of huAR9.6-IRDye800, tumors were sectioned, stained, and analyzed by a board-certified pathologist (G.A.T). Tumor blocks were scanned on an Odyssey M slide scanner at 800 nm, shown in **Figure 36A,** and depicted homogenous pockets of huAR9.6-IRDye800 localization throughout the tumor. Tumors were diagnosed as moderately differentiated invasive pancreatic ductal adenocarcinoma. Tumor differentiation was homogenous throughout, and there were no regions of necrosis, as shown by H&E stain in **Figure 36B.** OC125, the gold standard antibody for detection of MUC16, showed 26-50% of cells positive for MUC16 **(Figure 36C)**. High expression was observed in secretions with 3+ staining intensity, and weaker membranous staining was also observed with 1+ staining intensity. Pattern of distribution of MUC16 was consistent with pattern of fluorescence localization observed on 800 nm scan of the tumor block. Masson's Trichrome stain was used to identify collagen within the tumor **(Figure 36D).** Wisps of collagen comprised approximately 5% of the total tumor mass, with homogenous localization around tumor glands. α Smooth muscle actin (SMA) stain (a myofibroblast marker), showed expression consistent with the patterns observed in Masson's Trichrome staining, with expression observed around glands, making up about 5% of the total tumor mass, suggesting that the stroma present was largely fibroblast-derived **(Figure 36E)**. CD31 (an endothelial marker commonly used to identify angiogenesis in

tumors) showed minimal to mild angiogenesis throughout the tumor, mirroring the hypovasculature characteristic of patients with PDAC **(Figure 36F)**. Ki67 staining showed variable expression of tumor cell proliferation with lower-expressing regions containing 50% positive cells, and higher regions with 80% positive cells **(Figure 36G)**.

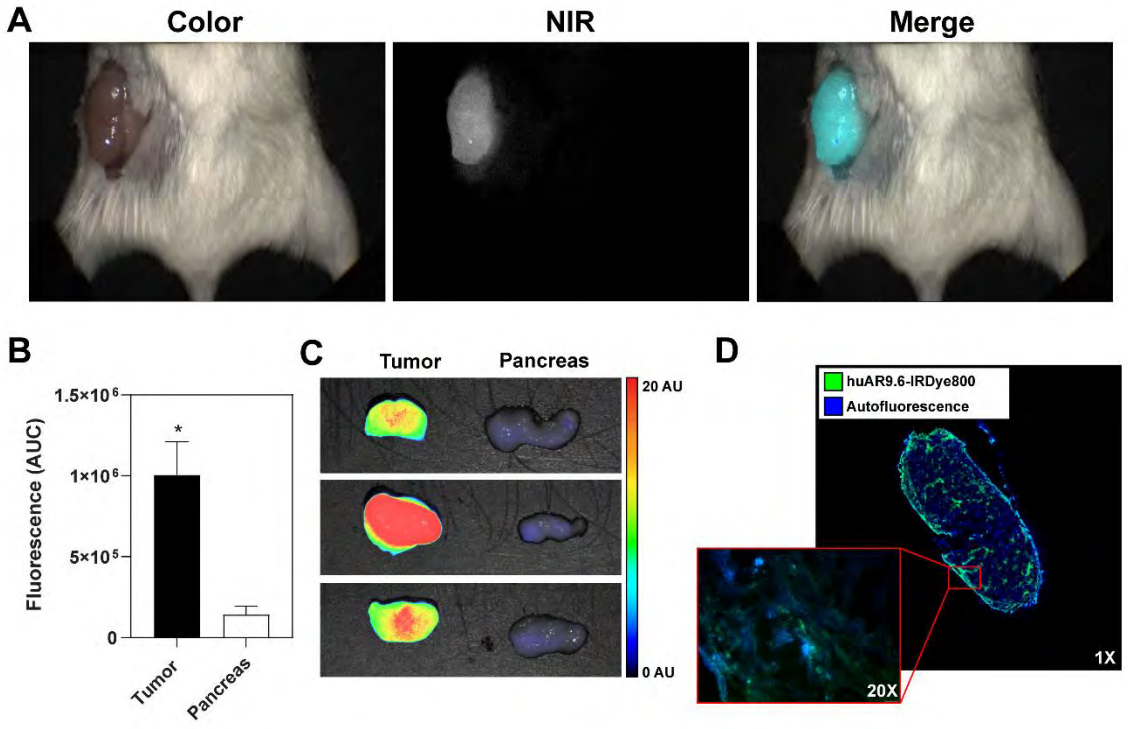

Figure 35. Fluorescence-Guided Surgery in a patient-derived xenograft model with huAR9.6-IRDye800. **(A)** Representative images from Curadel-guided resection. **(B)** Comparative fluorescent signal from tumor and pancreas **(C)** Representative LI-COR images of tumor and pancreas signal. **(D)** Miscroscopic fluorescence localization of huAR9.6-IRDye800. (N=3).

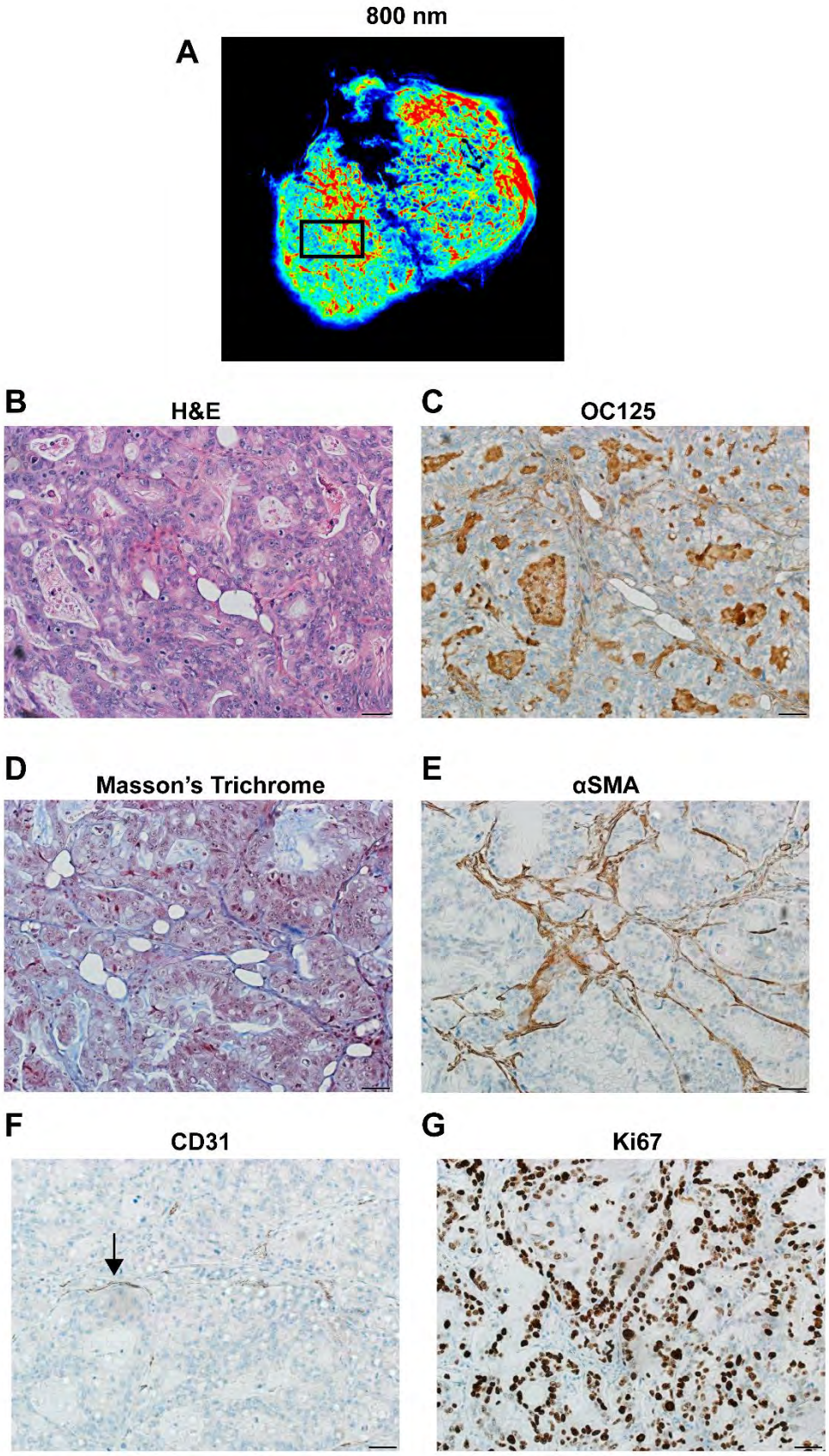
800 nm
A
B
H&E
C
OC125
D
Masson's Trichrome
E
αSMA
F
CD31
G
Ki67

Figure 36. Histological Analysis of Patient-Derived Xenografts. **(A)** 800 nm signal in PDX tumor (1X magnification) **(B)** H&E staining **(C)** OC125 staining for MUC16 expression **(D)** Masson's Trichrome staining to identify collagen expression **(E)** αSMA staining of myofibroblasts **(F)** CD31 staining of vascular proliferation **(G)** Ki67 staining of tumor proliferating cells (Images in B-G captured at 20X magnification).

3.4 Discussion

The objective of this project was to develop a humanized MUC16-targeted fluorescent antibody conjugate, huAR9.6-IRDye800, and demonstrate specificity toward MUC16, and efficacy in detecting PDAC intraoperatively, to further progress towards clinical translation. Because of the critical and potentially curative role of surgery and the limited number of fluorescent probes under development for FGS in pancreatic cancer, the goal of this work was to focus on the development of an FGS agent towards a novel target. MUC16 is a compelling potential biomarker for FGS. It is highly expressed among primary tumors in PDAC patients, in metastatic lesions common to pancreatic cancer, and in precursor (PANIN) lesions. It has little to no expression in benign conditions such as pancreatitis, which is critical for differentiating malignant disease, and reducing potential background signal from peritumoral inflammation [204]. Preliminary evidence in our laboratory (currently unpublished) has demonstrated that MUC16 expression is conserved after neoadjuvant therapy.

Expression of this protein on the surface of cells provides ease of access for targeting, and limited native expression provides a favorable biodistribution profile for minimized background signal for imaging. MUC16 is not expressed in the normal pancreas and is not expressed in critical background organs throughout the peritoneal cavity. MUC16 is also expressed in many other malignancies, and thus has potential applications as a tumor agnostic biomarker for targeted FGS. It has been well established as a serum biomarker in ovarian cancer, suggesting avenues for development of blood-based biomarkers for detection, patient stratification, and disease monitoring. These characteristics of MUC16 align with many of the reported criteria for development of successful FGS probes, and targeted agents [257–260].

However, as we continue to develop this probe for clinical translation, it is necessary to address the potential challenges and criticisms of targeting MUC16.

MUC16 can be cleaved from the cell and circulate within the blood stream. While this can be advantageous as a blood biomarker, this may pose a challenge for imaging. High levels of circulating MUC16 in the serum could bind the fluorescent antibody conjugate and reduce antibody available to bind tumors. This could cause high background and reduce tumor contrast. Current mouse models of tumors tend to be poor predictors of this phenomenon, as many studies have found that these tumor models fail to recapitulate circulating antigen [261]. However, there are many preclinical and clinical studies that suggest cleaved antigen is of minimal concern. Preclinical studies have shown successful imaging in the context of many cleaved antigens [227, 229, 258, 259]. Furthermore, the clinical success of SGM-101 as an imaging agent for FGS addresses this criticism. CEA, the target of SGM-101 can also be cleaved. However, quantification of fluorescent antibody bound to circulating antigen in patients after injection of the contrast agent showed only 3% of the total injected dose was sequestered in circulation, resulting in minimal impact on the tumor contrast [176]. Current SGM-101 studies excluded patients with serum levels over a certain threshold, but clinical data suggested that this exclusion criterion could be abandoned in future studies because of the minor impact of circulating antigen. It is also possible, as suggested by other reports investigating MUC16, that not all cleaved antigen circulates in the serum. In assessing PDAC patient MUC16 samples, it was observed in several samples that MUC16 may become trapped within the tumor (likely due to dense desmoplasia), leading to very high levels of intratumoral antigen. This phenomenon has been observed in ovarian cancer, where serum levels of MUC16 did not reflect tumor expression of MUC16, which investigators attributed to trapping of secreted MUC16 within the tumor [264–266]. Studies need to be conducted to see if circulating levels of MUC16 coincide with tumor expression of MUC16 in PDAC, in order to correctly stratify patients for huAR9.6-IRDye800. Given the large body of work demonstrating successful imaging of cleavable

antigens, we do not anticipate that this parameter will impede the efficacy of huAR9.6-IRDye800.

One of the critical aspects of FGS for PDAC not addressed within this project is the detection of metastases, including positive lymph nodes. Further studies are needed to investigate the minimum size of lesions that can be detected with FGS, since detection of occult metastases may alter the patient's course of treatment and they can be missed during preoperative imaging. Additionally, while MUC16 has little to no expression in pancreatitis, the effects of benign inflammatory conditions on detecting malignancies should be investigated. Finally, clinically available systems should be integrated to determine the detection capabilities for huAR9.6-IRDye800.

Overall, the results of this study support huAR9.6-IRDye800 as a potential agent for further development for FGS. Data showed that huAR9.6 retained its binding properties in comparison to the murine variant. Dye to protein ratios were optimized in this study and highlighted the impact of increasing dye ratios on liver accumulation. There is currently a lack of consensus in the literature on the optimal labeling ratio for near infrared dyes, but the results of the data shown herein, as well as in previous reports, highlight the impact of the degree of labeling on biodistribution [251]. Dye to protein ratios of 1:1 had minimal impact on distribution. The liver is both a key background organ in pancreatic cancer, as well as a site of frequent metastasis. Thus, it is paramount to diminish liver signal, and keeping dye to protein ratios low can assist in reducing background liver signal. However, this study did not investigate the detection of metastatic lesions, and so it has yet to be determined if liver lesions are identifiable even at lower dye to protein ratios used here. Furthermore, this dye to protein ratio needs to be assessed in tumor-bearing models on clinically used imaging systems to ensure that this ratio allows for adequate detection.

In vivo studies in subcutaneous tumor models showed high tumor to background ratios in MUC16 expressing tumors, and low tumor to background ratios in tumors that did not express MUC16. The results of this study confirm that fluorescence localization is due to the specificity of the probe for MUC16, rather than accumulation due to the EPR effect. However, it is important to note that these results are likely not entirely simplified to the presence or absence of MUC16. Considerations for differential vascularity and tumor size likely have a role in tumor to background ratio, as evidenced by several clinical studies [255]. However, these factors were not explored at length in this research project, and thus should be investigated at further in future studies.

Fluorescence guided surgery conducted in patient-derived xenograft tumors demonstrated that huAR9.6-IRDye800 could successfully delineate tumors. The tumor model used herein captured many characteristics of tumors observed in patients in the clinic. Cell line-derived tumor models are notoriously aggressive and poorly differentiated. Comparatively, the patient-derived xenograft model was moderately differentiated, which more accurately represented the grade of tumors frequently eligible for surgical resection. Furthermore, the patient-derived xenografts used herein exhibited hypovascularity, which mirrors the hypoxic environment characteristic of most PDACs. Stroma was present in this tumor as well. Despite the low degree of vascularity and presence of stroma, huAR9.6-IRDye800 still accumulated homogenously throughout the tumor, and illuminated the tumor for surgical resection.

However, while this PDX model more accurately recapitulates the tumor microenvironment of PDAC than cell line-derived tumor models, this model has limitations as well. Previous studies have shown that humanized antibodies exhibit analomous biodistribution in severely immunodeficient mice, such as NSG mice used herein, which can decrease tumor uptake, and increase background signal in the liver, spleen, and bone [264]. This pattern of altered biodistribution was also observed here,

with increased peritoneal signal. Tumor contrast was still very bright, but may have been diminished due to altered biodistribution patterns. Previous reports have attributed altered biodistribution of IgGs in NSG mice to the lack of endogenous IgG, as well as interactions between FcγR present in myeloid cells in the spleen, liver, and bone [265, 266]. While in this study, we were able to still demonstrate fluorescence localization in the context of these deterrents, this is an important consideration for further investigation of this agent, especially in orthotopic context. To address this, a preloading dose of antibody could be delivered to occupy FcRn receptors and minimize alterations to biodistribution, or an antibody fragment that lacks the Fc region of the antibody could be utilized. Herein, our main priority was to address localization of our conjugate in the context of PDAC microenvironment, which we were able to confirm. Furthermore, analysis of one PDX tumor really only provides a snapshot of clinically replicative tumors. Assessing distribution and accretion of huAR9.6-IRDye800 across multiple PDX models with varying levels of MUC16 expression and differential microenvironments may help to strengthen the evidence for success of huAR9.6-IRDye800.

Overall, the results of this study demonstrated that huAR9.6-IRDye800 is specific for MUC16, and is a safe, non-toxic probe, and can effectively illuminate tumors in translational cancer models. Data presented here demonstrates compelling evidence of the efficacy of huAR9.6-IRDye800 and necessitates further investigation for clinical translation.

Chapter 4: Safety, Toxicity, and Long-Term Biodistribution of HuAR9.6-IRDye800

4.1 Introduction

The expansive pipeline of optical imaging agents in clinical development for solid tumors demonstrates significant scientific efforts to translate FGS to the clinic. 5-ALA, an

agent approved for imaging gliomas, has demonstrated both surgical utility and patient benefit from integration of this technology, mirrored by the success of ICG, and several targeted imaging agents in late phase clinical trials [170]. Since the majority of clinical trials for FGS are in Phase 1, there is a lack of data about patient benefit and the overall value and impact of FGS on surgical outcomes and survival. Phase 3 clinical trial data will be essential to provide a strong rationale for the necessity of widespread adoption of FGS in clinical practices [267]. However, there are significant hurdles towards approval of optical imaging agents that have made the progress of agents to the clinic slow. Thorough consideration of metrics of efficacy, extensive consideration of safety and toxicity profiles, and standardization of study design during preclinical investigation will aid in translation [171, 268]. Before consideration of clinical translation, the safety and toxicity of an agent requires significant evaluation. Concerns of toxicity can be attributed to the contrast agent used, or the targeting vehicle, since different targeting vehicles can have vastly different biodistribution profiles and circulation times.

We have developed a humanized antibody near-infrared conjugate, termed huAR9.6-IRDye800, that has shown efficacy in delineating pancreatic cancer intraoperatively through the use of FGS. The near infrared dye, IRDye800, employed in this conjugate has demonstrated a safe, non-toxic profile through extensive preclinical testing, and clinical trials [62, 210, 250, 269–271]. However, the antibody component of this conjugate, huAR9.6, is novel, and has not been investigated for safety or toxicity. Antibodies have been used frequently as a targeting moiety in FGS studies due to their high target affinity, and stability. However, antibodies can have long circulation times, exhibit off target binding to endogenous proteins, and have instances of hypersensitivity, infusion reactions, and potentially high levels of immunogenicity. Thus, critical evaluation of the safety and toxicity profile for this targeting moiety is paramount. Herein, we seek to demonstrate proof of concept data describing the safety, biodistribution, and toxicity

profile of huAR9.6-IRDye800, and lay the groundwork for further dose evaluation, and future two-species toxicity studies for clinical translation.

4.2 Methods and Materials

4.2.1 Antibody Conjugation

HuAR9.6 was conjugated to IRDye800 N-hydroxysuccinimide (NHS) ester (0.5 mg, LI-COR Biosciences, 929-70020; Lincoln, NE) according to the instructions of the manufacturer. Briefly, 100 µl of 1M potassium phosphate was added to each mg of antibody to raise the pH to 8.5. Dye was dissolved in 50 µl of Nanopure water, and added to 1 mg of antibody and incubated for 2 hours at room temperature. Addition of 0.12 mg of dye consistently resulted in ~1:1 dye:protein. Excess dye was removed by Zeba spin desalting columns (ThermoFisher Scientific, 89891). Antibody diluted 1:5 in 1:1 PBS:methanol was loaded into a 1 cm cuvette (Eppendorf, E0030106300; Hauppauge, NY). Conjugation ratios were determined spectrophotometrically with a Thermo Scientific Evolution 220 UV-visible spectrophotometer, and fluorescence was confirmed with a FluoroMax 4 spectrofluorometer (Horiba Scientific; Irvine, CA).

4.2.2 Biodistribution, Safety, and Toxicity

All animal work was performed under a protocol approved by the UNMC IACUC. 6-8 week old male and female CD-1 mice (Charles River, Crl:CD1(ICR)) were injected with 100 µl of saline control, 20 µg of 1:1 dye:protein huAR9.6-IRDye800 or 80µg of 1:1 dye:protein huAR9.6-IRDye800 via tail vein. Agent was allowed to circulate for 1, 14, or 28 days after injection. Mice were weighed weekly as an evaluation of toxicity for the the 28-day timepoint, and weighed every three days for the 14-day timepoint. At the randomly assigned timepoint, cardiac punctures were conducted, and necropsies were performed. Blood was collected in serum separator tubes, and serum was separated after samples were allowed to clot for 30 minutes. Serum was analyzed for blood

chemistry on the Abaxis Vetscan VS-2 chemistry analyzer. Resected organs were imaged on the LI-COR Pearl and quantified as previously described. Organs were fixed in 10% neutral buffered formalin for 24 hours, before paraffin embedding. Organs were stained with H&E and analyzed for signs of toxicity by a board-certified pathologist (G.A.T) who was blinded to the treatment groups.

4.2.3 Statistical Analysis

All statistical analyses were conducted using Graph Pad Prism software. A Two-way ANOVA, followed by Tukey's test for multiple comparisons was used to compare differences in mean fluorescent signal in resected organs for the biodistribution study. A One-way ANOVA followed by Tukey's test for multiple comparisons was used to compare blood chemistry values for each group. All values are reported as the mean ± standard deviation.

4.3 Results

4.3.1 Biodistribution

To assess the biodistribution of huAR9.6-IRDye800, male and female CD-1 mice were randomly assigned to a 24-hour, 14-day, or 28-day time point. 3 male and 3 female mice at each timepoint were injected with either saline (control) a low dose (20 μg) of huAR9.6-IRDye800, or a high dose (80 μg) of huAR9.6-IRDye800 via tail vein. Doses were selected based on human equivalent doses (calculated from body surface area) of ~5 mg and ~20 mg respectively [272]. These doses captured a range of similar antibody-based fluorescent agents used in early phase clinical trials [200, 262]. At the assigned time point after injection of the agent, blood was collected via cardiac puncture, mice were euthanized, and necropsies were conducted. Organs were imaged on the LI-COR Pearl, using the white and 800 nm channels. Mean fluorescent signal (mean NIR signal per pixel) was calculated for each organ. Representative images of necropsied organs

from each of group at 1,14, and 28 days post-injection are shown in **Figures 37, 39, and 41** respectively. Primary clearance and distribution were observed within the liver. At 1 day after injection, mean liver signal in both the low dose (0.0320 ± 0.0099) and high dose (0.1582 ± 0.0298) huAR9.6-IRDye800 groups was significantly higher ($p < 0.0001$) than the control group (0.0014 ±0.0004) as shown in **Figure 37D**. While the primary clearance route for unconjugated IRDye800 is renal, it is expected to see primary clearance through the liver with antibody conjugates, because the large size largely prohibits glomerular filtration. Male and female mice were also compared within groups to ascertain if biodistribution varied between sexes **(Figure 38)**. At 1 day post-injection, the biodistribution was largely consistent for all organs between male and female mice in all groups, with the exception of differences in kidney signal in the control saline group, and liver in the low dose group. No significant differences in biodistribution were observed in the high dose group **(Figure 38C)**. By day 14, signal in the liver decreased by >10 fold in both the high and low dose huAR9.6-IRDye800 groups, with mean liver signals of 0.0102 ± 0.0043 and 0.00339 ± 0.0009 respectively **(Figure 39)**. Signal in all organs was diminished at 14 days post-injection. The patterns of biodistribution were conserved between male and female mice for the majority of organs in all groups. Liver signal was significantly higher in male mice in the low dose group, but also in the saline group. Liver signal was not significantly different between male and female mice in the high dose group (**Figure 40, A-C**). By 28 days, little to no signal remained in any organs for either the high or low dose group, demonstrating that the conjugate had been cleared. While the mean quantified signal still showed significant differences in several organs at 28 days, all values were near zero **(Figure 41)**. Similar to the 14-day timepoint, only the liver signal was significantly different between the sexes for all groups, including the saline control. The pattern of biodistribution was conserved between male and females for all other organs **(Figure 42)**.

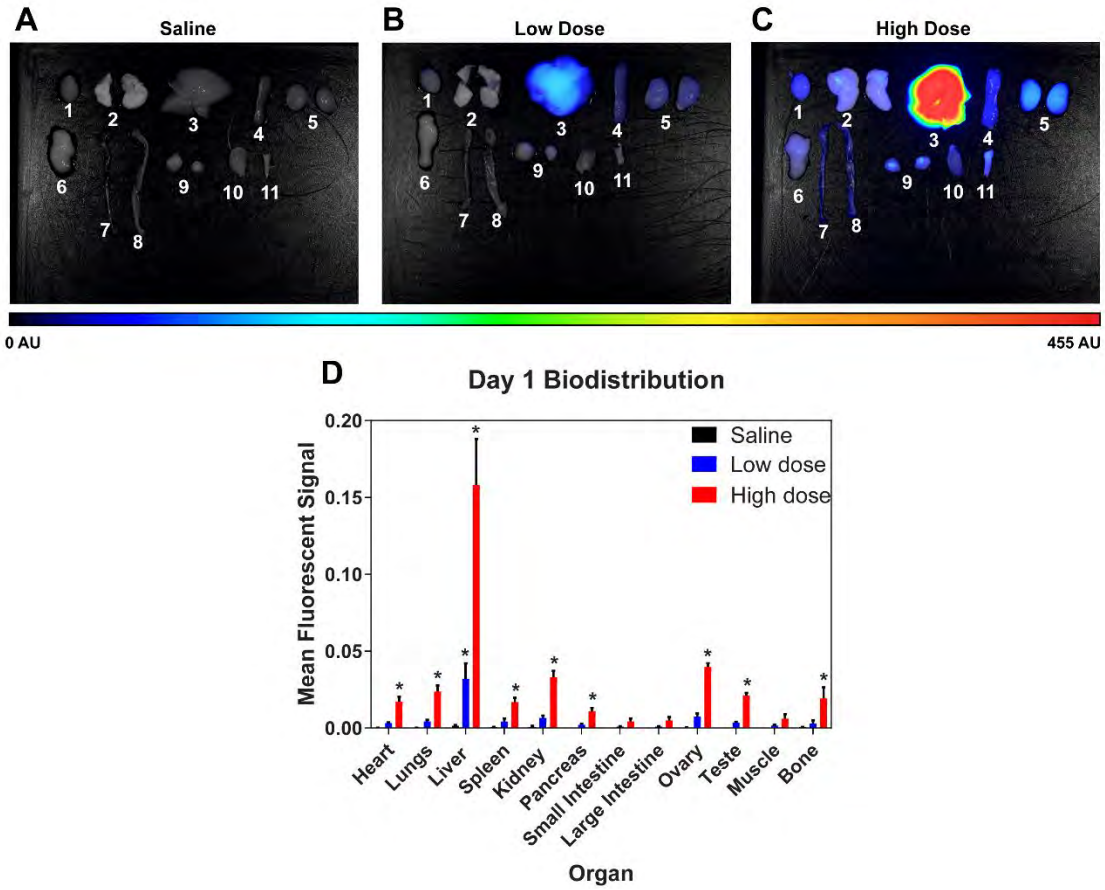

Figure 37: Day 1 biodistribution in **(A)** saline control, **(B)** low dose, **(C)** and high dose groups. Organs: 1 = heart, 2 = lungs, 3 = liver, 4 = spleen, 5 = kidneys, 6 = pancreas, 7 = small intestine, 8 = large intestine, 9 = ovaries, 10 = muscle, 11 = bone. (N = 6) **(D)** Day 1 quantified mean fluorescent signal from necropsied organs

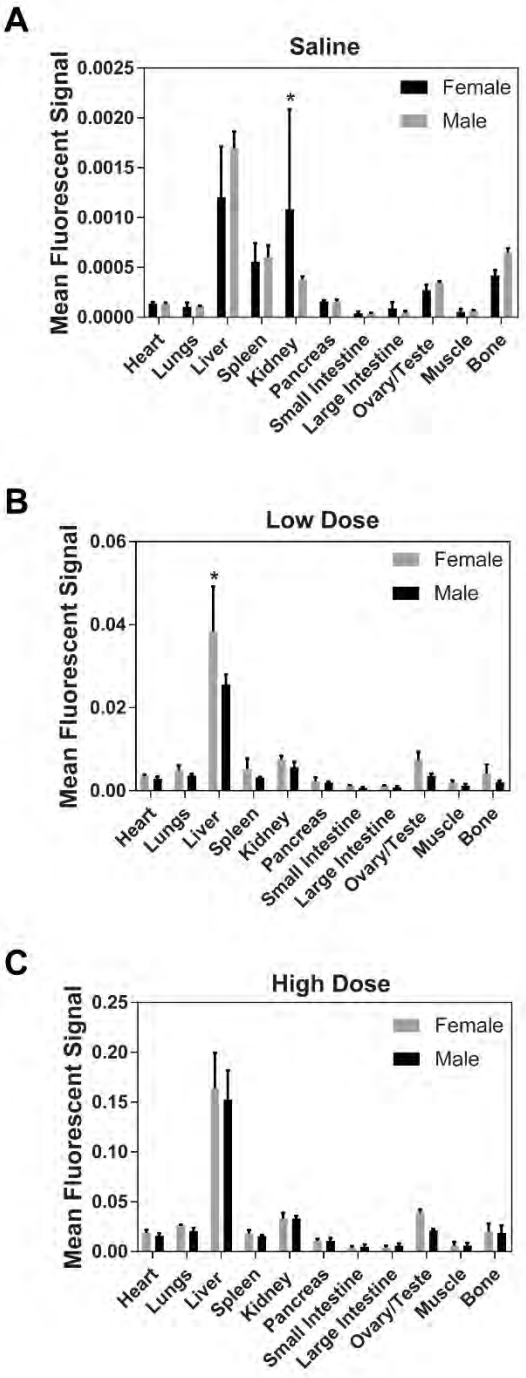

Figure 38: Day 1 comparisons of mean fluorescent signal in resected organs between male and female mice for **(A)** saline, **(B)** low dose, **(C)** and high dose groups.

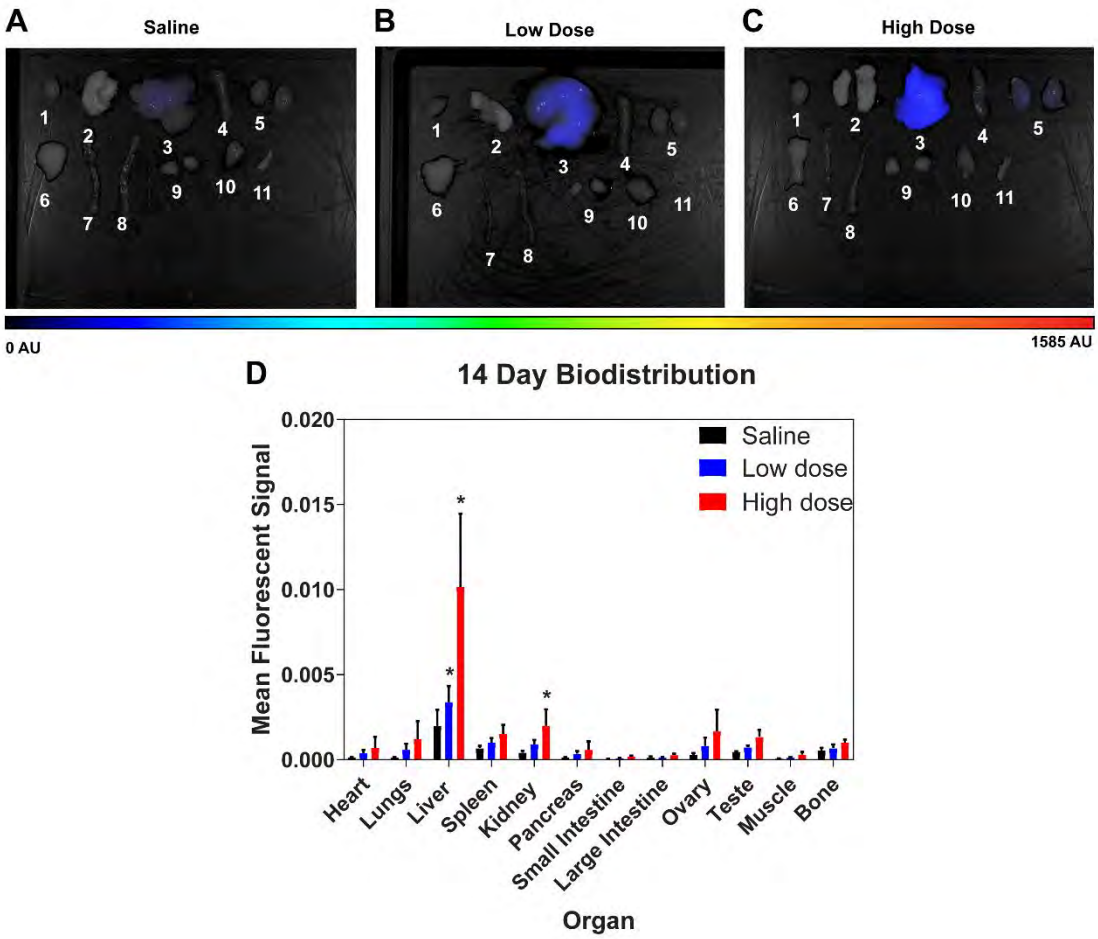

Figure 39: Day 14 biodistribution in **(A)** saline control, **(B)** low dose, **(C)** and high dose groups. Organs: 1 = heart, 2 = lungs, 3 = liver, 4 = spleen, 5 = kidneys, 6 = pancreas, 7 = small intestine, 8 = large intestine, 9 = ovaries, 10 = muscle, 11 = bone. (N=6) **(D)** Day 14 quantified mean fluorescent signal from necropsied organs.

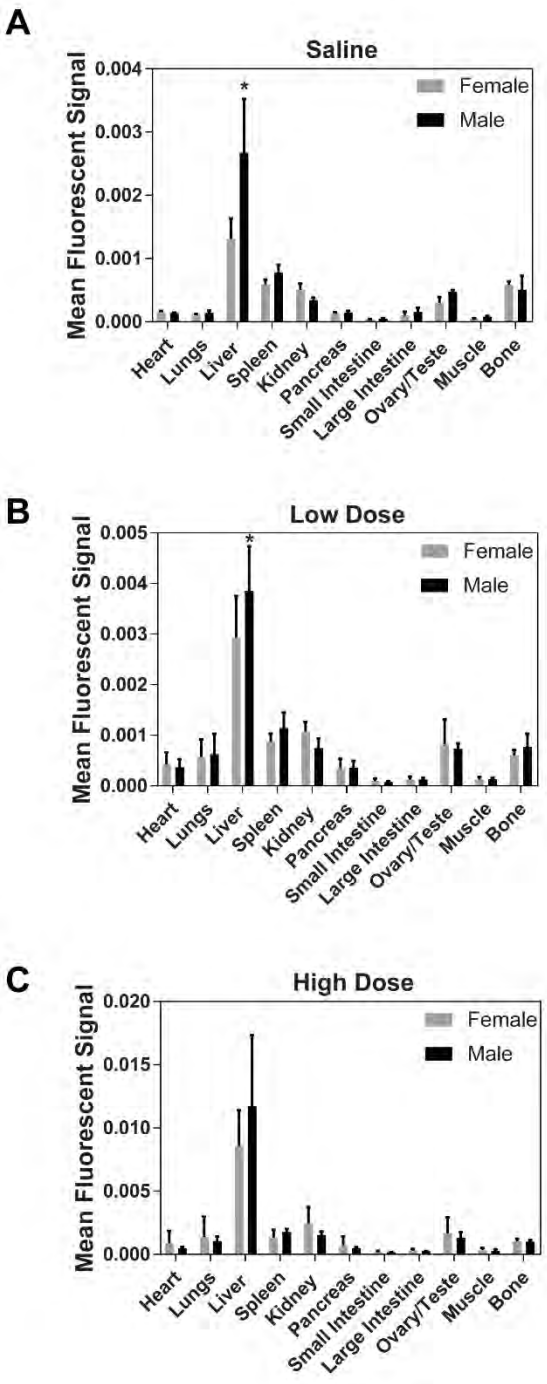

Figure 40: Day 14 comparisons of mean fluorescent signal in resected organs between male and female mice for **(A)** saline, **(B)** low dose, **(C)** and high dose groups.

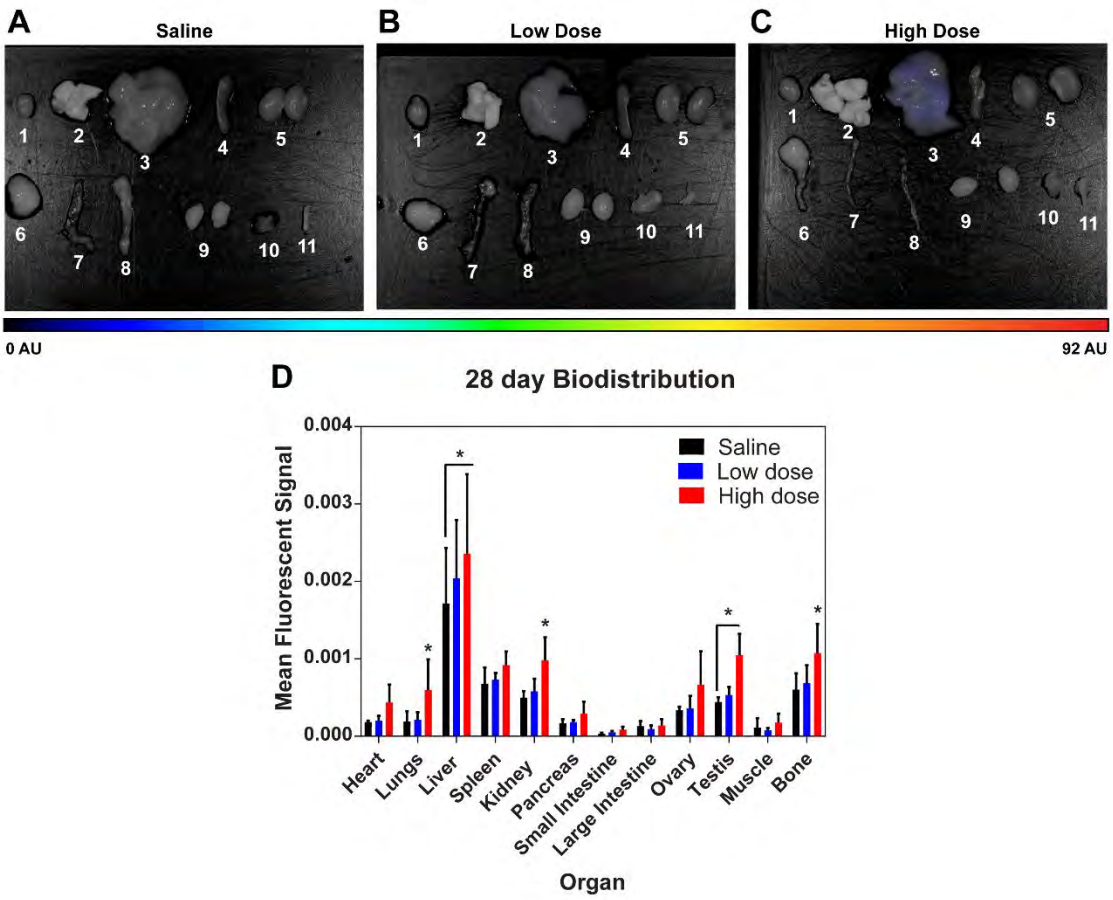

Figure 41: Day 28 biodistribution in **(A)** saline control, **(B)** low dose, **(C)** and high dose groups. Organs: 1 = heart, 2 = lungs, 3 = liver, 4 = spleen, 5 = kidneys, 6 = pancreas, 7 = small intestine, 8 = large intestine, 9 = testes, 10 = muscle, 11 = bone. (N=6 per group) **(D)** Day 28 quantified mean fluorescent signal from necropsied organs.

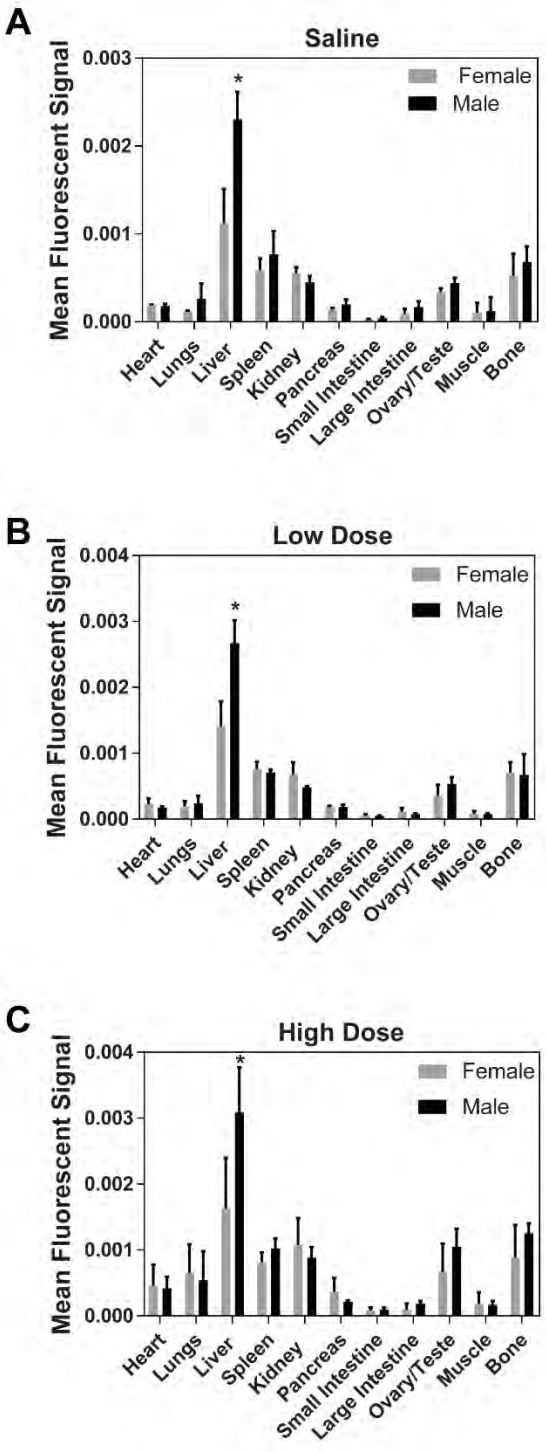

Figure 42: Day 28 comparisons of mean fluorescent signal in resected organs between male and female mice for **(A)** saline, **(B)** low dose, **(C)** and high dose groups.

4.3.2 Blood Chemistry Analysis

Serum isolated from blood samples collected at cardiac puncture were analyzed to obtain blood chemistry values. At one day post-injection, there were no significant differences in blood chemistry parameters between the saline control, low dose, and high dose huAR9.6-IRDye800 groups, as summarized in **Table 3**, and depicted in **Figures 43**. When female and male mice were analyzed separately the only significant differences between sexes were observed in total bilirubin (TBIL), and sodium (NA+) levels in the low dose groups. However, no differences were observed in the high dose groups between sexes. Variations in both sodium and total bilirubin are likely to be a result of hemolysis [273, 274]. All other blood chemistry parameters were consistent between male and female mice.

At the 14 days post-injection time point, there were no significant differences across groups for any blood chemistry values except alkaline phosphatase (ALP) **(Table 4, Figure 44)**. ALP was significantly lower in the low dose group, but no significant differences were observed in the high dose group. Comparisons between female and male mice showed that there were largely no differences between the sexes for most values. Total bilirubin (TBIL), and sodium (NA+) were significantly different between the sexes for the low dose male and female mice, but not for the high dose groups. All other blood chemistry parameters were consistent between male and female mice.

At 28 days post-injection, again the majority of the blood chemistry parameters analyzed were not significantly different across groups **(Table 5, Figure 45)**. Potassium (K+) was significantly lower in low and high dose huAR9.6-IRDye800 as compared to the saline control group, and Calcium (CA) was significantly higher in the high dose group compared to the low and saline groups. These differences in values are likely attributed to hemolysis that was observed in several samples, due to acquisition of samples through a needle by cardiac puncture [273, 274]. Male and female mice had no

significant differences in blood chemistry values, with the exception of total bilirubin (TBIL) which had significant differences for the high dose of huAR9.6-IRDye800. All other values were not significantly different between males and females at 28 days post-injection. The consistency in blood chemistry parameters for the saline control, low dose huAR9.6-IRDye800, and high dose huAR9.6-IRDye800 for all time points, supports the tolerability and safety of huAR9.6-IRDye800 as a fluorescent probe for FGS.

Table 3: Blood Chemistry Analysis from 1-Day Timepoint

Blood Chemistry	Saline	Low Dose	High Dose	Significance
ALB g/L	37.83 ± 2.14	36.88 ± 2.17	35.83 ± 2.64	ns
ALP U/L	81.00 ± 23.18	81.38 ± 14.85	73.33 ± 25.69	ns
AMY U/L	866.83 ± 80.55	874.00 ± 102.43	786.17 ± 44.66	ns
TBIL µmol/L	3.50 ± 1.05	4.13 ± 0.64	4.17 ± 0.75	ns
BUN mmol/L	8.67 ± 1.14	7.66 ± 0.94	6.35 ± 1.28	ns
CA+ mmol/L	2.28 ± 0.27	2.44 ± 0.21	2.60 ± 0.09	ns
PHOS mmol/L	2.56 ± 0.37	2.60 ± 0.30	2.28 ± 0.11	ns
GLU mmol/L	16.83 ± 3.97	14.23 ± 2.72	13.23 ± 2.37	ns
NA+ mmol/L	146.00 ± 2.68	147.38 ± 1.77	146.33 ± 1.21	ns
K+ mmol/L	5.50 ± 0.46	5.94 ± 1.48	5.12 ± 1.19	ns
TP g/L	47.17 ± 2.32	47.75 ± 1.75	47.33 ± 1.97	ns
GLOB g/L	9.33 ± 1.86	10.75 ± 1.83	11.83 ± 0.98	ns

Abbreviations: ALB = albumin, ALP = alkaline phosphatase, AMY = amylase, TBIL = total bilirubin, BUN = blood urea nitrogen, CA+ = calcium, PHOS = phosphorus, GLU = glucose, NA+ = sodium, K+ = potassium, TP = total protein, GLOB = globulin

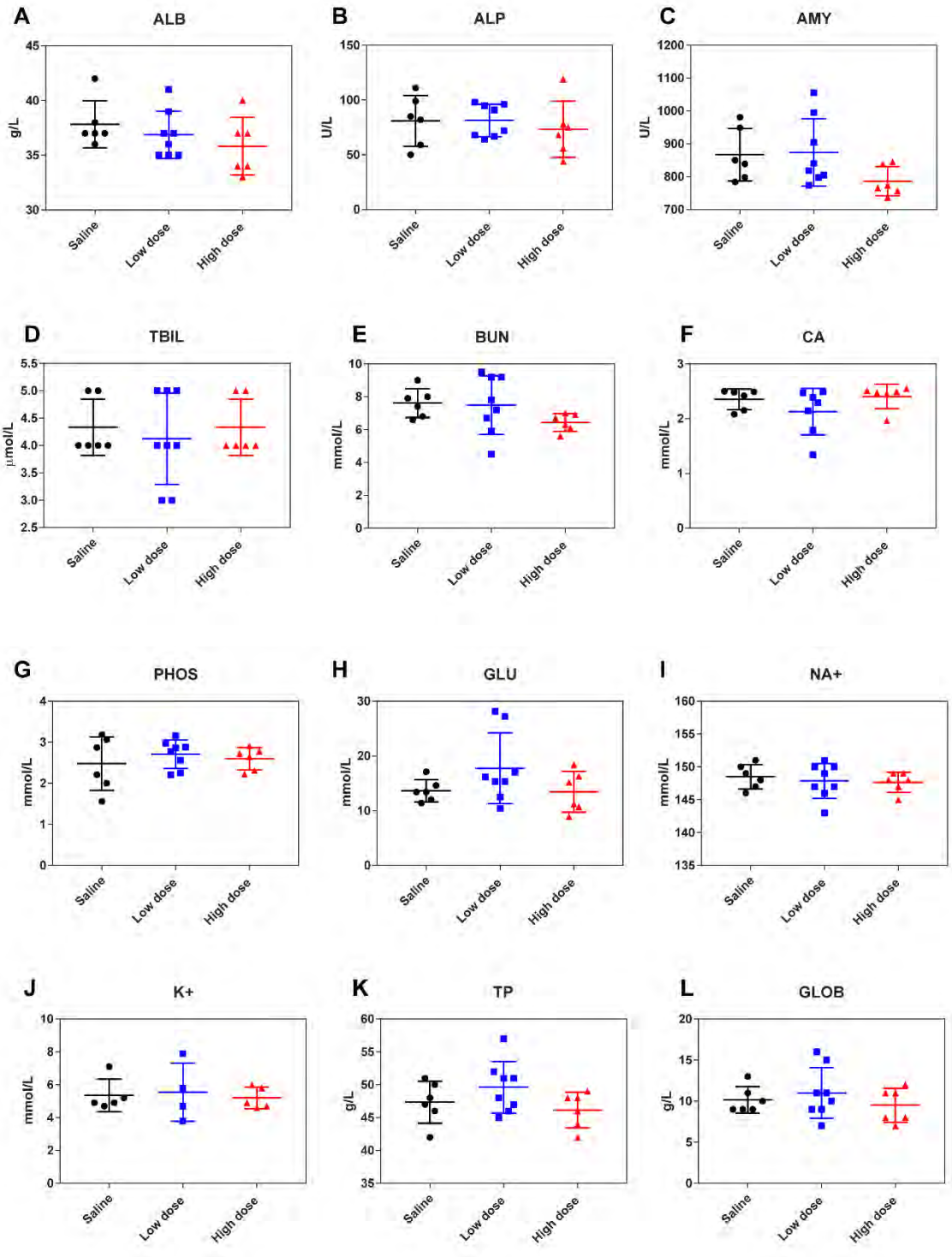

Figure 43: Blood chemistry values from 1 day after injection. **(A)** ALB = albumin **(B)** ALP = alkaline phosphatase **(C)** AMY = amylase **(D)** TBIL = total bilirubin **(E)** BUN = blood urea nitrogen **(F)** CA = calcium **(G)** PHOS = phosphorus, **(H)** GLU = glucose, **(I)** NA+ = sodium **(J)** K+ = potassium **(K)** TP = total protein **(L)** GLOB = globulin (N=6)

Table 4: Blood Chemistry Analysis from 14-Day Timepoint

Blood Chemistry	Saline	Low Dose	High Dose	Significance
ALB g/L	37.33 ± 3.50	38.50 ± 2.33	36.50 ± 2.66	ns
ALP U/L	105.17 ± 21.72	67.88 ± 14.52	98.50 ± 21.77	*
AMY U/L	957.50 ± 95.40	974.38 ± 148.22	873.00 ± 117.10	ns
TBIL µmol/L	4.33 ± 0.52	4.13 ± 0.83	4.33 ± 0.52	ns
BUN mmol/L	7.62 ± 0.88	7.50 ± 1.78	6.43 ± 0.54	ns
CA+ mmol/L	2.35 ± 0.19	2.13 ± 0.42	2.41 ± 0.22	ns
PHOS mmol/L	2.48 ± 0.65	2.71 ± 0.34	2.60 ± 0.27	ns
GLU mmol/L	13.65 ± 2.04	17.75 ± 6.47	13.45 ± 3.72	ns
NA+ mmol/L	148.50 ± 1.87	147.88 ± 2.64	147.67 ± 1.51	ns
K+ mmol/L	5.36 ± 0.99	5.55 ± 1.77	5.20 ± 0.65	ns
TP g/L	47.33 ± 3.20	49.63 ± 3.93	46.17 ± 2.71	ns
GLOB g/L	10.17 ± 1.60	11.00 ± 3.07	9.50 ± 2.07	ns

Abbreviations: ALB = albumin, ALP = alkaline phosphatase, AMY = amylase, TBIL = total bilirubin, BUN = blood urea nitrogen, CA+ = calcium, PHOS = phosphorus, GLU = glucose, NA+ = sodium, K+ = potassium, TP = total protein, GLOB = globulin (N =6)

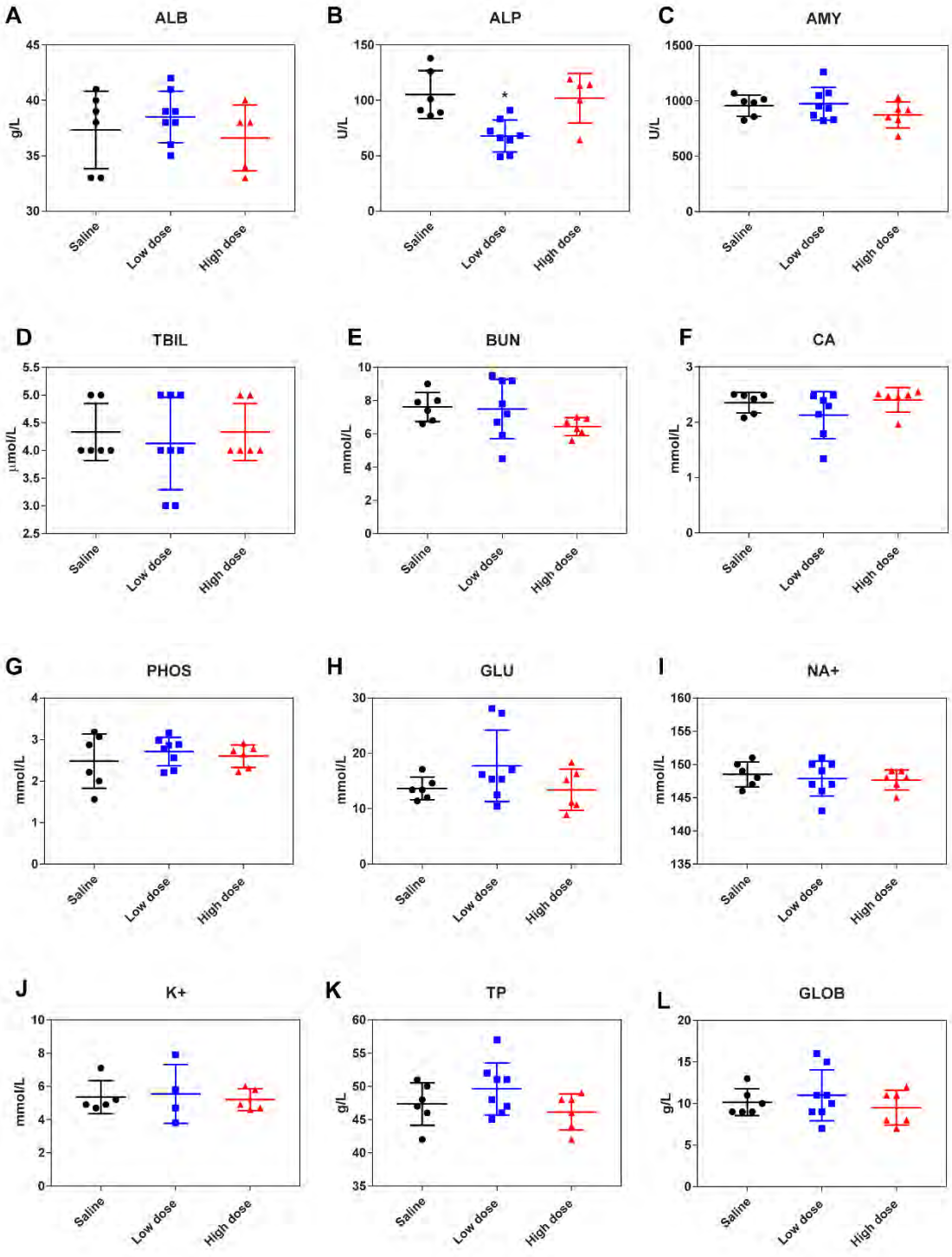

Figure 44: Blood chemistry values from 14 days after injection. **(A)** ALB = albumin **(B)** ALP = alkaline phosphatase **(C)** AMY = amylase **(D)** TBIL = total bilirubin **(E)** BUN = blood urea nitrogen **(F)** CA = calcium **(G)** PHOS = phosphorus, **(H)** GLU = glucose, **(I)** NA+ = sodium **(J)** K+ = potassium **(K)** TP = total protein **(L)** GLOB = globulin (N=6)

Table 5: Blood Chemistry Analysis from 28-Day Timepoint

Blood Chemistry	Saline	Low Dose	High Dose	Significance
ALB g/L	38.00 ± 3.03	37.71 ± 2.63	36.60 ± 3.51	ns
ALP U/L	69.67 ± 12.16	76.43 ± 24.13	77.80 ± 15.80	ns
AMY U/L	847.33 ± 118.28	889.57 ± 128.64	837.00 ± 71.11	ns
TBIL µmol/L	3.83 ± 0.41	4.43 ± 0.98	5.20 ± 1.10	ns
BUN mmol/L	7.65 ± 0.88	7.24 ± 1.16	6.76 ± 1.47	ns
CA+ mmol/L	2.34 ± 0.15	2.38 ± 0.12	2.60 ± 0.08	*
PHOS mmol/L	2.39 ± 0.34	2.65 ± 0.46	2.48 ± 0.39	ns
GLU mmol/L	16.20 ± 2.49	15.00 ± 3.35	14.36 ± 2.31	ns
NA+ mmol/L	145.33 ± 2.16	147.00 ± 2.08	147.20 ± 1.92	ns
K+ mmol/L	6.26 ± 0.26	5.47 ± 0.59	4.80 ± 0.48	*
TP g/L	47.00 ± 2.68	46.57 ± 3.36	46.00 ± 2.45	ns
GLOB g/L	9.00 ± 2.28	9.60 ± 2.41	9.80 ± 1.30	ns

Abbreviations: ALB = albumin, ALP = alkaline phosphatase, AMY = amylase, TBIL = total bilirubin, BUN = blood urea nitrogen, CA+ = calcium, PHOS = phosphorus, GLU = glucose, NA+ = sodium, K+ = potassium, TP = total protein, GLOB = globulin (N=6)

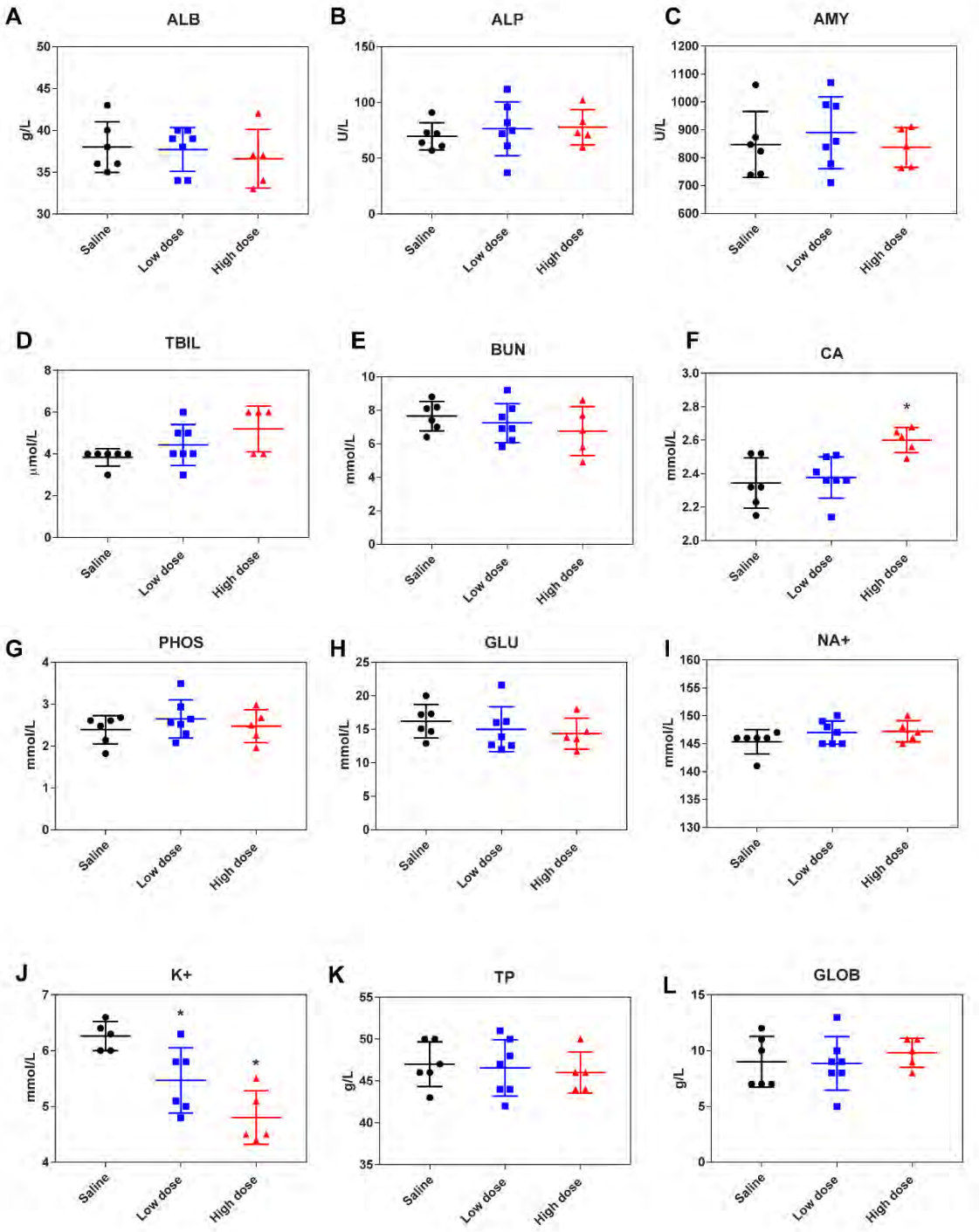

Figure 45: Blood chemistry values from 28 days after injection. **(A)** ALB = albumin **(B)** ALP = alkaline phosphatase **(C)** AMY = amylase **(D)** TBIL = total bilirubin **(E)** BUN = blood urea nitrogen **(F)** CA = calcium **(G)** PHOS = phosphorus, **(H)** GLU = glucose, **(I)** NA+ = sodium **(J)** K+ = potassium **(K)** TP = total protein **(L)** GLOB = globulin (N=6)

4.3.3 Toxicity and Organ Pathology

To monitor for signs of toxicity, animal weights were monitored for the 14-day and 28-day post-injection timepoints. No significant changes in weight were observed for male or female mice over the 14-day and 28-day time points, as depicted in **Figure 46A** and **Figure 46B** respectively, indicating that huAR9.6-IRDye800 was well tolerated. At the indicated timepoint of 24 hours, 14 days, or 28 days, organs resected at euthanasia were formalin-fixed and paraffin-embedded, sectioned, and stained with H&E. Slides were examined by a board-certified pathologist (G.A.T), who was blinded to treatment groups and study results, for any signs of toxicity. Results from the 1-day timepoint showed that no significant toxicity was observed in any group, as summarized in **Table 6**. Minimal and insignificant histological changes were observed in minor lobular inflammation in the liver, but this was also observed in the control saline group. Mild vacuolar changes and mild tubular dilation were observed in the kidneys of one subject in the saline group and high dose group respectively, but again changes were not classified as significant. At 14 days, no significant toxicity was observed in any group **(Table 7)**. Several mice had minimal and insignificant focal lobular inflammation in the liver consistent with observations 1-day post-injection, but this was also observed in the saline control group as well, and thus is not likely to be attributed to huAR9.6-IRDye800. At 28 days, results were consistent with earlier timepoints as shown in **Table 8**. There were several cases of minor focal lobular inflammation in the liver, but this was observed in all groups including the saline control. Several cases had minor patches of tubular dilation in kidneys. Histological changes observed at all three timepoints in the liver and kidneys were considered minimal and insignificant, and changes were consistent between the saline, low dose, and high dose groups, and are thus likely not attributed to the injection of huAR9.6-IRDye800. The absence of signs of toxicity in response to

huAR9.6 at 1 day, 14 days, and 28 days post-injection provides compelling preliminary evidence that huAR9.6-IRDye800 is a safe, non-toxic probe.

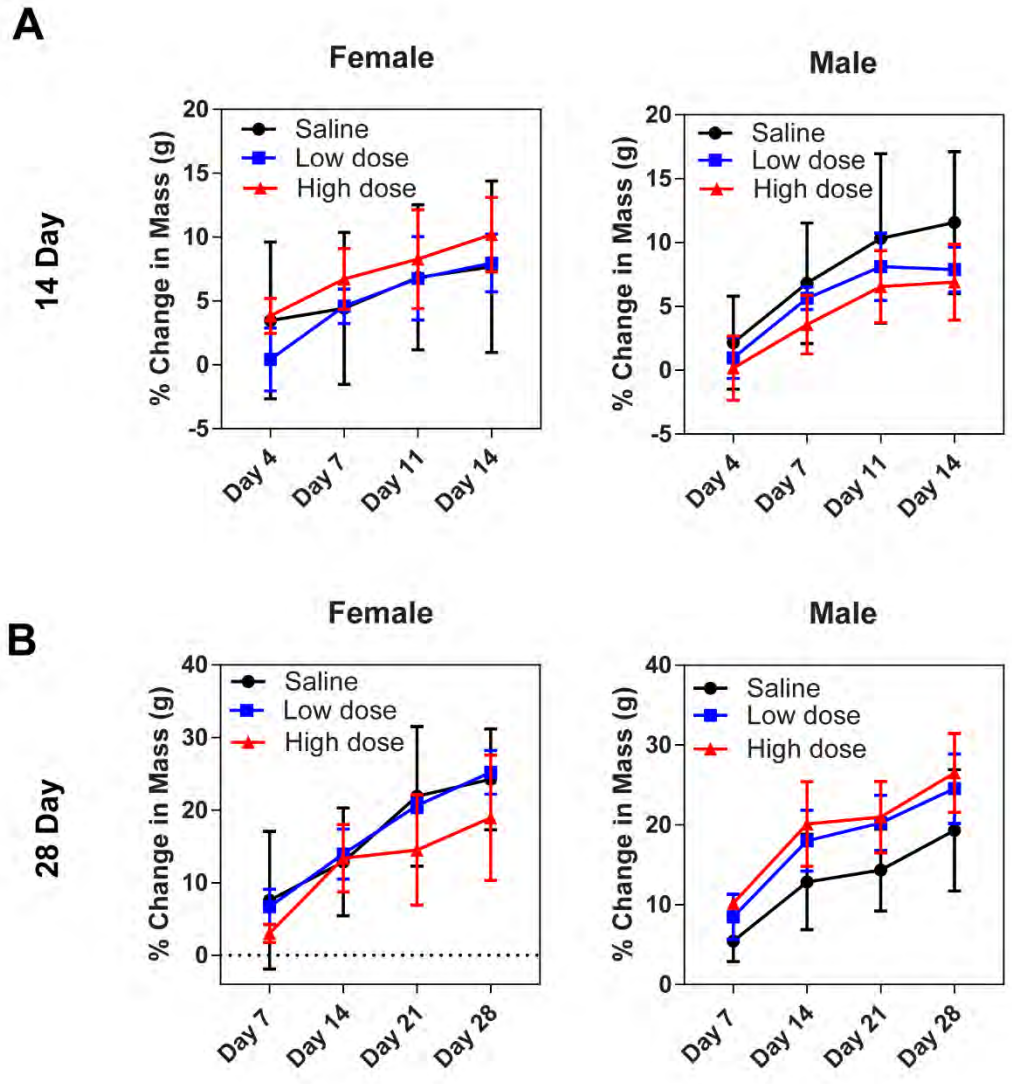

Figure 46: Change in mouse weights over time for **(A)** 14-day group and **(B)** 28-day group.

Table 6: Histological evaluation of key clearance organs necropsied 1-day post-injection.

		0 ***NO SIGNIFICANT HISTOLOGICAL CHANGES***	**1** ***MINIMAL HISTOLOGICAL CHANGES***	**2** ***MILD HISTOLOGICAL CHANGES***	**3** ***MODERATE HISTOLOGICAL CHANGES***	**4** ***SEVERE HISTOLOGICAL CHANGES***
CONTROL (SALINE)	Heart	100%				
	Lungs	100%				
	Spleen	100%				
	Kidney	83.3%	16.67%			
	Liver	83.3%	16.67%			
LOW DOSE	Heart	100%				
	Lungs	100%				
	Spleen	100%				
	Kidney	100%				
	Liver	100%				
HIGH DOSE	Heart	100%				
	Lungs	100%				
	Spleen	100%				
	Kidney	83.3%	16.67%			
	Liver	83.3%	16.67%			

Table 7: Histological evaluation of key clearance organs necropsied 14-days post-injection.

		0 ***NO SIGNIFICANT HISTOLOGICAL CHANGES***	**1** ***MINIMAL HISTOLOGICAL CHANGES***	**2** ***MILD HISTOLOGICAL CHANGES***	**3** ***MODERATE HISTOLOGICAL CHANGES***	**4** ***SEVERE HISTOLOGICAL CHANGES***
CONTROL (SALINE)	Heart	100%				
	Lungs	100%				
	Spleen	100%				
	Kidney	83.3%	16.67%			
	Liver	66.7%	33.3%			
LOW DOSE	Heart	100%				
	Lungs	100%				
	Spleen	100%				
	Kidney	100%				
	Liver	62.5%	37.5%			
HIGH DOSE	Heart	100%				
	Lungs	100%				
	Spleen	100%				
	Kidney	100%				
	Liver	83.3%	16.67%			

Table 8: Histological evaluation of key clearance organs necropsied 28-days post-injection.

		0 ***NO SIGNIFICANT HISTOLOGICAL CHANGES***	**1** ***MINIMAL HISTOLOGICAL CHANGES***	**2** ***MILD HISTOLOGICAL CHANGES***	**3** ***MODERATE HISTOLOGICAL CHANGES***	**4** ***SEVERE HISTOLOGICAL CHANGES***
CONTROL (SALINE)	Heart	100%				
	Lungs	100%				
	Spleen	100%				
	Kidney	100%				
	Liver	50%	50%			
LOW DOSE	Heart	100%				
	Lungs	100%				
	Spleen	100%				
	Kidney	87.5%	12.5%			
	Liver	87.5%	12.5%			
HIGH DOSE	Heart	100%				
	Lungs	100%				
	Spleen	100%				
	Kidney	50%	50%			
	Liver	66.7%	33.3%			

4.4 Discussion

This study demonstrated compelling evidence of a non-toxic safety profile for huAR9.6-IRDye800, and provides data to support clinical translation efforts for this fluorescent conjugate. IRDye800 alone has been well documented for its safety across vigorous preclinical and clinical studies. However, humanized AR9.6 is a new molecular entity, and as with any combination product, huAR9.6-IRDye800 must undergo rigorous evaluation before clinical translation. Among these qualifications for further investigation are in-depth analysis of the safety, toxicity, and biodistribution profiles. To that end, this study was conducted to lay the groundwork and provide preliminary evidence of the safety profile of huAR9.6-IRDye800 to support further investigation and translation.

Since the ultimate goal of this study was to produce preliminary evidence, doses for safety evaluation were chosen to directly reflect a range of doses used for similar agents in clinical trials and several preclinical studies [200, 262]. However, moving forward, a multiple of a human equivalent dose will be assessed, either 10-fold or 100-fold greater than the anticipated human dose. In this study, doses were calculated based on body surface area from human equivalent doses of ~5 and ~20 mg, resulting in a low dose of 20 μg and a high dose of 80 μg in a CD-1 mouse model [272, 275]. Evaluation of this agent was conducted at three timepoints: 1 day, 14 days, and 28 days post-injection. These timepoints were chosen to evaluate the acute effects of huAR9.6-IRDye800 (1 day), provide initial information for the 14 day No-observed-effect-level (14 days), and elucidate long-term biodistribution (28 days), consistent with FDA nonclinical toxicity study recommendations [276]. Results from biodistribution studies highlighted primary clearance of the agent through the liver at 1 day post-injection, which was consistent with expected clearance patterns for an IgG. By 28 days, antibody conjugate was largely cleared. It is important to note that while preliminary evidence has demonstrated that AR9.6 binds to murine Muc16, further evidence is needed to support

this, and to determine if there are differences in binding human as compared to murine MUC16. This is an important consideration, because interaction with native MUC16 could impact biodistribution, as could differential expression of MUC16 in mice and humans [277]. Results from blood chemistry analysis showed there were minimal significant differences between the saline, low dose, and high dose groups. However, future studies need to increase sample size to allow for more complete independent analysis of male and female groups. Blood collection via cardiac puncture can lead to variability in many blood chemistry parameters due to hemolysis from collection methods, which was observed in several samples in this study, and is an inherent limitation of this analysis method. Increasing sample size may assist in differentiating changes in blood chemistry attributed to hemolysis. Results from the toxicity study provided strong support for the safety of huAR9.6-IRDye800, evidenced by the lack of significant histological changes in organ pathology. However, this parameter should also be investigated at higher dosing ranges and include a wider array of organs for analysis in future studies.

IRDye800 has undergone extensive analysis, and demonstrated a safe, non-toxic profile. This NIR dye is currently used in over 30 clinical trials, none of which have been withdrawn due to safety issues [278]. The majority of patients who receive antibody conjugates for FGS do not experience any serious adverse effects, regardless of the parent antibody used. However, the majority of antibodies currently under investigation for FGS repurpose an FDA-approved antibody as a targeting moiety. huAR9.6 will likely face additional regulatory hurdles because this is not yet an approved or widely adopted antibody. This further emphasizes the critical importance of thorough safety and toxicity evaluation. Overall, the data herein establishes preliminary evidence that huAR9.6-IRDye800 is a safe and non-toxic fluorescent conjugate, providing justification for further extensive safety evaluation in the pursuit of clinical translation of this agent.

Chapter 5: Conclusions and Future Perspectives

5.1 Conclusions

Surgery remains the cornerstone of treatment for most solid tumors, and is integrated across all settings of care, from preventative and diagnostic, to palliative, reconstructive, and curative treatment [279]. Because of the essential role of surgical resections in cancer care, ensuring disease eradication, or complete resections, in which both gross and microscopic disease are removed, is critical [280]. Positive surgical margins, or incomplete resections, are associated with increased recurrence rates, lower survival, increased rates of re-resection, and thus increased costs, morbidity, and quality of life [281]. Pancreatic cancer surgeries are extremely complex resections, complicated by infiltrating disease, inflammation, dense stroma, and frequently undetected lesions. Surgical resections for this disease are plagued by high rates of positive surgical margins [282]. Thus, there is a need for methods to improve intraoperative detection to reduce the frequency of incomplete resections, and improve survival rates and patient outcomes [283]. FGS has demonstrated significant potential across preclinical studies, as well as early and late phase clinical trials for improving the detection of many solid tumor types. Several early phase clinical trials have results that demonstrate initial success and feasibility for FGS of pancreatic cancer [2, 3, 200]. However, the targets studied for imaging probes in PDAC are limited. There remains a need for extensive research to develop additional imaging candidates that reflect the heterogeneity of the disease, and advance current imaging agents to later phase trials, to support the integration of FGS as a mainstay tool for surgical resection in pancreatic cancer.

This body of work focused on the development of a novel probe for FGS of pancreatic cancer. MUCIN16, also known as MUC16, or CA125, was chosen as a target for the development of a novel probe because it is highly overexpressed in pancreatic cancer, it is highly expressed in metastatic lesions, can be found in precursor lesions

(PANIN lesions), is expressed in many other cancer types, and had not yet been investigated for FGS in pancreatic cancer. The specifics of the probe design were selected to optimize and accelerate integration into the clinical setting. An antibody was selected as the targeting moiety to mirror the success of other targeted agents for pancreatic cancer. IRDye800CW NHS Ester was selected as the fluorophore because of the ease of conjugation, overall brightness, compelling safety profile, and relevance in clinical trials. This MUC16-targeted probe was termed AR9.6-IRDye800. Initial investigation of this probe described in Chapter 2 utilized a murine antibody that targeted human MUC16. These data showed that this probe bound MUC16 *in vitro* [190]. Dynamic contrast enhancement studies in subcutaneous mouse models showed that AR9.6-IRDye800 had significantly higher tumor to background ratios as compared to a non-specific IgG control from 48 hours through 144 hours after injection. *In vivo* studies demonstrated the efficacy of this probe in highlighting pancreatic cancer intraoperatively in an orthotopic model, with significantly higher contrast than the non-specific control. Additionally, these data showed that AR9.6-IRDye800 had the potential to identify metastatic lesions. Specific fluorescence localization was observed microscopically in primary tumors and metastatic lesions. Tumor to background ratios acquired during FGS in this study met preclinical recommendations of >3.0 for novel imaging probes, deeming the probe appropriate for further study [211]. Overall results from this initial study demonstrated strong potential for AR9.6-IRDye800 as an imaging agent for FGS of PDAC.

To further refine and investigate the translational potential of this probe, a humanized variant was developed using CDR grafting, as discussed in Chapters 3 and 4. This probe, termed huAR9.6-IRDye800, was synthesized using identical methodology as the first generation probe, but addressed the risk of immunogenicity that a murine antibody posed. The data, shown in previous chapters, demonstrated that the

humanized antibody bound with similar affinity as the murine variant used in earlier studies. Conjugation at varying dye to protein ratios did not impact binding. An optimal dye:protein ratio of 1:1 was selected to minimize the impact of conjugation of biodistribution, while allowing for consistent detection on a variety of imaging systems and maintaining continuity with current clinical trials. Dynamic contrast enhancement studies were conducted in three different subcutaneous tumor models, and demonstrated that in MUC16-positive tumors, huAR9.6-IRDye800 showed strong tumor contrast from 1-9 days after injection.

To further lay the groundwork for clinical translation, biodistribution, safety and toxicity of huAR9.6-IRDye800 were evaluated. Acute (1 day), 14 day, and long-term (28 day) timepoints were selected, and a saline control, low dose (20 μg of huAR9.6-IRDye800) and high dose (80 μg of huAR9.6-IRDye800) were compared. Organ pathology showed no significant signs of toxicity in any of the groups. Biodistribution studies demonstrated that signal was cleared by 28 days, and that clearance patterns were consistent, with primary clearance occurring in the liver for the antibody conjugate. Blood chemistry was analyzed and minimal differences were observed between groups. No significant changes in weight were observed in mice for the 14- and 28-day timepoints, providing further evidence that huAR9.6-IRDye800 was non-toxic and safe.

While the cell-line based subcutaneous and orthotopic models investigated in the early phases of this projected demonstrated initial efficacy of the AR9.6 probes, these models had limited capacity to represent the heterogeneity and complexity of pancreatic cancer. Thus, efficacy studies were completed using patient-derived xenograft models. Models were initially screened for expression of MUC16. Image-guided surgery conducted in this tumor model could more accurately recapitulate the tumor microenvironment that complicates pancreatic cancer resections. Overall, this body of work demonstrated the strong potential of the MUC16-targeted imaging probe, huAR9.6-

IRDye800 as a novel agent for FGS of pancreatic cancer. This work has also made a strong case for targeting MUC16 as a biomarker and has established the foundational data necessary for clinical translation. Nevertheless, there remains significant research needed to move this agent toward clinical trials. Furthermore, this body of work has sparked additional preclinical research questions that require investigation in the future [284].

5.2 Future Perspectives

5.2.1 Large Animal Models

Mouse models are an essential tool for cancer research and drug development, but these models have many limitations that need to be recognized as well, including their inability to reliably inform the efficacy, safety, and toxicity of drugs to treat cancer [285]. Porcine models present many advantages because of their comparable size, anatomy, genetics, and pathology (among many other factors) to humans. Using an induction method termed the Oncopig Cancer Model (OCM), a preliminary porcine PDAC model has been developed [284, 286]. This model poses many potential advantages for assessment of the efficacy of an imaging agent because it more closely recapitulates human PDAC. Furthermore, one of the major benefits of this large animal model is that it allows for investigation of diagnostic and interventional modalities, such as surgery, which are limited in rodent models because of size restrictions. Because FGS investigates a surgical intervention modality, the relevant size and anatomical similarities of Oncopigs to human disease may further improve preclinical investigation of FGS and resulting efficacy data as compared to much smaller mouse models. To that end, our lab has garnered an interest in collaborating with the lab of Dr. Mark Carlson (UNMC Department of Surgery, VA Nebraska-Western Iowa Health Care System) to investigate utilizing his porcine PDAC model for FGS with huAR9.6-IRDye800. Future studies will investigate the utility of huAR9.6-IRDye800 for detecting PDAC in a porcine

model. Using this model will better elucidate intraoperative tumor contrast with the agent, relative background noise, and efficacy for detecting primary tumor and other lesions in a context replicative of patient surgery. Furthermore, pathology can be analyzed to assess tumor heterogeneity and pathology of disease to allow for comparison to human tumors. Expression of MUC16 can be assessed within the tumor, and serum samples can be collected to look for the presence of circulating antigen. These studies will incorporate both open air imaging systems (such as the Curadel and Fluobeam), as well as laparoscopic imaging systems like the DaVinci surgical system.

5.2.2 Incorporation of Paired Clinical Imaging Systems and Standardized Imaging Methodology

A major consideration for FGS agents in clinical trials is the selection and incorporation of clinically relevant imaging devices. Fluorescent probes can either be paired with a specific imaging device, or imaging devices can be repurposed to be used with a variety of different imaging agents. Each of these strategies has caveats and considerations. Pairing a probe with a specific device can slow down regulatory approval and cause significant delays in clinical progress. However, repurposing an existing imaging device may not provide the optimal imaging parameters for the novel agent [60, 287]. Several different imaging devices were used throughout this body of work, including the Curadel, the Fluobeam, the LI-COR Pearl, and the Spectropen. The Fluobeam imaging system has an FDA-approved imaging device, and the Curadel imaging system has been used in several clinical trials. However, to allow for consistency across trials, it is also necessary to compare the signal, contrast, and sensitivity achieved in multiple clinical systems. PDAC clinical trials that have results, to date, have used the SPY-PHI (Novadaq/Stryker), PINPOINT (Novadq/Stryker), Explorer Air (SurgVision), Artemis, and Spectrum (Quest Medical Imaging) imaging systems for intraoperative imaging. All of these imaging modalities except for the Explorer Air are

currently FDA approved for imaging [170]. Thus, for future development of huAR9.6-IRDye800, it would be beneficial to incorporate these imaging systems. Because imaging systems have variable detection limitations and operational characteristics, incorporating the specific imaging modalities employed in current clinical trials would allow for direct comparison of contrast and noise data to current clinical results. Furthermore, PDAC resections may incorporate laparoscopic or open-air imaging systems, which differ widely in terms of imaging results and data. Future studies with huAR9.6-IRDye800 need to incorporate a wider variety of imaging systems that reflect clinically used systems to provide additional data on imaging efficacy and to improve standardization of data. Investigating additional devices will allow for optimization of device pairing for clinical trials.

In conjunction with the consideration of imaging modalities, conducting studies with a standardized imaging methodology, consistent with recent literature reports, may also improve the transition from preclinical to clinical studies [288, 289]. One of the major areas of variability in FGS is the lack of a standardized imaging methodology. To assist in accelerating clinical translation, it is paramount that FGS can not only seamlessly integrate into the clinical workflow, but also demonstrate a clinical benefit. Adoption of a standard and clear workflow for FGS will help to minimize variability between studies and improve the data collected, as well as strengthen the case for the clinical benefit of FGS. Thus, simulating this same workflow in preclinical studies is an important area of investigation for future studies. Some reports have suggested that incorporating back table imaging in closed-field imaging devices (such as the LI-COR Pearl) and increasing reliance on pathology may improve macroscopic and microscopic analysis of imaging agents [196, 252, 254]. This concept may be of greater importance for probes that target a specific biomarker, to confirm co-localization and assess intratumoral biodistribution. However, added clinical complexity and demands outside of the standard surgical

workflow should be considered as well. Nonetheless, future studies will be conducted to establish a workflow for AR9.6-IRDye800. An outline of the proposed clinical workflow is shown in **Figure 47**. The proposed workflow involves first utilizing FGS to survey the surgical field for the primary tumor, and also looking for metastatic lesions. After resection, FGS should be used for assessing margins and looking for any residual disease. The use of a closed-field imaging device after resection of the tumors may improve standardization of imaging, to remove variability of working distance and ambient light. Additions to the workflow may include bread loaf imaging, and microscopic imaging, particularly with a biomarker based-probe such as AR9.6-IRDye800. Information collected from microscopic, or 'tumor mapping' stages of the workflow provide information about probe localization, heterogeneity and targeting, that may improve or alter probe development, which is why it is necessary to analyze these factors during the preclinical workflow optimization [255, 290]. However, this may not be amenable or necessary as part of the final clinical workflow. Data collected should report on the sensitivity, specificity, negative predictive value, and positive predictive values. Standardizing expected imaging outcomes and data across multiple imaging devices, and optimizing a clinical workflow in preclinical studies will help ease the transition of imaging operations to the surgical suite during clinical trials. Design of these studies should involve clinical partners, including surgical oncologists and pathologists to assist in designing a study that minimizes disruption to clinical workflow while maximizing the data that can be collected and the outcomes from using FGS.

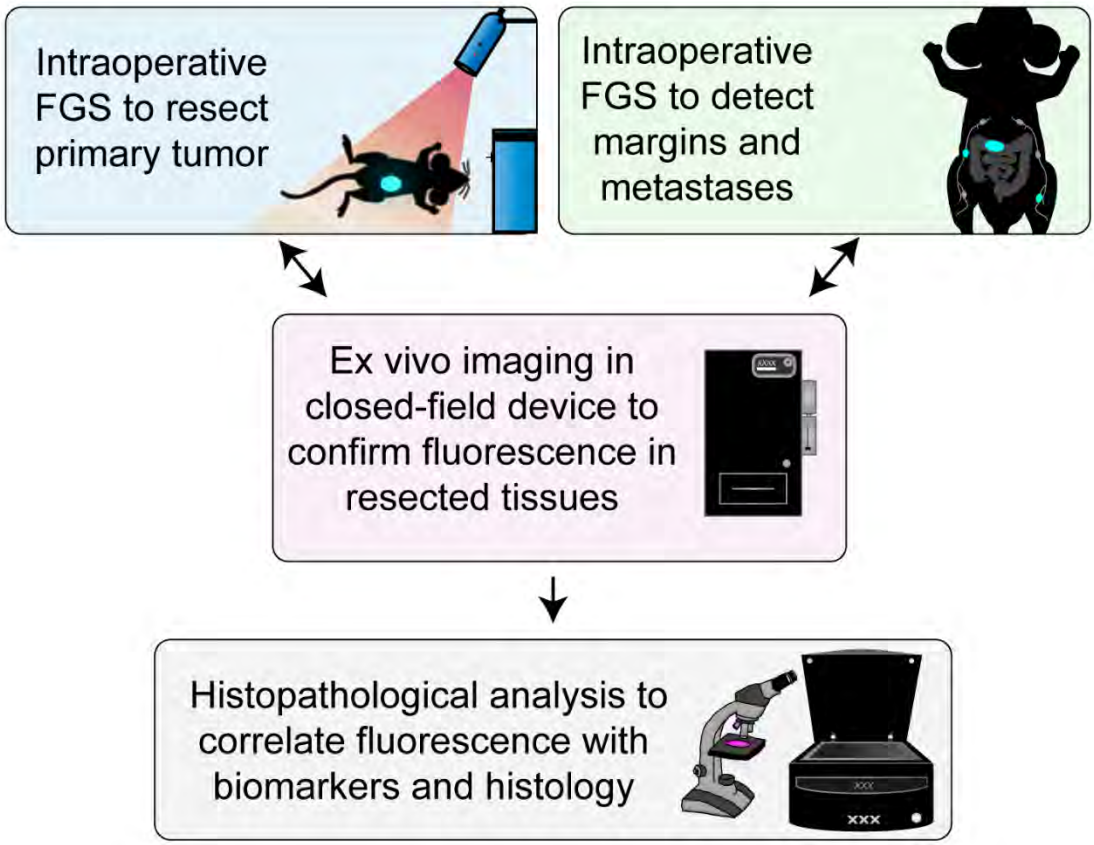

Figure 47: Proposed workflow for future development of huAR9.6-IRDye800

5.2.3 Clinical Translation

This body of work presents fundamental evidence of AR9.6-IRDye800 as a potential probe for FGS and supports further clinical development. Contextualizing this project in the broader framework of pharmaceutical drug development highlights the preliminary success of an appropriate and relevant target, efficacy in targeting tumors, with low background signal, and promising safety and toxicity profile [291, 292]. However, there are many additional studies that need to be conducted to assist in the clinical translation of huAR9.6-IRDye800. These studies include a two species toxicity and safety study (both rodent and non-rodent) in which a dose, typically a multiple of the projected clinical dose should be investigated to establish a wide safety margin. Antibody product needs to be scaled up in production and produced under good lab practice conditions. Pharmacokinetics and pharmacodynamics need to be evaluated, and the maximum tolerated dose needs to be established. Requirements for these studies are extensive, and will not be described at length herein, but have been summarized by Tummers, W. et al as shown in **Table 9**. Future work should focus on accomplishing these major studies needed to compile an Investigational New Drug application to support clinical translation of huAR9.6-IRDye800.

Table 9: Nonclinical studies needed for optical imaging agents. Adapted with permission from [171], Copyright © 2017, American Association for Cancer Research.

Study	Explanation
Proof-of-concept	Studies showing proof-of-concept of new molecular entity
Safety pharmacology	To measure functional indices of potential toxicity. The aim of the safety pharmacology studies should be to reveal any functional effects on major physiologic systems.
Pharmacokinetics and toxicokinetics	Single and multiple dose pharmacokinetics, toxicokinetics, and tissue distribution studies. Information on absorption, disposition, and clearance in relevant animal models should be collected.
Expanded single dose toxicity study (can be combined with repeat dose toxicity study)	Single dose studies should generate useful data to describe the relationship of dose to systemic and/or local toxicity. Repeated dose toxicity must be done when there is a chance for a secondary dose.
Special toxicology	e.g., phototoxicity, route irritancy, blood compatibility.
In vitro genotoxicity study	The use of standard genotoxicity studies for assessing the genotoxic potential of biotechnology-derived pharmaceuticals is not considered appropriate.

5.2.4 Addressing Neoadjuvant Therapy and Antigenic Shift

While neoadjuvant therapy is becoming increasingly incorporated for the treatment of pancreatic cancer, this treatment strategy is still in its infancy. Little information exists about the impact of neoadjuvant therapy on critical tumor biomarkers. Antigenic shift, or change in antigen expression as a result of chemotherapy, has been reported preliminarily in other cancer types, but little information exists in pancreatic cancer [198, 293, 294]. This is an important consideration for biomarker-based probes for FGS, and for therapeutic development in general. Because of the increasing prevalence of neoadjuvant therapy, it is necessary to fully understand the changes that occur in tumor biomarker expression, as this would guide the choice of adjuvant therapies, and of relevance herein, the choice of imaging agent. Furthermore, this question is further complicated by the involvement of serum-based biomarkers. MUC16, in addition to CA-19-9 and CEA, can all be cleaved and circulate in the bloodstream. Changes in serum levels of these antigens may be indicative of successful treatment, but the relationship between changes in serum levels of a protein and expression of the protein in the tumor needs to be investigated. Thus, studies are needed to evaluate the expression of MUC16 in patients treated with neoadjuvant therapy, to characterize changes in MUC16 expression. Furthermore, analyzing matched serum samples to resected patient tissues may provide critical information about the relationship between serum expression of a biomarker and tumor expression following neoadjuvant therapy. This study will help to develop criteria for which patients would benefit from MUC16-targeted imaging prior to or following therapy.

5.2.5 Antibody Cocktail

One of the common criticisms of biomarker-based probes is the heterogeneity of biomarker expression. Differential expression of biomarkers in tumors may result in heterogenous targeting, and subsequent contrast during imaging. A patient may present

with low levels of a biomarker or may not have a biomarker present at all. In the absence of a surgical biopsy to profile the tumor before surgery in order to better understand biomarker expression, using a cocktail of antibodies that target different biomarkers frequently present in tumors may improve imaging and reduce heterogenous distribution of contrast agents within the tumor [198, 200, 295, 296]. To this end, future studies should investigate the impact of using huAR9.6-IRDye800 in combination with other probes currently under investigation in clinical trials, such as antibody probes targeting VEGF-A, CEA, and EGFR. While there are likely regulatory challenges to this strategy, these studies are necessary to evaluate if more homogenous binding improves intraoperative contrast and detection capabilities.

5.2.6 Reducing off-target fluorescence

There are additional strategies that should be investigated to improve targeting of huAR9.6-IRDye800 to tumors. While MUC16 is not ubiquitously expressed throughout the body, it is expressed in the respiratory tract, cornea, and female reproductive tissues [202]. Endogenous expression in off-target organs may sequester circulating fluorescently labeled antibody. This off-target binding may reduce overall antibody availability, increase background signal, and reduce tumor-specific contrast. Studies with cetuximab-IRDye800, an EGFR targeted fluorescent probe, have demonstrated the utility of delivery of an unlabeled dose of antibody before injection of the contrast agent. The ubiquitous expression of EGFR, and particularly its high expression in skin and liver, have raised issues for imaging. However, clinical trials have been conducted that suggest that administration of a “preload” unlabeled dose of the antibody assisted in saturating EGFR in normal tissues, thereby improving tumor-specific uptake [110, 297]. This strategy has not yet been broadly investigated in clinical trials. While MUC16 is not as broadly expressed as EGFR, this strategy may also be useful to saturate cleaved MUC16 in patients with high serum levels of MUC16, and thus reduce levels of the

fluorescent conjugate circulating in the blood and improve tumor availability. Further reduction of off-target fluorescence could also be accomplished by reconfiguring huAR9.6 as an activatable probe.

As demonstrated in previous chapters, huAR9.6-IRDye800 is largely cleared by non-specific proteolysis in the liver. Because this is a key site of metastases in pancreatic cancer, high background signal may preclude detection of lesions at this site. To lower background signal, additional dyes should be considered. Several studies in the literature have shown that the charge of the dye chosen can significantly impact biodistribution. IRDye800 CW has a negative net charge, and exhibits high interaction with serum proteins, non-specific tissue uptake, and liver clearance. However, other dyes, such as ZW800, carry a net 0 charge, and thus have a different pattern of distribution. Studies showed that ZW800 has appreciably ultralow background signal and kidney clearance, which may yield optimal biodistribution for imaging PDAC [298]. IRDye800 was selected in this body of work to maintain consistency with the current clinical trial landscape, but additional dyes should be explored in future studies to optimize the biodistribution profile for imaging in the peritoneal cavity.

Antibodies are widely used for FGS and as therapeutics and delivery vehicles across many facets of oncology. High stability and target affinity are attractive attributes. However, antibodies are frequently criticized as targeting vehicles for many imaging modalities because of their long circulation time. While long circulation may pose a challenge for radionuclide development, this has potential advantages for FGS. As demonstrated in our dynamic contrast studies, and in many studies for antibody-based probes in FGS, there is a wide window in which imaging can occur, because antibodies continue to stick around within the tumor, allowing for greater flexibility in surgical planning. Furthermore, this could be beneficial in utilizing the targeting moiety for its

therapeutic potential, to allow for upfront treatment of tumors before subsequent imaging, using one dose of antibody.

However, the long circulation time of antibodies may increase background signal, and the large size of antibodies may reduce tumor penetration and result in heterogenous tumor distribution. To reduce extended circulation and background at earlier timepoints and improve tumor penetration, antibody fragments should be considered. Antibody fragments may improve penetration into the tumor, which reducing circulation time by removal of the Fc portion. Further studies are needed to elucidate the kinetics of these fragments and determine the ideal moiety size for different imaging applications. Antibody fragments may be more compatible with radiolabeling than a full IgG. However, loss of valency with a Fab fragment may impact binding, and thus should be considered as well.

Furthermore, the method of administration could be optimized to minimize background signal. Intravenous administration was explored for huAR9.6-IRDye800 in this body of work to maintain consistency with the current clinical landscape, but other methods of administration such as intratumoral or topical may hold interest for further investigation. Topical FGS probes, which can be sprayed onto the surgical field, or lesions in question, have demonstrated preliminary efficacy for several different probes, though these are mainly used with activatable probes. This method eliminates the longer circulation times of antibodies, and provides more rapid feedback about positive lesions, but may have limited depth of penetration into tumors [140].

5.2.7 Application in Multiple Tumor Types and in Metastatic Lesions.

MUC16 is an attractive target for imaging not only because it is highly expressed in pancreatic cancer, but because it is expressed in many other tumor types as well. MUC16, also known as CA125, is most well established as a biomarker in ovarian

cancer, and is expressed in more than 80% of these cancers [299]. Furthermore, CA125 serves as a serum biomarker for ovarian cancer. MUC16 has also been shown to have expression in esophageal, gastric, colon, lung, and breast cancers [201, 300]. Given the importance of surgical resection in many of these tumor types, future studies should investigate the utility of huAR9.6-IRDye800 as a FGS probe for these malignancies. Additionally, the expression of MUC16 is generally associated with an increased propensity for metastasis, and in pancreatic cancer, MUC16 has high expression in metastatic lesions, including lung, liver and lymph node metastases [203, 301]. Thus, studying applications of huAR9.6-IRDye800 for detecting peritoneal carcinomatosis, and for N1 disease, is critical. Determining the detection limits for identifying small lesions has not yet been investigated. These parameters are of critical importance for many tumor types. Investigating the ability of huAR9.6-IRDye800 to identify precursor PANIN lesions should also be investigated. MUC16 expression increases as PANIN lesions progress in pancreatic cancer. There is an unmet need for early detection in PDAC, and development of an FGS methodology for these early lesions has critical value, and warrants investigation.

5.2.8 Photoimmunotherapy

An area of application for further development of huAR9.6 is photoimmunotherapy. Treatment options are extremely limited for patients with pancreatic cancer [302]. For patients that are not candidates for surgical resection, typically chemotherapy or a combination of chemotherapy and radiation is the only treatment option. Even patients that undergo surgery typically receive some type of adjuvant chemotherapy. The results of these treatments are often limited to mild decreases in cancer-related symptoms and are accompanied by high levels of toxicity. In contrast to toxic chemotherapeutic regimens, photosensitizers can be administered in repeated doses and elicit minimal adverse effects [303]. Photosensitizers have been

used in a therapeutic technique called photodynamic therapy for decades [304]. There are still many clinical trials investigating photodynamic therapy in cancers, with promising results. The downside of this type of phototherapy is the lack of a targeting mechanism, thus there can be widespread off-target effects from exposure of non-cancerous organs to near-infrared (NIR) irradiation. In contrast, the newly developed method of photoimmunotherapy (PIT) uses an antibody to target photosensitizers. Studies have shown that antibody-targeted photosensitizers are toxic only when bound to cells, resulting in highly improved specificity and reduced off-target phototoxicity [305, 306]. Therefore, PIT can be a highly targeted non-toxic therapy. PIT has demonstrated high levels of pre-clinical efficacy for several cancer types and was recently fast-tracked to a Phase 3 clinical trial for head and neck cancer (NCT03769506). One of the obvious limitations to light-based therapy is depth of penetration. However, to address this concern in interstitial tumors like pancreatic cancer, recent studies have reported that fiber optic diffusers can be inserted adjacent to deep interstitial tumors, allowing for greater depth of penetration and ensuring that the PIT is reaching the tumor [307, 308]. Using this technique, it has been shown that PIT can kill cells at a distance of 10 mm from the light source [309]. Thus, there is high translational potential for reducing burden of deeply seeded pancreatic tumors in a clinical setting. The main mechanism of phototoxicity in *photodynamic* therapy is the production of reactive oxygen species and apoptosis. However, in *PIT,* necrosis has been cited as the mechanism of phototoxicity [310]. Studies have reported PIT-induced cell death in hypoxic conditions and in the presence of reactive oxygen species (ROS) scavengers. PIT has been shown to damage cancer cell membranes rather than their internal contents, causing an influx of water into cells, leading to cell bursting. In addition to inducing an immediate response (necrosis of cancer cells), PIT has been shown to enhance host anti-tumor immune responses in clinical trials and cause a super-enhanced permeability and retention effect

in tumors [311, 312]. Development of a photoimmunotherapeutic coincides with FGS development because of parallel fluorescence detection. Future studies should investigate the development of huAR9.6 as a PIT agent, to provide additional treatment options for PDAC patients as alternatives to more toxic therapeutic regimens. This could be applied intraoperatively, using fluorescence to detect lesions, and subsequently treating lesions and disease margins to improve outcomes after resection.

5.2.9 Development of a Diagnostic Imaging Agent

Preoperative imaging modalities play a critical role in diagnosis, staging, surgical planning, and treatment monitoring of pancreatic cancer [313]. Several different imaging modalities are currently used in the clinical space for diagnosis of PDAC, but these modalities are not without their limitations, particularly in their ability to detect small lesions, and to differentiate benign conditions from cancerous conditions. While nuclear imaging has not yet become the standard imaging modality in PDAC, preoperative nuclear imaging has demonstrated success in providing diagnostic information, post-surgical monitoring, and a road map to resection [314]. ImmunoPET has gained traction as a preoperative imaging modality for many cancer types. This modality combines the specific targeting properties of a monoclonal antibody, with the high sensitivity and resolution of PET imaging [315]. ImmunoPet pairs well with fluorescence imaging because both modalities can be used at low, nontoxic tracer doses with synergistic high spatial resolution [316]. Using a targeted PET agent could assist in surgical planning, and in determining candidates for surgery. Furthermore, preoperative imaging could be used as a screening tool to stratify patients' expression of a biomarker for FGS or therapy [9]. Applying either a multimodality probe in this setting or using a consistent target for preoperative and intraoperative imaging has the potential to improve continuity of imaging across stages of treatment, from diagnosis, to surgical resection, and

treatment monitoring and follow-up. Thus, future studies should investigate AR9.6 as the targeting moiety for an immunoPET agent.

5.2.10 Theranostic Development and ADCs

The monoclonal antibody used as a targeting moiety in AR9.6-IRDye800 lends itself to therapeutic development in parallel to optical imaging agent development. The work of Dr. Prakash Radhakrishnan at UNMC has demonstrated the efficacy of the AR9.6 antibody as a therapeutic for treating pancreatic cancer [301]. Treatment of MUC16-expressing tumors with AR9.6 resulted in a significant reduction in tumor growth and metastases in an orthotopic mouse model of pancreatic cancer. Mechanistically, these studies demonstrated that AR9.6 binding to MUC16 inhibited phosphorylation of Erb-B type receptors and subsequent downstream AKT/GSK3β signaling [301]. The potential for AR9.6 as a therapeutic has potential to be utilized in combination with fluorescence imaging as a theranostic agent. Preliminary studies from the initial therapeutic investigation, and the optical imaging agent described herein, warrant further study to develop a fluorescent biological that could be implemented to assist in treating PDAC as well as illuminating tumor lesions for surgery. While the evidence is still preliminary, because AR9.6 reduced metastatic spread in preclinical models, this agent may be beneficial to administrate as a neoadjuvant therapy to downstage tumors and increase patient eligibility for surgery, whereby the agent could also be used to visualize remaining lesions. Because of the long circulating time of antibodies, and the long retention of AR9.6 in tumors (shown preclinically in Chapters 2 +3) the feasibility for theranostic employment presents another promising avenue for future research. To that end, the huAR9.6-IRDye800 could also be employed as an antibody drug conjugate to deliver chemotherapeutics in addition to serving as an imaging agent. The versatility of antibodies in drug development, as well as their high stability and high target affinity, strengthens the potential uses for cancer treatment [224]. Furthermore, bispecific

antibodies, which have gained traction in the pipeline of many pharmaceutical companies, may be a direction to pursue as well. One of the challenges to targeting pancreatic cancer is that the dense desmoplasia surrounding the tumor presents a significant barrier for drug delivery. Reconfiguring AR9.6 to target MUC16 as well as a stromal target may improve tumor delivery. Potential targets of tumor stroma have been thoroughly described, including collagen-based biomarkers, the hedgehog signaling pathway, or hyaluronic acid [317–319]. Bispecificity could also be used to engage an immune target, and improve the immune response to tumors [320]. Preliminary success has been demonstrated in the literature with targeting CD3 with bispecific antibodies, which could pose a potential target for investigation in conjunction with MUC16 [321–324]. Alternatively, given the presence of mucins in a wide variety of cancers, a bispecific antibody could be developed to target two difference mucins (ie MUC1 and MUC16) simultaneously. Identifying multiple targets with one antibody may decrease concerns of patient heterogeneity for FGS probes. Additionally, modification of AR9.6 to engineer a biparatopic antibody (an antibody that simultaneously binds to overlapping epitopes on the same target) could be done to increase avidity for improved imaging and therapeutic efficacy [325]. Further research efforts in developing and expanding the utility of AR9.6 are anticipated to not be futile. Antibody therapies have undergone rapid growth in the therapeutics market, and there is still largely untapped growth potential. Oncology is perhaps the field most accessible for development of monoclonal antibody treatments. Thus, investigation of further theranostic applications is advisable.

Consideration of preoperative imaging applications described above, and therapeutic development in parallel to intraoperative imaging contextualizes this body of work in the larger continuum of cancer care. While the main focus of the project described within was really focused on intraoperative imaging, it is essential to investigate the role of this treatment modality along the spectrum of treatment that a

patient received during pancreatic cancer treatment, because surgery is only one of many critical pieces of care that a patient receives when they have pancreatic cancer. The concept of integrating AR9.6-IRDye800 in multiple settings is depicted in **Figure 48**. Development of applications for cancer treatment and diagnostics along with intraoperative imaging with AR9.6 permits the integration of the core targeting moiety into many aspects of cancer treatment, for continuity of care. While these research directions describe a wide array of projects, the ability to integrate one targeting moiety to improve diagnosis and staging, to surgical resection, therapy, and treatment monitoring, could be extremely beneficial to streamline care for MUC16-expressing PDAC patients, and is worthy of further investigation and development.

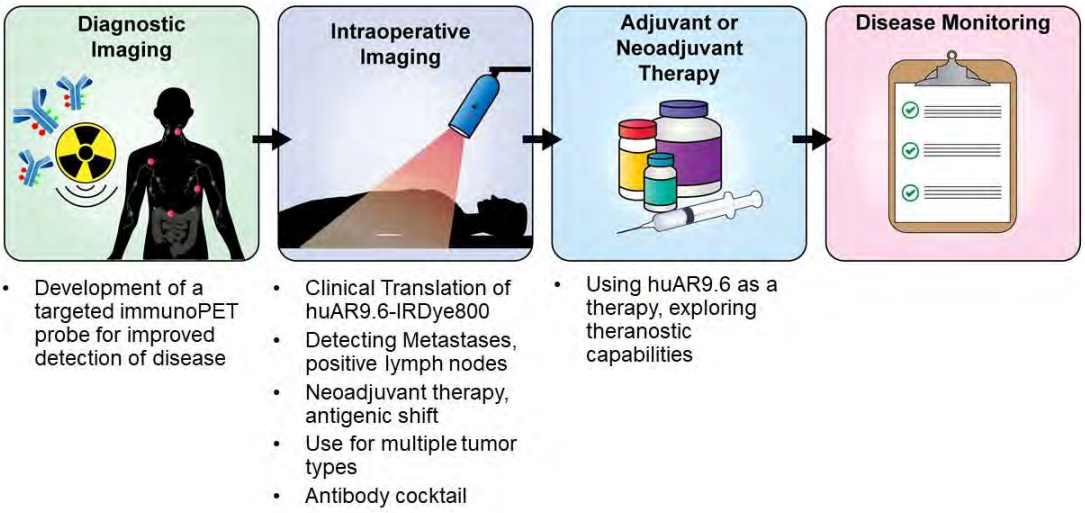

Figure 48: Contextualizing fluorescence-guided surgery in the continuum of cancer care.

Bibliography

1. Siegel RL, Miller KD, Fuchs HE, Jemal A (2021) Cancer Statistics, 2021. CA Cancer J Clin 71:7–33

2. Lu G, van den Berg NS, Martin BA, et al (2020) Tumour-Specific Fluorescence-Guided Surgery for Pancreatic Cancer Using Panitumumab-IRDye800CW: a Phase 1 Single-Centre, Open-label, Single-arm, Dose-Escalation Study. Lancet Gastroenterol Hepatol 5:753–764. doi: 10.1016/S2468-1253(20)30088-1

3. Tummers WS, Miller SE, Teraphongphom NT, et al (2018) Intraoperative Pancreatic Cancer Detection using Tumor-Specific Multimodality Molecular Imaging. Ann Surg Oncol 25:1880–1888. doi: 10.1245/s10434-018-6453-2

4. Strobel O, Neoptolemos J, Jäger D, Büchler MW (2019) Optimizing the Outcomes of Pancreatic Cancer Surgery. Nat Rev Clin Oncol 16:11–26. doi: 10.1038/s41571-018-0112-1

5. Olson MT, Ly QP, Mohs AM (2019) Fluorescence Guidance in Surgical Oncology: Challenges, Opportunities, and Translation. Mol Imaging Biol 21:200–218. doi: 10.1007/s11307-018-1239-2

6. Stewart B, Wild C (2014) World Cancer Report 2014. International Agency for Research on Cancer, https://publications.iarc.fr/Non-Series-Publications/World-Cancer-Reports/World-Cancer-Report-2014

7. Siegel RL, Miller KD, Jemal A (2018) Cancer Statistics, 2018. CA Cancer J Clin 68:7–30 . doi: 10.3322/caac.21442

8. Orosco RK, Tsien RY, Nguyen QT (2013) Fluorescence Imaging in Surgery. IEEE Rev Biomed Eng 6:178–87. doi: 10.1109/RBME.2013.2240294

9. Nguyen QT, Tsien RY (2013) Fluorescence-Guided Surgery with Live Molecular Navigation — a New Cutting Edge. Nat Rev Cancer 13:653–662. doi: 10.1038/nrc3566

10. Keating J, Tchou J, Okusanya O, et al (2016) Identification of Breast Cancer Margins Using Intraoperative Near-Infrared Imaging. J Surg Oncol 113:508–514. doi: 10.1002/jso.24167

11. Madajewski B, Judy BF, Mouchli A, et al (2012) Intraoperative Near-infrared Imaging of Surgical Wounds After Tumor Resections Can Detect Residual Disease. Clin Cancer Res 18:5741–51. doi: 10.1158/1078-0432.CCR-12-1188

12. Narod S (2016) Can Advanced-Stage Ovarian Cancer be Cured? Nat Rev Clin Oncol 13:255–261. doi: 10.1038/nrclinonc.2015.224

13. Witkowski ER, Smith JK, Tseng JF (2013) Outcomes Following Resection of Pancreatic Cancer. J Surg Oncol 107:97–103. doi: 10.1002/jso.23267

14. Shaib Y, Davila J, Naumann C, El-Serag H (2007) The Impact of Curative Intent Surgery on the Survival of Pancreatic Cancer Patients: A U.S. Population-Based Study. Am J Gastroenterol 102:1377–1382. doi: 10.1111/j.1572-0241.2007.01202.x

15. Rossi ML, Rehman AA, Gondi CS (2014) Therapeutic Options for the Management of Pancreatic Cancer. World J Gastroenterol 20:11142–11159. doi: 10.3748/wjg.v20.i32.11142

16. Tamburrino D, Partelli S, Crippa S, et al (2014) Selection Criteria in Resectable Pancreatic Cancer: a Biological and Morphological Approach. World J Gastroenterol 20:11210–5. doi: 10.3748/wjg.v20.i32.11210

17. Manuel H, Hidalgo M (2010) Pancreatic Cancer. N Engl J Med 362:1605–1617 .

doi: 10.1056/NEJMra0901557

18. Nick AM, Coleman RL, Ramirez PT, Sood AK (2015) A Framework for a Personalized Surgical Approach to Ovarian cancer. Nat Rev Clin Oncol 12:239–245. doi: 10.1038/nrclinonc.2015.26

19. Sehouli J, Grabowski JP (2017) Surgery for Recurrent Ovarian Cancer: Options and Limits. Best Pract Res Clin Obstet Gynaecol 41:88–95. doi: 10.1016/j.bpobgyn.2016.10.009

20. Liberale G, Vankerckhove S, Gomez Caldon M, et al (2016) Fluorescence Imaging after Indocyanine Green Injection for Detection of Peritoneal Metastases in Patients Undergoing Cytoreductive Surgery for Peritoneal Carcinomatosis from Colorectal Cancer: A Pilot Study. Ann Surg 264:1110–1115 . doi: 10.1097/SLA.0000000000001618

21. Hoogstins CE, Weixler B, Boogerd LS, et al (2017) In Search for Optimal Targets for Intraoperative Fluorescence Imaging of Peritoneal Metastasis From Colorectal Cancer. Biomark Cancer 9:1179299X1772825. doi: 10.1177/1179299X17728254

22. Barth CW, Gibbs SL (2017) Direct Administration of Nerve-Specific Contrast to Improve Nerve Sparing Radical Prostatectomy. Theranostics 7:573–593. doi: 10.7150/thno.17433

23. Gibbs-Strauss SL, Nasr KA, Fish KM, et al (2011) Nerve-Highlighting Fluorescent Contrast Agents for Image-Guided Surgery. Mol Imaging 10:91–101

24. Hussain T, Mastrodimos MB, Raju SC, et al (2015) Fluorescently Labeled Peptide Increases Identification of Degenerated Facial Nerve Branches During Surgery and Improves Functional Outcome. PLoS One 10:e0119600. doi: 10.1371/journal.pone.0119600

25. Hussain T, Nguyen LT, Whitney M, et al (2016) Improved Facial Nerve Identification During Parotidectomy with Fluorescently Labeled Peptide. Laryngoscope 126:2711–2717. doi: 10.1002/lary.26057

26. Whitney MA, Crisp JL, Nguyen LT, et al (2011) Fluorescent Peptides Highlight Peripheral Nerves During Surgery in Mice. Nat Biotechnol 29:352–356. doi: 10.1038/nbt.1764

27. He K, Zhou J, Yang F, et al (2018) Near-infrared Intraoperative Imaging of Thoracic Sympathetic Nerves: From Preclinical Study to Clinical Trial. Theranostics 8:304–313. doi: 10.7150/thno.22369

28. Hong G, Antaris AL, Dai H (2017) Near-infrared Fluorophores for Biomedical Imaging. Nat Biomed Eng 1:10. doi: 10.1038/s41551-016-0010

29. Moore GE, Peyton WT, French LA, Walker WW (1948) The Clinical Use of Fluorescein in Neurosurgery. J Neurosurg 5:392–398. doi: 10.3171/jns.1948.5.4.0392

30. Dilek O, Ihsan A, Tulay H (2011) Anaphylactic Reaction after Fluorescein Sodium Administration During Intracranial Surgery. J Clin Neurosci 18:430–1. doi: 10.1016/j.jocn.2010.06.012

31. Tanahashi S (1995) An Anaphylactoid Reaction After Administration of Fluorescein Sodium During Neurosurgery. Can J Anaesth 42:181–5. doi: 10.1213/01.ANE.0000227204.25547.B1

32. Mondal SB, Gao S, Zhu N, et al (2014) Real-time Fluorescence Image-Guided Oncologic Surgery. Adv Cancer Res 124:171–211. doi: 10.1016/B978-0-12-411638-2.00005-7

33. Thevarajah S, Huston TL, Simmons RM (2005) A Comparison of the Adverse

Reactions Associated with Isosulfan Blue versus Methylene Blue Dye in Sentinel Lymph Node Biopsy for Breast Cancer. Am J Surg 189:236–9. doi: 10.1016/j.amjsurg.2004.06.042

34. Kidd SA, Lancaster PAL, Anderson JC, et al (1996) Fetal Death After Exposure to Methylene Blue Dye During Mid-Trimester Amniocentesis in Twin Pregnancy. Prenat Diagn 16:39–47. doi: 10.1002/(SICI)1097-0223(199601)16:1<39::AID-PD789>3.0.CO;2-P

35. Zhang RR, Schroeder AB, Grudzinski JJ, et al (2017) Beyond the Margins: Real-Time Detection of Cancer Using Targeted Fluorophores. Nat Rev Clin Oncol 14:347–364

36. Verbeek FPR, van der Vorst JR, Schaafsma BE, et al (2013) Intraoperative Near Infrared Fluorescence Guided Identification of the Ureters Using Low Dose Methylene Blue: a First in Human Experience. J Urol 190:574–9. doi: 10.1016/j.juro.2013.02.3187

37. Dip FD, Moreira Grecco AD, Nguyen D, et al (2015) Ureter Identification Using Methylene Blue and Fluorescein. In: Fluorescence Imaging for Surgeons. Springer International Publishing, Cham, pp 327–332

38. Seif C, Martínez Portillo FJ, Osmonov DK, et al (2004) Methylene Blue Staining for Nerve-Sparing Operative Procedures: An Animal Model. Urology 63:1205–1208. doi: 10.1016/j.urology.2003.12.020

39. Osorio JA, Breshears JD, Arnaout O, et al (2015) Ultrasound-Guided Percutaneous Injection of Methylene Blue to Identify Nerve Pathology and Guide Surgery. Neurosurg Focus 39:E2. doi: 10.3171/2015.6.FOCUS15220

40. Candell L, Campbell MJ, Shen WT, et al (2014) Ultrasound-Guided Methylene

Blue Dye Injection for Parathyroid Localization in the Reoperative Neck. World J Surg 38:88–91. doi: 10.1007/s00268-013-2234-z

41. Kir G, Alimoglu O, Sarbay BC, Bas G (2014) Ex vivo Intra-arterial Methylene Blue Injection in the Operation Theater May Improve the Detection of Lymph Node Metastases in Colorectal Cancer. Pathol Res Pract 210:818–821. doi: 10.1016/j.prp.2014.09.003

42. Tummers QRJG, Schepers A, Hamming JF, et al (2015) Intraoperative Guidance in Parathyroid Surgery Using Near-Infrared Fluorescence Imaging and Low-Dose Methylene Blue. Surgery 158:1323–1330. doi: 10.1016/j.surg.2015.03.027

43. van der Vorst JR, Schaafsma BE, Verbeek FPR, et al (2014) Intraoperative Near-Infrared Fluorescence Imaging of Parathyroid Adenomas with Use of Low-Dose Methylene Blue. Head Neck 36:853–8. doi: 10.1002/hed.23384

44. van der Vorst JR, Vahrmeijer AL, Hutteman M, et al (2012) Near-Infrared Fluorescence Imaging of a Solitary Fibrous Tumor of the Pancreas Using Methylene Blue. World J Gastrointest Surg 4:180–4. doi: 10.4240/wjgs.v4.i7.180

45. Chu M, Wan Y (2009) Sentinel Lymph Node Mapping Using Near-Infrared Fluorescent Methylene Blue. J Biosci Bioeng 107:455–459. doi: 10.1016/J.JBIOSC.2008.11.011

46. Ferraro N, Barbarite E, Albert TR, et al (2016) The Role of 5-aminolevulinic Acid in Brain Tumor Surgery: a Systematic Review. Neurosurg Rev 39:545–555. doi: 10.1007/s10143-015-0695-2

47. Zhao S, Wu J, Wang C, et al (2013) Intraoperative Fluorescence-Guided Resection of High-Grade Malignant Gliomas Using 5-Aminolevulinic Acid–Induced Porphyrins: A Systematic Review and Meta-Analysis of Prospective Studies.

PLoS One 8:e63682. doi: 10.1371/journal.pone.0063682

48. Hadjipanayis CG, Widhalm G, Stummer W (2015) What is the Surgical Benefit of Utilizing 5-Aminolevulinic Acid for Fluorescence-Guided Surgery of Malignant Gliomas? Neurosurgery 77:663–73. doi: 10.1227/NEU.0000000000000929

49. Moiyadi A, Syed P, Srivastava S (2014) Fluorescence-Guided Surgery of Malignant Gliomas Based on 5-aminolevulinic Acid: Paradigm Shifts but not a Panacea. Nat Rev Cancer 14:146–146. doi: 10.1038/nrc3566-c1

50. Stummer W, Novotny A, Stepp H, et al (2000) Fluorescence-Guided Resection of Glioblastoma Multiforme Utilizing 5-ALA-Induced Porphyrins: a Prospective Study in 52 Consecutive Patients. J Neurosurg 93:1003–1013. doi: 10.3171/jns.2000.93.6.1003

51. Stummer W, Tonn J-C, Goetz C, et al (2014) 5-Aminolevulinic Acid-Derived Tumor Fluorescence: the Diagnostic Accuracy of Visible Fluorescence Qualities as Corroborated by Spectrometry and Histology and Postoperative Imaging. Neurosurgery 74:310-9-20. doi: 10.1227/NEU.0000000000000267

52. Schaafsma BE, Mieog JSD, Hutteman M, et al (2011) The Clinical Use of Indocyanine Green as a Near-Infrared Fluorescent Contrast Agent for Image-Guided Oncologic Surgery. J Surg Oncol 104:323–332. doi: 10.1002/jso.21943

53. Marshall M V, Rasmussen JC, Tan I-C, et al (2010) Near-Infrared Fluorescence Imaging in Humans with Indocyanine Green: A Review and Update. Open Surg Oncol J 2:12–25. doi: 10.2174/1876504101002010012

54. Namikawa T, Sato T, Hanazaki K (2015) Recent Advances in Near-Infrared Fluorescence-Guided Imaging Surgery Using Indocyanine Green. Surg Today 45:1467–1474. doi: 10.1007/s00595-015-1158-7

55. Pitsinis V, Provenzano E, Kaklamanis L, et al (2015) Indocyanine Green Fluorescence Mapping for Sentinel Lymph Node Biopsy in Early Breast Cancer. Surg Oncol 24:375–379. doi: 10.1016/j.suronc.2015.10.002

56. Sugie T, Kassim KA, Takeuchi M, et al (2010) A Novel Method for Sentinel Lymph Node biopsy by indocyanine green fluorescence technique in breast cancer. Cancers (Basel) 2:713–20 . doi: 10.3390/cancers2020713

57. Vahrmeijer AL, Hutteman M, van der Vorst JR, et al (2013) Image-guided cancer surgery using near-infrared fluorescence. Nat Rev Clin Oncol 10:507–518 . doi: 10.1038/nrclinonc.2013.123

58. Hill TK, Abdulahad A, Kelkar SS, et al (2015) Indocyanine Green-Loaded Nanoparticles for Image-Guided Tumor Surgery. Bioconjug Chem 26:294–303 . doi: 10.1021/bc5005679

59. Kraft JC, Ho RJY (2014) Interactions of Indocyanine Green and Lipid in Enhancing Near-Infrared Fluorescence Properties: The Basis for Near-Infrared Imaging *in Vivo*. Biochemistry 53:1275–1283 . doi: 10.1021/bi500021j

60. Moore LS, Rosenthal EL, Chung TK, et al (2017) Characterizing the Utility and Limitations of Repurposing an Open-Field Optical Imaging Device for Fluorescence-Guided Surgery in Head and Neck Cancer Patients. J Nucl Med 58:246–251. doi: 10.2967/jnumed.115.171413

61. Korb ML, Hartman YE, Kovar J, et al (2014) Use of Monoclonal Antibody-IRDye800CW Bioconjugates in the Resection of Breast Cancer HHS Public Access. J Surg Res J Surg Res May 111:119–128. doi: 10.1016/j.jss.2013.11.1089

62. Rosenthal EL, Warram JM, de Boer E, et al (2015) Safety and Tumor Specificity

of Cetuximab-IRDye800 for Surgical Navigation in Head and Neck Cancer. Clin Cancer Res 21:3658–3666. doi: 10.1158/1078-0432.CCR-14-3284

63. Lu Y, Su Y, Zhou Y, et al (2013) In Vivo Behavior of Near Infrared-Emitting Quantum Dots. doi: 10.1016/j.biomaterials.2013.02.054

64. Luo S, Zhang E, Su Y, et al (2011) A Review of NIR Dyes in Cancer Targeting and Imaging. Biomaterials 32:7127–7138. doi: 10.1016/j.biomaterials.2011.06.024

65. Ji X, Peng F, Zhong Y, et al (2014) Fluorescent Quantum Dots: Synthesis, Biomedical Optical Imaging, and Biosafety Assessment. Colloids Surfaces B Biointerfaces 124:132–139. doi: https://doi.org/10.1016/j.colsurfb.2014.08.036

66. Smith AM, Duan H, Mohs AM, Nie S (2008) Bioconjugated Quantum Dots for in Vivo Molecular and Cellular Imaging. Adv Drug Deliv Rev 60:1226–1240. doi: 10.1016/J.ADDR.2008.03.015

67. Tansi FL, Rüger R, Rabenhold M, et al (2015) Fluorescence-Quenching of a Liposomal-Encapsulated Near-Infrared Fluorophore as a Tool for in Vivo Optical Imaging. J Vis Exp e52136. doi: 10.3791/52136

68. Lisy M-R, Goermar A, Thomas C, et al (2008) In Vivo Near-infrared Fluorescence Imaging of Carcinoembryonic Antigen–expressing Tumor Cells in Mice. Radiology 247:779–787. doi: 10.1148/radiol.2472070123

69. Pauli J, Brehm R, Spieles M, et al (2010) Novel Fluorophores as Building Blocks for Optical Probes for In Vivo Near Infrared Fluorescence (NIRF) Imaging. J Fluoresc 20:681–693. doi: 10.1007/s10895-010-0603-7

70. Pansare VJ, Hejazi S, Faenza WJ, Prud'homme RK (2012) Review of Long-Wavelength Optical and NIR Imaging Materials: Contrast Agents, Fluorophores, and Multifunctional Nano Carriers. Chem Mater 24:812–827. doi:

10.1021/cm2028367

71. Hill TK, Mohs AM (2016) Image-Guided Tumor Surgery: Will There be a Role for Fluorescent Nanoparticles? Wiley Interdiscip Rev Nanomedicine Nanobiotechnology 8:498–511. doi: 10.1002/wnan.1381

72. Gioux S, Kianzad V, Ciocan R, et al (2009) High-Power, Computer-Controlled, Light-Emitting Diode-Based Light Sources for Fluorescence Imaging and Image-Guided Surgery. Mol Imaging 8:156–65

73. Gioux S, Choi HS, Frangioni J V (2010) Image-Guided Surgery using Invisible Near-Infrared Light: Fundamentals of Clinical Translation. Mol Imaging 9:237–255

74. DSouza A V, Lin H, Henderson ER, et al (2016) Review of Fluorescence Guided Surgery Systems: Identification of Key Performance Capabilities Beyond Indocyanine Green Imaging. J Biomed Opt 21:80901. doi: 10.1117/1.JBO.21.8.080901

75. Zhu B, Sevick-Muraca EM (2015) A Review of Performance of Near-Infrared Fluorescence Imaging Devices Used in Clinical Studies. Br J Radiol 88:20140547 . doi: 10.1259/bjr.20140547

76. Matsumura Y, Maeda H, Jain RK, et al (1986) A New Concept for Macromolecular Therapeutics in Cancer Chemotherapy: Mechanism of Tumoritropic Accumulation of Proteins and the Antitumor Agent Smancs. Cancer Res 46:6387–92. doi: 10.1158/0008-5472.can-12-4561

77. Bertrand N, Wu J, Xu X, et al (2014) Cancer Nanotechnology: The Impact of Passive and Active Targeting in the Era of Modern Cancer Biology. Adv Drug Deliv Rev 66:2–25. doi: 10.1016/j.addr.2013.11.009

78. Maeda H, Tsukigawa K, Fang J (2016) A Retrospective 30 Years After Discovery

of the Enhanced Permeability and Retention Effect of Solid Tumors: Next-Generation Chemotherapeutics and Photodynamic Therapy-Problems, Solutions, and Prospects. Microcirculation 23:173–182. doi: 10.1111/micc.12228

79. Kharaishvili G, Simkova D, Bouchalova K, et al (2014) The Role of Cancer-Associated Fibroblasts, Solid Stress and Other Microenvironmental Factors in Tumor Progression and Therapy Resistance. Cancer Cell Int 14:41. doi: 10.1186/1475-2867-14-41

80. Fang J, Nakamura H, Maeda H (2011) The EPR effect: Unique Features of Tumor Blood Vessels for Drug Delivery, Factors Involved, and Limitations and Augmentation of the Effect. Adv. Drug Deliv. Rev. 63:136–151

81. Carmeliet P, Jain RK (2000) Angiogenesis in Cancer and Other Diseases. Nature 407:249

82. Bergers G, Benjamin LE (2003) Angiogenesis: Tumorigenesis and the Angiogenic Switch. Nat Rev Cancer 3:401–410. doi: 10.1038/nrc1093

83. Morikawa S, Baluk P, Kaidoh T, et al (2002) Abnormalities in Pericytes on Blood Vessels and Endothelial Sprouts in Tumors. Am J Pathol 160:985–1000. doi: 10.1016/S0002-9440(10)64920-6

84. Padera TP, Kadambi A, di Tomaso E, et al (2002) Lymphatic Metastasis in the Absence of Functional Intratumor Lymphatics. Science 296:1883–6. doi: 10.1126/science.1071420

85. Sriraman SK, Aryasomayajula B, Torchilin VP (2014) Barriers to Drug Delivery in Solid Tumors. Tissue barriers 2:e29528. doi: 10.4161/tisb.29528

86. Maeda H (2012) Macromolecular Therapeutics in Cancer Treatment: The EPR Effect and Beyond. J Control Release 164:138–144. doi:

10.1016/J.JCONREL.2012.04.038

87. Nakamura H, Etrych T, Chytil P, et al (2014) Two Step Mechanisms of Tumor Selective Delivery of N-(2-hydroxypropyl)methacrylamide Copolymer Conjugated with Pirarubicin via an Acid-Cleavable Linkage. J Control Release 174:81–87. doi: 10.1016/J.JCONREL.2013.11.011

88. Kobayashi H, Watanabe R, Choyke PL (2013) Improving Conventional Enhanced Permeability and Retention (EPR) Effects; What is the Appropriate Target? Theranostics 4:81–9. doi: 10.7150/thno.7193

89. Nakamura Y, Mochida A, Choyke PL, Kobayashi H (2016) Nanodrug Delivery: Is the Enhanced Permeability and Retention Effect Sufficient for Curing Cancer? Bioconjug. Chem. 27:2225–2238

90. Jain RK, Stylianopoulos T (2010) Delivering Nanomedicine to Solid Tumors. Nat Rev Clin Oncol 7:653–664. doi: 10.1038/nrclinonc.2010.139

91. Padera TP, Stoll BR, Tooredman JB, et al (2004) Pathology: Cancer Cells Compress Intratumour Vessels. Nature 427:695–695. doi: 10.1038/427695a

92. Jain RK, Martin JD, Stylianopoulos T (2014) The Role of Mechanical Forces in Tumor Growth and Therapy. Annu Rev Biomed Eng 16:321–46. doi: 10.1146/annurev-bioeng-071813-105259

93. Heldin C-H, Rubin K, Pietras K, Östman A (2004) High Interstitial Fluid Pressure — an Obstacle in Cancer Therapy. Nat Rev Cancer 4:806–813. doi: 10.1038/nrc1456

94. Baxter LT, Jain ' RK (1989) Transport of Fluid and Macromolecules in Tumors I. Role of Interstitial Pressure and Convection. Microvasc Res 37:77–104

95. Wu M, Frieboes HB, Chaplain MAJ, et al (2014) The Effect of Interstitial Pressure on Therapeutic Agent Transport: Coupling with the Tumor Blood and Lymphatic Vascular Systems. J Theor Biol 355:194–207. doi: 10.1016/j.jtbi.2014.04.012

96. Miao L, Lin CM, Huang L (2015) Stromal Barriers and Strategies for the Delivery of Nanomedicine to Desmoplastic Tumors. J Control Release 219:192–204. doi: 10.1016/j.jconrel.2015.08.017

97. May JP, Li S-D (2013) Hyperthermia-Induced Drug Targeting. Expert Opin Drug Deliv 10:511–527. doi: 10.1517/17425247.2013.758631

98. Durymanov MO, Rosenkranz AA, Sobolev AS (2015) Current Approaches for Improving Intratumoral Accumulation and Distribution of Nanomedicines. Theranostics 5:1007–20. doi: 10.7150/thno.11742

99. Ojha T, Pathak V, Shi Y, et al (2017) Pharmacological and Physical Vessel Modulation Strategies to Improve EPR-Mediated Drug Targeting to Tumors ☆. doi: 10.1016/j.addr.2017.07.007

100. Yokoi K, Tanei T, Godin B, et al (2014) Serum Biomarkers for Personalization of Nanotherapeutics-Based Therapy in Different Tumor and Organ Microenvironments. Cancer Lett 345:48–55. doi: 10.1016/j.canlet.2013.11.015

101. Yokoi K, Kojic M, Milosevic M, et al (2014) Capillary-Wall Collagen as a Biophysical Marker of Nanotherapeutic Permeability into the Tumor Microenvironment. Cancer Res 74:4239–46. doi: 10.1158/0008-5472.CAN-13-3494

102. Bolkestein M, de Blois E, Koelewijn SJ, et al (2016) Investigation of Factors Determining the Enhanced Permeability and Retention Effect in Subcutaneous Xenografts. J Nucl Med 57:601–7. doi: 10.2967/jnumed.115.166173

103. Miller J, Wang ST, Orukari I, et al (2017) Perfusion-Based Fluorescence Imaging Method Delineates Diverse Organs and Identifies Multifocal Tumors Using Generic Near Infrared Molecular Probes. J Biophotonics. doi: 10.1002/jbio.201700232

104. Srinivasarao M, Galliford C V., Low PS (2015) Principles in the Design of Ligand-Targeted Cancer Therapeutics and Imaging Agents. Nat Rev Drug Discov 14:203–219 . doi: 10.1038/nrd4519

105. Choi HS, Gibbs SL, Lee JH, et al (2013) Targeted Zwitterionic Near-Infrared Fluorophores for Improved Optical Imaging. Nat Biotechnol 31:148–153. doi: 10.1038/nbt.2468

106. Nagaya T, Nakamura YA, Choyke PL, Kobayashi H (2017) Fluorescence-Guided Surgery. Front Oncol 7:314. doi: 10.3389/fonc.2017.00314

107. Warram JM, de Boer E, Sorace AG, et al (2014) Antibody-Based Imaging Strategies for Cancer. Cancer Metastasis Rev 33:809–22. doi: 10.1007/s10555-014-9505-5

108. Hiroshima Y, Lwin TM, Murakami T, et al (2016) Effective Fluorescence-Guided Surgery of Liver Metastasis using a Fluorescent anti-CEA Antibody. J Surg Oncol 114:951–958. doi: 10.1002/jso.24462

109. Lwin TM, Murakami T, Miyake K, et al (2018) Tumor-Specific Labeling of Pancreatic Cancer Using a Humanized Anti-CEA Antibody Conjugated to a Near-Infrared Fluorophore. Ann Surg Oncol 25:1079–1085. doi: 10.1245/s10434-018-6344-6

110. Moore LS, Rosenthal EL, de Boer E, et al (2017) Effects of an Unlabeled Loading Dose on Tumor-Specific Uptake of a Fluorescently Labeled Antibody for Optical

Surgical Navigation. Mol Imaging Biol 19:610–616. doi: 10.1007/s11307-016-1022-1

111. Freise AC, Wu AM (2015) In vivo Imaging with Antibodies and Engineered Fragments. Mol Immunol 67:142–52. doi: 10.1016/j.molimm.2015.04.001

112. Kobayashi H, Choyke PL, Ogawa M (2016) Monoclonal Antibody-Based Optical Molecular Imaging Probes; Considerations and Caveats in Chemistry, Biology and Pharmacology. Curr Opin Chem Biol 33:32–38. doi: 10.1016/j.cbpa.2016.05.015

113. Mazzocco C, Fracasso G, Germain-Genevois C, et al (2016) In vivo Imaging of Prostate Cancer Using an anti-PSMA scFv Fragment as a Probe. Sci Rep 6:23314. doi: 10.1038/srep23314

114. Sonn GA, Behesnilian AS, Jiang ZK, et al (2016) Fluorescent Image-Guided Surgery with an Anti-Prostate Stem Cell Antigen (PSCA) Diabody Enables Targeted Resection of Mouse Prostate Cancer Xenografts in Real Time. Clin Cancer Res 22:1403–12. doi: 10.1158/1078-0432.CCR-15-0503

115. Owens B (2017) Faster, Deeper, Smaller—the Rise of Antibody-like Scaffolds. Nat Biotechnol 35:602–603. doi: 10.1038/nbt0717-602

116. Sexton K, Tichauer K, Samkoe KS, et al (2013) Fluorescent Affibody Peptide Penetration in Glioma Margin Is Superior to Full Antibody. PLoS One 8:e60390 . doi: 10.1371/journal.pone.0060390

117. de Souza ALR, Marra K, Gunn J, et al (2017) Fluorescent Affibody Molecule Administered In Vivo at a Microdose Level Labels EGFR Expressing Glioma Tumor Regions. Mol Imaging Biol 19:41–48. doi: 10.1007/s11307-016-0980-7

118. Samkoe KS, Gunn JR, Marra K, et al (2017) Toxicity and Pharmacokinetic Profile for Single-Dose Injection of ABY-029: a Fluorescent Anti-EGFR Synthetic Affibody

Molecule for Human Use. Mol Imaging Biol 19:512–521. doi: 10.1007/s11307-016-1033-y

119. Chakravarty R, Goel S, Cai W (2014) Nanobody: the "Magic bullet"; for Molecular Imaging? Theranostics 4:386–98. doi: 10.7150/thno.8006

120. Debie P, Vanhoeij M, Poortmans N, et al (2017) Improved Debulking of Peritoneal Tumor Implants by Near-Infrared Fluorescent Nanobody Image Guidance in an Experimental Mouse Model. Mol Imaging Biol 1–7. doi: 10.1007/s11307-017-1134-2

121. Staderini M, Megia-Fernandez A, Dhaliwal K, Bradley M (2017) Peptides for Optical Medical Imaging and Steps Towards Therapy. Bioorg Med Chem. doi: 10.1016/J.BMC.2017.09.039

122. Sun X, Li Y, Liu T, et al (2017) Peptide-Based Imaging Agents for Cancer Detection. Adv Drug Deliv Rev 110–111:38–51. doi: 10.1016/j.addr.2016.06.007

123. Handgraaf HJM, Boonstra MC, Prevoo HAJM, et al (2017) Real-Time Near-Infrared Fluorescence Imaging using cRGD-ZW800-1 for Intraoperative Visualization of Multiple Cancer Types. Oncotarget 8:21054–21066. doi: 10.18632/oncotarget.15486

124. Sato K, Gorka AP, Nagaya T, et al (2016) Role of Fluorophore Charge on the In Vivo Optical Imaging Properties of Near-Infrared Cyanine Dye/Monoclonal Antibody Conjugates. Bioconjug Chem 27:404–413. doi: 10.1021/acs.bioconjchem.5b00492

125. Yin X, Wang M, Wang H, et al (2017) Evaluation of Neurotensin Receptor 1 as a Potential Imaging Target in Pancreatic Ductal Adenocarcinoma. Amino Acids 49:1325–1335. doi: 10.1007/s00726-017-2430-5

126. Wyatt LC, Lewis JS, Andreev OA, et al (2017) Applications of pHLIP Technology for Cancer Imaging and Therapy. Trends Biotechnol 35:653–664. doi: 10.1016/j.tibtech.2017.03.014

127. Golijanin J, Amin A, Moshnikova A, et al (2016) Targeted Imaging of Urothelium Carcinoma in Human Bladders by an ICG pHLIP Peptide ex Vivo. Proc Natl Acad Sci U S A 113:11829–11834. doi: 10.1073/pnas.1610472113

128. Karabadzhak AG, An M, Yao L, et al (2014) pHLIP-FIRE, a Cell Insertion-Triggered Fluorescent Probe for Imaging Tumors Demonstrates Targeted Cargo Delivery in Vivo. ACS Chem Biol 9:2545–53. doi: 10.1021/cb500388m

129. Darmostuk M, Rimpelova S, Gbelcova H, Ruml T (2015) Current Approaches in SELEX: An Update to Aptamer Selection Technology. Biotechnol Adv 33:1141–1161. doi: 10.1016/j.biotechadv.2015.02.008

130. Hori S, Herrera A, Rossi J, Zhou J (2018) Current Advances in Aptamers for Cancer Diagnosis and Therapy. Cancers (Basel) 10:9 . doi: 10.3390/cancers10010009

131. Huang YF, Chang HT, Tan W (2008) Cancer Cell Targeting Using Multiple Aptamers Conjugated on Nanorods. Anal Chem 80:567–572. doi: 10.1021/ac702322j

132. Tang J, Huang N, Zhang X, et al (2017) Aptamer-conjugated PEGylated Quantum Dots Targeting Epidermal Growth Factor Receptor Variant III for Fluorescence Imaging of Glioma. Int J Nanomedicine Volume 12:3899–3911. doi: 10.2147/IJN.S133166

133. Tan J, Yang N, Zhong L, et al (2017) A New Theranostic System Based on Endoglin Aptamer Conjugated Fluorescent Silica Nanoparticles. Theranostics

7:4862–4876. doi: 10.7150/thno.19101

134. Bazak R, Houri M, El Achy S, et al (2015) Cancer Active Targeting by Nanoparticles: a Comprehensive Review of Literature. J Cancer Res Clin Oncol 141:769–84. doi: 10.1007/s00432-014-1767-3

135. Duman FD, Erkisa M, Khodadust R, et al (2017) Folic Acid-Conjugated Cationic Ag_2S Quantum Dots for Optical Imaging and Selective Doxorubicin Delivery to HeLa cells. Nanomedicine 12:2319–2333. doi: 10.2217/nnm-2017-0180

136. Predina JD, Newton AD, Connolly C, et al (2018) Identification of a Folate Receptor-Targeted Near-Infrared Molecular Contrast Agent to Localize Pulmonary Adenocarcinomas. Mol Ther 26:390–403. doi: 10.1016/j.ymthe.2017.10.016

137. Hoogstins CES, Tummers QRJG, Gaarenstroom KN, et al (2016) A Novel Tumor-Specific Agent for Intraoperative Near-Infrared Fluorescence Imaging: A Translational Study in Healthy Volunteers and Patients with Ovarian Cancer. Clin Cancer Res 22:2929–38. doi: 10.1158/1078-0432.CCR-15-2640

138. Keating JJ, Runge JJ, Singhal S, et al (2017) Intraoperative Near-Infrared Fluorescence Imaging Targeting Folate Receptors Identifies Lung Cancer in a Large-Animal Model. Cancer 123:1051–1060. doi: 10.1002/cncr.30419

139. Zhu M, Sheng Z, Jia Y, et al (2017) Indocyanine Green-holo-Transferrin Nanoassemblies for Tumor-Targeted Dual-Modal Imaging and Photothermal Therapy of Glioma. ACS Appl Mater Interfaces 9:39249–39258. doi: 10.1021/acsami.7b14076

140. Mochida A, Ogata F, Nagaya T, et al (2018) Activatable Fluorescent Probes in Fluorescence-Guided Surgery: Practical Considerations. Bioorg Med Chem 26:925–930. doi: 10.1016/j.bmc.2017.12.002

141. Kobayashi H, Choyke PL (2011) Target-Cancer-Cell-Specific Activatable Fluorescence Imaging Probes: Rational Design and in Vivo Applications. Acc Chem Res 44:83–90. doi: 10.1021/ar1000633

142. Chinen AB, Guan CM, Ferrer JR, et al (2015) Nanoparticle Probes for the Detection of Cancer Biomarkers, Cells, and Tissues by Fluorescence. Chem Rev 115:10530–10574. doi: 10.1021/acs.chemrev.5b00321

143. Choi HS, Liu W, Liu F, et al (2010) Design Considerations for Tumour-Targeted Nanoparticles. Nat Nanotechnol 5:42–47. doi: 10.1038/nnano.2009.314

144. Chi C, Zhang Q, Mao Y, et al (2015) Increased Precision of Orthotopic and Metastatic Breast Cancer Surgery Guided by Matrix Metalloproteinase-Activatable Near-Infrared Fluorescence Probes. Sci Rep 5:14197. doi: 10.1038/srep14197

145. Alley SC, Okeley NM, Senter PD (2010) Antibody–Drug Conjugates: Targeted Drug Delivery for Cancer. Curr Opin Chem Biol 14:529–537. doi: 10.1016/J.CBPA.2010.06.170

146. Matsuzaki S, Serada S, Hiramatsu K, et al (2018) Anti-Glypican-1 Antibody-Drug Conjugate Exhibits Potent Preclinical Antitumor Activity Against Glypican-1 Positive Uterine Cervical Cancer. Int J Cancer 142:1056–1066. doi: 10.1002/ijc.31124

147. Su C-Y, Chen M, Chen L-C, et al (2018) Bispecific Antibodies (anti-mPEG/anti-HER2) for Active Tumor Targeting of Docetaxel (DTX)-loaded mPEGylated Nanocarriers to Enhance the Chemotherapeutic Efficacy of HER2-Overexpressing Tumors. Drug Deliv 25:1066–1079. doi: 10.1080/10717544.2018.1466936

148. Semkina AS, Abakumov MA, Skorikov AS, et al (2018) Multimodal Doxorubicin Loaded Magnetic Nanoparticles for VEGF Targeted Theranostics of Breast

Cancer. Nanomedicine Nanotechnology, Biol Med. doi: 10.1016/j.nano.2018.04.019

149. Huang R, Li J, Kebebe D, et al (2018) Cell Penetrating Peptides Functionalized Gambogic Acid-Nanostructured Lipid Carrier for Cancer Treatment. Drug Deliv 25:757–765. doi: 10.1080/10717544.2018.1446474

150. Deshpande P, Jhaveri A, Pattni B, et al (2018) Transferrin and Octaarginine Modified Dual-Functional Liposomes with Improved Cancer Cell Targeting and Enhanced Intracellular Delivery for the Treatment of Ovarian Cancer. Drug Deliv 25:517–532. doi: 10.1080/10717544.2018.1435747

151. Alibolandi M, Ramezani M, Abnous K, Hadizadeh F (2016) AS1411 Aptamer-Decorated Biodegradable Polyethylene Glycol–Poly(lactic-co-glycolic acid) Nanopolymersomes for the Targeted Delivery of Gemcitabine to Non–Small Cell Lung Cancer In Vitro. J Pharm Sci 105:1741–1750. doi: 10.1016/J.XPHS.2016.02.021

152. Lin R, Huang J, Wang L, et al (2018) Bevacizumab and Near Infrared Probe Conjugated Iron Oxide Nanoparticles for Vascular Endothelial Growth Factor Targeted MR and Optical Imaging. Biomater Sci. doi: 10.1039/C8BM00225H

153. Rijpkema M, Oyen WJ, Bos D, et al (2014) SPECT- and Fluorescence Image-Guided Surgery Using a Dual-Labeled Carcinoembryonic Antigen-Targeting Antibody. J Nucl Med 55:1519–24. doi: 10.2967/jnumed.114.142141

154. Zhang X-S, Xuan Y, Yang X-Q, et al (2018) A Multifunctional Targeting Probe with Dual-Mode Imaging and Photothermal Therapy Used in Vivo. J Nanobiotechnology 16:42. doi: 10.1186/s12951-018-0367-9

155. Yang H-M, Park CW, Park S, Kim J-D (2018) Cross-linked Magnetic

Nanoparticles with a Biocompatible Amide Bond for Cancer-Targeted Dual Optical/Magnetic Resonance Imaging. Colloids Surfaces B Biointerfaces 161:183–191. doi: 10.1016/J.COLSURFB.2017.10.049

156. Kommidi H, Guo H, Nurili F, et al (2018) ^{18} F-Positron Emitting/Trimethine Cyanine-Fluorescent Contrast for Image-Guided Prostate Cancer Management. J Med Chem 61:4256–4262. doi: 10.1021/acs.jmedchem.8b00240

157. Wang X, Yan J, Pan D, et al (2018) Polyphenol-Poloxamer Self-Assembled Supramolecular Nanoparticles for Tumor NIRF/PET Imaging. Adv Healthc Mater 1701505. doi: 10.1002/adhm.201701505

158. Chi C, Du Y, Ye J, et al (2014) Intraoperative Imaging-Guided Cancer Surgery: from Current Fluorescence Molecular Imaging Methods to Future Multi-Modality Imaging Technology. Theranostics 4:1072–84. doi: 10.7150/thno.9899

159. Hausner SH, Bauer N, Hu LY, et al (2015) The Effect of Bi-Terminal PEGylation of an Integrin $\alpha v\beta_6$-Targeted ^{18}F Peptide on Pharmacokinetics and Tumor Uptake. J Nucl Med 56:784–90. doi: 10.2967/jnumed.114.150680

160. Han Z, Li Y, Roelle S, et al (2017) Targeted Contrast Agent Specific to an Oncoprotein in Tumor Microenvironment with the Potential for Detection and Risk Stratification of Prostate Cancer with MRI. Bioconjug Chem 28:1031–1040. doi: 10.1021/acs.bioconjchem.6b00719

161. Rosenthal EL, Warram JM, Bland KI, Zinn KR (2015) The Status of Contemporary Image-Guided Modalities in Oncologic Surgery. Ann Surg 261:46–55. doi: 10.1097/SLA.0000000000000622

162. Kim MJ, Kim CS, Park YS, et al (2016) The Efficacy of Intraoperative Frozen Section Analysis During Breast-Conserving Surgery for Patients with Ductal

Carcinoma In Situ. Breast Cancer (Auckl) 10:205–210. doi: 10.4137/BCBCR.S40868

163. Ko S, Chun YK, Kang SS, Hur MH (2017) The Usefulness of Intraoperative Circumferential Frozen-Section Analysis of Lumpectomy Margins in Breast-Conserving Surgery. J Breast Cancer 20:176–182. doi: 10.4048/jbc.2017.20.2.176

164. Pleijhuis RG, Graafland M, de Vries J, et al (2009) Obtaining Adequate Surgical Margins in Breast-Conserving Therapy for Patients with Early-Stage Breast Cancer: Current Modalities and Future Directions. Ann Surg Oncol 16:2717–2730 . doi: 10.1245/s10434-009-0609-z

165. Petropoulou T, Kapoula A, Mastoraki A, et al (2017) Imprint Cytology Versus Frozen Section Analysis for Intraoperative Assessment of Sentinel Lymph Node in Breast Cancer. Breast cancer. Dove Med Press 9:325–330. doi: 10.2147/BCTT.S130987

166. Barth CW, Schaefer JM, Rossi VM, et al (2017) Optimizing Fresh Specimen Staining for Rapid Identification of Tumor Biomarkers During Surgery. Theranostics 7:4722–4734. doi: 10.7150/thno.21527

167. Hutteman M, Choi HS, Mieog JSD, et al (2011) Clinical Translation of ex Vivo Sentinel Lymph Node Mapping for Colorectal Cancer Using Invisible Near-Infrared Fluorescence Light. Ann Surg Oncol 18:1006–1014. doi: 10.1245/s10434-010-1426-0

168. Cutter JL, Cohen NT, Wang J, et al (2012) Topical Application of Activity-Based Probes for Visualization of Brain Tumor Tissue. PLoS One 7:e33060. doi: 10.1371/journal.pone.0033060

169. Tipirneni KE, Warram JM, Moore LS, et al (2017) Oncologic Procedures Amenable to Fluorescence-guided Surgery. Ann Surg 266:36–47. doi: 10.1097/SLA.0000000000002127

170. Barth CW, Gibbs SL (2020) Fluorescence Image-Guided Surgery – a Perspective on Contrast Agent Development. Proc SPIE--the Int Soc Opt Eng 11222:18. doi: 10.1117/12.2545292

171. Tummers WS, Warram JM, Tipirneni KE, et al (2017) Regulatory Aspects of Optical Methods and Exogenous Targets for Cancer Detection. Cancer Res 77:2197 LP-2206. doi: 10.1158/0008-5472.CAN-16-3217

172. Mondal SB, Gao S, Zhu N, et al (2015) Binocular Goggle Augmented Imaging and Navigation System provides real-time fluorescence image guidance for tumor resection and sentinel lymph node mapping. Sci Rep 5:12117. doi: 10.1038/srep12117

173. Mondal SB, Gao S, Zhu N, et al (2017) Optical See-Through Cancer Vision Goggles Enable Direct Patient Visualization and Real-Time Fluorescence-Guided Oncologic Surgery. Ann Surg Oncol 24:1897–1903. doi: 10.1245/s10434-017-5804-8

174. Goldstein SD, Heaton TE, Bondoc A, et al (2021) Evolving Applications of Fluorescence Guided Surgery in Pediatric Surgical Oncology: A Practical Guide for Surgeons. J Pediatr Surg 56:215–223. doi: 10.1016/J.JPEDSURG.2020.10.013

175. Esposito C, Settimi A, Del Conte F, et al (2020) Image-Guided Pediatric Surgery Using Indocyanine Green (ICG) Fluorescence in Laparoscopic and Robotic Surgery. Front Pediatr 0:314. doi: 10.3389/FPED.2020.00314

176. Boogerd LSF, Hoogstins CES, Schaap DP, et al (2018) Safety and Effectiveness of SGM-101, a Fluorescent Antibody Targeting Carcinoembryonic Antigen, for Intraoperative Detection of Colorectal Cancer: a Dose-Escalation Pilot Study. Lancet Gastroenterol Hepatol 3:181–191. doi: 10.1016/S2468-1253(17)30395-3

177. Patil CG, Walker DG, Miller DM, et al (2019) Phase 1 Safety, Pharmacokinetics, and Fluorescence Imaging Study of Tozuleristide (BLZ-100) in Adults With Newly Diagnosed or Recurrent Gliomas. Neurosurgery 85:E641–E649. doi: 10.1093/NEUROS/NYZ125

178. Payne WM, Hill TK, Svechkarev D, et al (2017) Multimodal Imaging Nanoparticles Derived from Hyaluronic Acid for Integrated Preoperative and Intraoperative Cancer Imaging. Contrast Media Mol Imaging 2017:1–14. doi: 10.1155/2017/9616791

179. Gao N, Bozeman EN, Qian W, et al (2017) Tumor Penetrating Theranostic Nanoparticles for Enhancement of Targeted and Image-guided Drug Delivery into Peritoneal Tumors following Intraperitoneal Delivery. Theranostics 7:1689–1704. doi: 10.7150/thno.18125

180. Biffi S, Petrizza L, Garrovo C, et al (2016) Multimodal Near-Infrared-Emitting PluS Silica Nanoparticles with Fluorescent, Photoacoustic, and Photothermal Capabilities. Int J Nanomedicine 11:4865–4874. doi: 10.2147/IJN.S107479

181. Lu Z, Pham TT, Rajkumar V, et al (2018) A Dual Reporter Iodinated Labeling Reagent for Cancer Positron Emission Tomography Imaging and Fluorescence-Guided Surgery. J Med Chem 61:1636–1645. doi: 10.1021/acs.jmedchem.7b01746

182. Nagaya T, Nakamura Y, Sato K, et al (2017) Near Infrared Photoimmunotherapy

with Avelumab, an Anti-Programmed Death-Ligand 1 (PD-L1) Antibody. Oncotarget 8:8807–8817. doi: 10.18632/oncotarget.12410

183. Maruoka Y, Nagaya T, Nakamura Y, et al (2017) Evaluation of Early Therapeutic Effects after Near-Infrared Photoimmunotherapy (NIR-PIT) Using Luciferase–Luciferin Photon-Counting and Fluorescence Imaging. Mol Pharm 14:4628–4635. doi: 10.1021/acs.molpharmaceut.7b00731

184. Sun Q, You Q, Wang J, et al (2018) Theranostic Nanoplatform: Triple-Modal Imaging-Guided Synergistic Cancer Therapy Based on Liposome-Conjugated Mesoporous Silica Nanoparticles. ACS Appl Mater Interfaces 10:1963–1975. doi: 10.1021/acsami.7b13651

185. Li X, Schumann C, Albarqi HA, et al (2018) A Tumor-Activatable Theranostic Nanomedicine Platform for NIR Fluorescence-Guided Surgery and Combinatorial Phototherapy. Theranostics 8:767–784. doi: 10.7150/thno.21209

186. Sun Y, Ding M, Zeng X, et al (2017) Novel Bright-Emission Small-Molecule NIR-II Fluorophores for in Vivo Tumor Imaging and Image-Guided Surgery. Chem Sci 8:3489–3493. doi: 10.1039/C7SC00251C

187. Cheng K, Chen H, Jenkins CH, et al (2017) Synthesis, Characterization, and Biomedical Applications of a Targeted Dual-Modal Near-Infrared-II Fluorescence and Photoacoustic Imaging Nanoprobe. ACS Nano 11:12276–12291. doi: 10.1021/acsnano.7b05966

188. Miao W, Kim H, Gujrati V, et al (2016) Photo-decomposable Organic Nanoparticles for Combined Tumor Optical Imaging and Multiple Phototherapies. Theranostics 6:2367–2379. doi: 10.7150/thno.15829

189. Liu L, Ruan Z, Yuan P, et al (2018) Oxygen Self-Sufficient Amphiphilic

Polypeptide Nanoparticles Encapsulating BODIPY for Potential Near Infrared Imaging-guided Photodynamic Therapy at Low Energy. Nanotheranostics 2:59–69 . doi: 10.7150/ntno.22754

190. Olson MT, Wojtynek NE, Talmon GA, et al (2020) Development of a MUC16-Targeted Near-Infrared Fluorescent Antibody Conjugate for Intraoperative Imaging of Pancreatic Cancer. Mol Cancer Ther 19:1670–1681. doi: 10.1158/1535-7163.MCT-20-0033

191. McGuigan A, Kelly P, Turkington RC, et al (2018) Pancreatic Cancer: A Review of Clinical Diagnosis, Epidemiology, Treatment and Outcomes. World J Gastroenterol 24:4846–4861. doi: 10.3748/wjg.v24.i43.4846

192. Tempero MA, Malafa MP, Al-Hawary M, et al (2017) Pancreatic Adenocarcinoma, Version 2.2017, NCCN Clinical Practice Guidelines in Oncology. J Natl Compr Cancer Netw 15:1028–1061. doi: 10.6004/jnccn.2017.0131

193. Merkow RP, Bilimoria KY, Bentrem DJ, et al (2014) National Assessment of Margin Status as a Quality Indicator after Pancreatic Cancer Surgery. Ann Surg Oncol 21:1067–1074. doi: 10.1245/s10434-013-3338-2

194. Barugola G, Partelli S, Marcucci S, et al (2009) Resectable Pancreatic Cancer: Who Really Benefits From Resection? Ann Surg Oncol 16:3316–3322. doi: 10.1245/s10434-009-0670-7

195. Niesen W, Hank T, Büchler M, Strobel O (2019) Local Radicality and Survival Outcome of Pancreatic Cancer Surgery. Ann Gastroenterol Surg 3:464–475. doi: 10.1002/ags3.12273

196. Konstantinidis IT, Warshaw AL, Allen JN, et al (2013) Pancreatic Ductal Adenocarcinoma. Ann Surg 257:731–736. doi: 10.1097/SLA.0b013e318263da2f

197. Frangioni J V. (2008) New Technologies for Human Cancer Imaging. J. Clin. Oncol. 26:4012–4021

198. Lwin TM, Hoffman RM, Bouvet M (2018) The Development of Fluorescence Guided surgery for Pancreatic Cancer: from Bench to Clinic. Expert Rev Anticancer Ther 18:651–662. doi: 10.1080/14737140.2018.1477593

199. Wittrup KD, Thurber GM, Schmidt MM, Rhoden JJ (2012) Practical Theoretic Guidance for the Design of Tumor-Targeting Agents. Academic Press

200. Hoogstins CES, Boogerd LSF, Sibinga Mulder BG, et al (2018) Image-Guided Surgery in Patients with Pancreatic Cancer: First Results of a Clinical Trial Using SGM-101, a Novel Carcinoembryonic Antigen-Targeting, Near-Infrared Fluorescent Agent. Ann Surg Oncol 25:3350–3357. doi: 10.1245/s10434-018-6655-7

201. Streppel MM, Vincent A, Mukherjee R, et al (2012) Mucin 16 (Cancer Antigen 125) Expression in Human Tissues and Cell Lines and Correlation with Clinical Outcome in Adenocarcinomas of the Pancreas, Esophagus, Stomach, and Colon. Hum Pathol 43:1755–176 . doi: 10.1016/j.humpath.2012.01.005

202. Felder M, Kapur A, Gonzalez-Bosquet J, et al (2014) MUC16 (CA125): Tumor Biomarker to Cancer Therapy, a Work in Progress. Mol Cancer 13:129. doi: 10.1186/1476-4598-13-129

203. Haridas D, Chakraborty S, Ponnusamy MP, et al (2011) Pathobiological Implications of MUC16 Expression in Pancreatic Cancer. PLoS One 6:e26839. doi: 10.1371/journal.pone.0026839

204. Jiang K, Tan E, Sayegh Z, et al (2017) Cancer Antigen 125 (CA125, MUC16) Protein Expression in the Diagnosis and Progression of Pancreatic Ductal

Adenocarcinoma. Appl Immunohistochem Mol Morphol 25:620–623. doi: 10.1097/PAI.0000000000000368

205. Qi B, Crawford AJ, Wojtynek NE, et al (2018) Indocyanine Green Loaded Hyaluronan-Derived Nanoparticles for Fluorescence-Enhanced Surgical Imaging of Pancreatic Cancer. Nanomedicine Nanotechnology, Biol Med 14:769–780. doi: 10.1016/j.nano.2017.12.015

206. Hill TK, Kelkar SS, Wojtynek NE, et al (2016) Near Infrared Fluorescent Nanoparticles Derived from Hyaluronic Acid Improve Tumor Contrast for Image-Guided Surgery. Theranostics 6:2314–2328. doi: 10.7150/thno.16514

207. Mohs AM, Mancini MC, Singhal S, et al (2010) Hand-Held Spectroscopic Device for in Vivo and Intraoperative Tumor Detection: Contrast Enhancement, Detection Sensitivity, and Tissue Penetration. Anal Chem 82:9058–65. doi: 10.1021/ac102058k

208. Thériault C, Pinard M, Comamala M, et al (2011) MUC16 (CA125) Regulates Epithelial Ovarian Cancer Cell Growth, Tumorigenesis and Metastasis. Gynecol Oncol 121:434–443. doi: 10.1016/j.ygyno.2011.02.020

209. Gao Y, Hernandez C, Yuan H-X, et al (2017) Ultrasound Molecular Imaging of Ovarian Cancer with CA-125 Targeted Nanobubble Contrast Agents. Nanomedicine Nanotechnology, Biol Med 13:2159–2168. doi: 10.1016/j.nano.2017.06.001

210. Marshall M V, Draney D, Sevick-Muraca EM, Olive DM (2010) Single-Dose Intravenous Toxicity Study of IRDye 800CW in Sprague-Dawley Rats. Mol Imaging Biol 12:583–94. doi: 10.1007/s11307-010-0317-x

211. Tummers WS, Warram JM, van den Berg NS, et al (2018) Recommendations for

Reporting on Emerging Optical Imaging Agents to Promote Clinical Approval. Theranostics 8:5336–5347

212. Cilliers C, Liao J, Atangcho L, Thurber GM (2015) Residualization Rates of Near-Infrared Dyes for the Rational Design of Molecular Imaging Agents. Mol Imaging Biol 17:757–762. doi: 10.1007/s11307-015-0851-7

213. Oliveira-Cunha M, Newman WG, Siriwardena AK (2011) Epidermal Growth Factor Receptor in Pancreatic Cancer. Cancers (Basel) 3:1513–1526. doi: 10.3390/cancers3021513

214. Tummers WS, Farina-Sarasqueta A, Boonstra MC, et al (2017) Selection of Optimal Molecular Targets for Tumor-Specific Imaging in Pancreatic Ductal Adenocarcinoma. Oncotarget 8:56816–56828. doi: 10.18632/oncotarget.18232

215. Heath CH, Deep NL, Sweeny L, et al (2012) Use of Panitumumab-IRDye800 to Image Microscopic Head and Neck Cancer in an Orthotopic Surgical Model. Ann Surg Oncol 19:3879–3887. doi: 10.1245/s10434-012-2435-y

216. Gutowski M, Framery B, Boonstra MC, et al (2017) SGM-101: An Innovative Near-Infrared Dye-Antibody Conjugate that Targets CEA for Fluorescence-Guided Surgery. Surg Oncol 26:153–162. doi: 10.1016/j.suronc.2017.03.002

217. Lwin TM, Miyake K, Murakami T, et al (2018) Fluorescent Humanized Anti-CEA Antibody Specifically Labels Metastatic Pancreatic Cancer in a Patient-Derived Orthotopic Xenograft (PDOX) Mouse Model. Oncotarget 9:37333–37342. doi: 10.18632/oncotarget.26484

218. Tummers WS, Kimura RH, Abou-Elkacem L, et al (2018) Development and Preclinical Validation of a Cysteine Knottin Peptide Targeting Integrin αvβ6 for Near-infrared Fluorescent-guided Surgery in Pancreatic Cancer. Clin Cancer Res

24:1667–1676. doi: 10.1158/1078-0432.CCR-17-2491

219. Boonstra MC, Tolner B, Schaafsma BE, et al (2015) Preclinical Evaluation of a Novel CEA-Targeting Near-Infrared Fluorescent Tracer Delineating Colorectal and Pancreatic Tumors. Int J Cancer 137:1910–1920. doi: 10.1002/ijc.29571

220. Zhang L, Sanagapalli S, Stoita A (2018) Challenges in Diagnosis of Pancreatic Cancer. World J Gastroenterol 24:2047–2060. doi: 10.3748/wjg.v24.i19.2047

221. Liu X, Fu Y, Chen Q, et al (2018) Predictors of Distant Metastasis on Exploration in Patients with Potentially Resectable Pancreatic Cancer. BMC Gastroenterol 18:168. doi: 10.1186/s12876-018-0891-y

222. Vaisman-Mentesh A, Gutierrez-Gonzalez M, DeKosky BJ, Wine Y (2020) The Molecular Mechanisms That Underlie the Immune Biology of Anti-drug Antibody Formation Following Treatment With Monoclonal Antibodies. Front Immunol 0:1951. doi: 10.3389/FIMMU.2020.01951

223. Kuus-Reichel K, Grauer LS, Karavodin LM, et al (1994) Will Immunogenicity Limit the Use, Efficacy, and Future Development of Therapeutic Monoclonal Antibodies? Clin Diagn Lab Immunol 1:365

224. Lu R-M, Hwang Y-C, Liu I-J, et al (2020) Development of Therapeutic Antibodies for the Treatment of Diseases. J Biomed Sci 2020 271 27:1–30. doi: 10.1186/S12929-019-0592-Z

225. Erkan M, Hausmann S, Michalski CW, et al (2012) The Role of Stroma in Pancreatic Cancer: Diagnostic and Therapeutic Implications. Nat Rev Gastroenterol Hepatol 9:454–467. doi: 10.1038/nrgastro.2012.115

226. Dougan M, Ingram JR, Jeong HJ, et al (2018) Targeting Cytokine Therapy to the Pancreatic Tumor Microenvironment Using PD-L1–Specific VHHs. Cancer

Immunol Res 6:389–401. doi: 10.1158/2326-6066.CIR-17-0495

227. Xenaki KT, Oliveira S, van Bergen En Henegouwen PMP (2017) Antibody or Antibody Fragments: Implications for Molecular Imaging and Targeted Therapy of Solid Tumors. Front Immunol 8:1287. doi: 10.3389/fimmu.2017.01287

228. Rochefort MM, Girgis MD, Knowles SM, et al (2014) A Mutated Anti-CA19-9 scFv-Fc for Positron Emission Tomography of Human Pancreatic Cancer Xenografts. Mol Imaging Biol 16:721–729. doi: 10.1007/s11307-014-0733-4

229. Eskander MF, de Geus SWL, Kasumova GG, et al (2017) Evolution and Impact of Lymph Node Dissection during Pancreaticoduodenectomy for Pancreatic Cancer. Surgery 161:968–976. doi: 10.1016/j.surg.2016.09.032

230. Ashfaq A, Pockaj BA, Gray RJ, et al (2014) Nodal Counts and Lymph Node Ratio Impact Survival After Distal Pancreatectomy for Pancreatic Adenocarcinoma. J Gastrointest Surg 18:1929–193 . doi: 10.1007/s11605-014-2566-5

231. Ulmert D, Evans MJ, Holland JP, et al (2012) Imaging Androgen Receptor Signaling with a Radiotracer Targeting Free Prostate-Specific Antigen. Cancer Discov 2:320–327. doi: 10.1158/2159-8290.CD-11-0316

232. Sharma SK, Wuest M, Wang M, et al (2014) Immuno-PET of Epithelial Ovarian Cancer: Harnessing the Potential of CA125 for Non-Invasive Imaging. EJNMMI Res 4:60. doi: 10.1186/s13550-014-0060-4

233. Viola-Villegas NT, Rice SL, Carlin S, et al (2013) Applying PET to Broaden the Diagnostic Utility of the Clinically Validated CA19.9 Serum Biomarker for Oncology. J Nucl Med 54:1876–1882. doi: 10.2967/jnumed.113.119867

234. Liu JFF, Moore KNN, Birrer MJJ, et al (2016) Phase I Study of Safety and Pharmacokinetics of the anti-MUC16 Antibody–Drug Conjugate DMUC5754A in

Patients with Platinum-Resistant Ovarian Cancer or Unresectable Pancreatic Cancer. Ann Oncol 27:2124–2130. doi: 10.1093/annonc/mdw401

235. De Dosso S, Siebenhüner AR, Winder T, et al (2021) Treatment Landscape of Metastatic Pancreatic Cancer. Cancer Treat Rev 96:102180. doi: 10.1016/j.ctrv.2021.102180

236. Rawla P, Rawla P, Sunkara T, Gaduputi V (2019) Epidemiology of Pancreatic Cancer: Global Trends, Etiology and Risk Factors. World J Oncol 10:10–27. doi: 10.4021/wjon.v10i1.1166

237. Mizrahi JD, Surana R, Valle JW, Shroff RT (2020) Pancreatic Cancer. Lancet 395:2008–2020. doi: 10.1016/S0140-6736(20)30974-0

238. Raufi AG, Manji GA, Chabot JA, Bates SE (2019) Neoadjuvant Treatment for Pancreatic Cancer. Semin Oncol 46:19–27. doi: https://doi.org/10.1053/j.seminoncol.2018.12.002

239. Seufferlein T, Ettrich TJ (2019) Treatment of Pancreatic Cancer—Neoadjuvant Treatment in Resectable Pancreatic Cancer (PDAC). Transl Gastroenterol Hepatol 4: . doi: 10.21037/tgh.2019.03.05

240. Katz MHG, Shi Q, Ahmad SA, et al (2016) Preoperative Modified FOLFIRINOX Treatment Followed by Capecitabine-Based Chemoradiation for Borderline Resectable Pancreatic Cancer: Alliance for Clinical Trials in Oncology Trial A021101. JAMA Surg 151:e161137. doi: 10.1001/JAMASURG.2016.1137

241. Janssen QP, Buettner S, Suker M, et al (2019) Neoadjuvant FOLFIRINOX in Patients With Borderline Resectable Pancreatic Cancer: A Systematic Review and Patient-Level Meta-Analysis. JNCI J Natl Cancer Inst 111:782–794. doi: 10.1093/JNCI/DJZ073

242. Suker M, Beumer BR, Sadot E, et al (2016) A Patient-Level Meta-Analysis of FOLFIRINOX for Locally Advanced Pancreatic Cancer. Lancet Oncol 17:801. doi: 10.1016/S1470-2045(16)00172-8

243. Costa WL da, Cao HST, Massarweh NN (2020) Neoadjuvant Treatment for Patients With Localized Pancreatic Adenocarcinoma: Are We There Yet? JAMA Oncol 6:1163–1164. doi: 10.1001/JAMAONCOL.2020.0562

244. Shaib WL, Sayegh L, Zhang C, et al (2019) Induction Therapy in Localized Pancreatic Cancer. Pancreas 48:913–919. doi: 10.1097/MPA.0000000000001353

245. Tummers WS, Willmann JK, Bonsing BA, et al (2018) Advances in Diagnostic and Intraoperative Molecular Imaging of Pancreatic Cancer. Pancreas 47:675. doi: 10.1097/MPA.0000000000001075

246. Zhang Y, Huang Z-X, Song B (2021) Role of Imaging in Evaluating the Response After Neoadjuvant Treatment for Pancreatic Ductal Adenocarcinoma. World J Gastroenterol 27:3037. doi: 10.3748/WJG.V27.I22.3037

247. Grossberg AJ, Chu LC, Deig CR, et al (2020) Multidisciplinary Standards of Care and Recent Progress in Pancreatic Ductal Adenocarcinoma. CA Cancer J Clin 70:375–403. doi: 10.3322/CAAC.21626

248. Jarvi, Justin; Tewodros, Marta; Wang, Minan; Cheng, Mingshan; Creamer-Hente M (2016) Refining the PDX Mouse Model: Development of a Less Invasive and Disposable Tumor Engraftment Process. Lab Anim Sci Prof 47–51

249. Hwang WYK, Foote J (2005) Immunogenicity of Engineered Antibodies. Methods 36:3–10 . doi: 10.1016/J.YMETH.2005.01.001

250. Zinn KR, Korb M, Samuel S, et al (2015) IND-Directed Safety and Biodistribution Study of Intravenously Injected Cetuximab-IRDye800 in Cynomolgus Macaques.

Mol Imaging Biol 17:49. doi: 10.1007/S11307-014-0773-9

251. Cilliers C, Nessler I, Christodolu N, Thurber GM (2017) Tracking Antibody Distribution with Near-Infrared Fluorescent Dyes: Impact of Dye Structure and Degree of Labeling on Plasma Clearance. doi: 10.1021/acs.molpharmaceut.6b01091

252. Cohen R, Vugts DJ, Stigter-Van Walsum M, et al (2013) Inert Coupling of IRDye800CW and Zirconium-89 to Monoclonal Antibodies for Single- or Dual-Mode Fluorescence and PET Imaging. Nat Protoc 8:1010–1018. doi: 10.1038/nprot.2013.054

253. Peixoto RDD, Speers C, McGahan CEE, et al (2015) Prognostic Factors and Sites of Metastasis in Unresectable Locally Advanced Pancreatic Cancer. Cancer Med 4:1171. doi: 10.1002/CAM4.459

254. Cohen R, Stammes MA, de Roos IH, et al (2011) Inert Coupling of IRDye800CW to Monoclonal Antibodies for Clinical Optical Imaging of Tumor Targets

255. Lu G, Fakurnejad S, Martin BA, et al (2020) Predicting Therapeutic Antibody Delivery into Human Head and Neck Cancers. Clin Cancer Res 26:2582–2594. doi: 10.1158/1078-0432.CCR-19-3717

256. Pogue BW, M.D. ELR, Achilefu S, Dam GM van (2018) Perspective Review of What is Needed for Molecular-Specific Fluorescence-Guided Surgery. J Biomed Opt 23:100601. doi: 10.1117/1.JBO.23.10.100601

257. Oosten M van, Crane LM, Bart J, et al (2011) Selecting Potential Targetable Biomarkers for Imaging Purposes in Colorectal Cancer Using TArget Selection Criteria (TASC): A Novel Target Identification Tool. Transl Oncol 4:71. doi: 10.1593/TLO.10220

258. Boonstra MC, Geus SWL De, Prevoo HAJM, et al (2016) Selecting Targets for Tumor Imaging: An Overview of Cancer-Associated Membrane Proteins: https://doi.org/104137/BICS38542 8:BIC.S38542. doi: 10.4137/BIC.S38542

259. Chen K, Chen X (2010) Design and Development of Molecular Imaging Probes. Curr Top Med Chem 10:1227

260. Agdeppa ED, Spilker ME (2009) A Review of Imaging Agent Development. AAPS J 11:286. doi: 10.1208/S12248-009-9104-5

261. Sharma SK, Sevak KK, Monette S, et al (2016) Preclinical (89)Zr Immuno-PET of High-Grade Serous Ovarian Cancer and Lymph Node Metastasis. J Nucl Med 57:771–776. doi: 10.2967/jnumed.115.167072

262. Lamberts LE, Koch M, De Jong JS, et al (2017) Tumor-Specific Uptake of Fluorescent Bevacizumab-IRDye800CW Microdosing in Patients with Primary Breast Cancer: A Phase I Feasibility Study. Clin Cancer Res 23:2730–2741. doi: 10.1158/1078-0432.CCR-16-0437

263. Elekonawo FMKMK, Gooyer JM de M de, Bos DLL, et al (2020) Ex Vivo Assessment of Tumor-Targeting Fluorescent Tracers for Image-Guided Surgery. Cancers (Basel) 12. doi: 10.3390/CANCERS12040987

264. Rump A, Morikawa Y, Tanaka M, et al (2004) Binding of Ovarian Cancer Antigen CA125/MUC16 to Mesothelin Mediates Cell Adhesion *. J Biol Chem 279:9190–9198 . doi: 10.1074/JBC.M312372200

265. Ginath S, Menczer J, Fintsi Y, et al (2002) Tissue and Serum CA125 Expression in Endometrial Cancer. Int J Gynecol Cancer 12:372–375. doi: 10.1136/IJGC-00009577-200207000-00007

266. Giamougiannis P, Martin-Hirsch PLL, Martin FLL (2021) The Evolving Role of

MUC16 (CA125) in the Transformation of Ovarian Cells and the Progression of Neoplasia. Carcinogenesis 42:327–343. doi: 10.1093/CARCIN/BGAB010

267. Achterberg FB, Deken & MM, Meijer & RPJ, et al (2020) Clinical Translation and Implementation of Optical Imaging Agents for Precision Image-Guided Cancer Surgery. Eur J Nucl Med Mol Imaging 2020 482 48:332–339

268. Rosenthal EL, Warram JM, Boer E de, et al (2016) Successful Translation of Fluorescence Navigation During Oncologic Surgery: A Consensus Report. J Nucl Med 57:144–150. doi: 10.2967/JNUMED.115.158915

269. Gao RW, Teraphongphom N, de Boer E, et al (2018) Safety of Panitumumab-IRDye800CW and Cetuximab-IRDye800CW for Fluorescence-Guided Surgical Navigation in Head and Neck Cancers. Theranostics 8:2488–2495. doi: 10.7150/thno.24487

270. Lamberts LE, Koch M, de Jong JS, et al Personalized Medicine and Imaging Tumor-Specific Uptake of Fluorescent Bevacizumab–IRDye800CW Microdosing in Patients with Primary Breast Cancer: A Phase I Feasibility Study. Clin Cancer Res 23:2730–41. doi: 10.1158/1078-0432.CCR-16-0437

271. Korb ML, Hartman YE, Kovar J, et al (2014) Use of Monoclonal Antibody-IRDye800CW Bioconjugates in the Resection of Breast Cancer. J Surg Res 188:119–28. doi: 10.1016/j.jss.2013.11.1089

272. Nair AB, Jacob S (2016) A Simple Practice Guide for Dose Conversion Between Animals and Human. J Basic Clin Pharm 7:27. doi: 10.4103/0976-0105.177703

273. Koseoglu M, Hur A, Atay A, Cuhadar S (2011) Effects of Hemolysis Interference on Routine Biochemistry Parameters. Biochem Medica 21:79–85. doi: 10.11613/BM.2011.015

274. Ni J, Zhu W, Wang Y, et al (2021) A Reference Chart for Clinical Biochemical Tests of Hemolyzed Serum Samples. J Clin Lab Anal 35:e23561. doi: 10.1002/JCLA.23561

275. Reagan-Shaw S, Nihal M, Ahmad N (2008) Dose Translation from Animal to Human Studies Revisited. FASEB J 22:659–661. doi: 10.1096/fj.07-9574lsf

276. (2010) Guidance for Industry M3(R2) Nonclinical Safety Studies for the Conduct of Human Clinical Trials and Marketing Authorization for Pharmaceuticals Guidance for Industry

277. Wang Y, Cheon D-J, Lu Z, et al (2008) MUC16 Expression During Embryogenesis, in Adult Tissues, and Ovarian Cancer in the Mouse. Differentiation 76:1081. doi: 10.1111/J.1432-0436.2008.00295.X

278. Bernhard W, Barreto K, El-Sayed A, et al (2021) Pre-Clinical Study of IRDye800CW-Nimotuzumab Formulation, Stability, Pharmacokinetics, and Safety. BMC Cancer 2021 211 21:1–13. doi: 10.1186/S12885-021-08003-3

279. Sullivan R, Alatise OI, Anderson BO, et al (2015) Global Cancer Surgery: Delivering Safe, Affordable, and Timely Cancer Surgery. Lancet Oncol 16:1193–1224. doi: 10.1016/S1470-2045(15)00223-5

280. Orosco RK, Tapia VJ, Califano JA, et al (2018) Positive Surgical Margins in the 10 Most Common Solid Cancers. Sci Reports 2018 81 8:1–9. doi: 10.1038/s41598-018-23403-5

281. Heidkamp J, Scholte M, Rosman C, et al (2021) Novel Imaging Techniques for Intraoperative Margin Assessment in Surgical Oncology: A Systematic Review. Int J Cancer 149:635–645. doi: 10.1002/ijc.33570

282. Ghaneh P, Kleeff J, Halloran CM, et al (2019) The Impact of Positive Resection

Margins on Survival and Recurrence Following Resection and Adjuvant Chemotherapy for Pancreatic Ductal Adenocarcinoma. Ann Surg 269:520–529. doi: 10.1097/SLA.0000000000002557

283. Lwin TM, Hoffman RM, Bouvet M (2020) The Future of Tumour-Specific Fluorescence-Guided Surgery for Pancreatic Cancer. Lancet Gastroenterol Hepatol 5:715–717. doi: 10.1016/S2468-1253(20)30123-0

284. Schachtschneider KM, Schwind RM, Newson J, et al (2017) The Oncopig Cancer Model: An Innovative Large Animal Translational Oncology Platform. Front Oncol 0:190. doi: 10.3389/FONC.2017.00190

285. Gould SE, Junttila MR, de Sauvage FJ (2015) Translational Value of Mouse Models in Oncology Drug Development. Nat Med 2015 215 21:431–439. doi: 10.1038/nm.3853

286. Bailey KL, Carlson MA (2019) Porcine Models of Pancreatic Cancer. Front Oncol 0:144. doi: 10.3389/FONC.2019.00144

287. Rosenthal EL, Warram JM, de Boer E, et al (2016) Successful Translation of Fluorescence Navigation During Oncologic Surgery: A Consensus Report. J Nucl Med 57:144–50. doi: 10.2967/jnumed.115.158915

288. Steinkamp PJ, Voskuil FJ, van der Vegt B, et al (2021) A Standardized Framework for Fluorescence-Guided Margin Assessment for Head and Neck Cancer Using a Tumor Acidosis Sensitive Optical Imaging Agent. Mol Imaging Biol 2021 1–9. doi: 10.1007/S11307-021-01614-Z

289. Koller M, Qiu S-Q, Linssen MD, et al (2018) Implementation and Benchmarking of a Novel Analytical Framework to Clinically Evaluate Tumor-Specific Fluorescent Tracers. Nat Commun 2018 91 9:1–11. doi: 10.1038/s41467-018-05727-y

290. Gao RW, Teraphongphom N, van den Berg NS, et al (2018) Determination of Tumor Margins with Surgical Specimen Mapping Using Near-Infrared Fluorescence. doi: 10.1158/0008-5472.CAN-18-0878

291. Cook D, Brown D, Alexander R, et al (2014) Lessons Learned From the Fate of AstraZeneca's Drug Pipeline: a Five-Dimensional Framework. Nat Rev Drug Discov 2014 136 13:419–431. doi: 10.1038/nrd4309

292. Morgan P, Brown DG, Lennard S, et al (2018) Impact of a Five-Dimensional Framework on R&D Productivity at AstraZeneca. Nat Rev Drug Discov 2018 173 17:167–181. doi: 10.1038/nrd.2017.244

293. Tsai S, George B, Wittmann D, et al (2020) Importance of Normalization of CA19-9 Levels following Neoadjuvant Therapy in Patients with Localized Pancreatic Cancer. Ann Surg 271:740–747. doi: 10.1097/SLA.0000000000003049

294. Verbeke C, Häberle L, Lenggenhager D, Esposito I (2018) Pathology Assessment of Pancreatic Cancer Following Neoadjuvant Treatment: Time to Move on. Pancreatology 18:467–476. doi: 10.1016/J.PAN.2018.04.010

295. Hentzen JEKR, Jongh SJ de, Hemmer PHJ, et al (2018) Molecular Fluorescence-Guided Surgery of Peritoneal Carcinomatosis of Colorectal Origin: A Narrative Review. J Surg Oncol 118:332–343. doi: 10.1002/JSO.25106

296. Saccomano M, Dullin C, Alves F, Napp J (2016) Preclinical Evaluation of Near-Infrared (NIR) Fluorescently Labeled Cetuximab as a Potential Tool for Fluorescence-Guided Surgery. Int J Cancer 139:2277–2289. doi: 10.1002/ijc.30277

297. Nishio N, Berg NS van den, Keulen S van, et al (2020) Optimal Dosing Strategy for Fluorescence-Guided Surgery with Panitumumab-IRDye800CW in Head and

Neck Cancer. Mol imaging Biol 22:156. doi: 10.1007/S11307-019-01358-X

298. Choi HS, Nasr K, Alyabyev S, et al (2011) Synthesis and In Vivo Fate of Zwitterionic Near-Infrared Fluorophores. Angew Chem Int Ed Engl 50:6258. doi: 10.1002/ANIE.201102459

299. Suh H, Valle S, Morris DL (2017) Targeting MUC16 in Cancer Therapy. Chemother Open Access 6:1–5. doi: 10.4172/2167-7700.1000235

300. Haridas D, Ponnusamy MP, Chugh S, et al (2014) MUC16: Molecular Analysis and Its Functional Implications in Benign and Malignant Conditions. FASEB J 28:4183–4199. doi: 10.1096/FJ.14-257352

301. Thomas D, Sagar S, Liu X, et al (2021) Isoforms of MUC16 Activate Oncogenic Signaling Through EGF Receptors to Enhance the Progression of Pancreatic Cancer. Mol Ther 29:1557–1571. doi: 10.1016/J.YMTHE.2020.12.029

302. Neoptolemos JP, Kleeff J, Michl P, et al (2018) Therapeutic Developments in Pancreatic Cancer: Current and Future Perspectives. Nat Rev Gastroenterol Hepatol 15:333–348. doi: 10.1038/s41575-018-0005-x

303. Dobson J, de Queiroz GF, Golding JP (2018) Photodynamic Therapy and Diagnosis: Principles and Comparative Aspects. Vet J 233:8–18. doi: 10.1016/j.tvjl.2017.11.012

304. Yano T, Kasai H, Horimatsu T, et al (2017) A Multicenter Phase II Study of Salvage Photodynamic Therapy Using Talaporfin Sodium (ME2906) and a Diode Laser (PNL6405EPG) for Local Failure After Chemoradiotherapy or Radiotherapy for Esophageal Cancer. Oncotarget 8:22135–22144. doi: 10.18632/oncotarget.14029

305. Maawy AA, Hiroshima Y, Zhang Y, et al (2015) Photoimmunotherapy Lowers

Recurrence After Pancreatic Cancer Surgery in Orthotopic Nude Mouse Models. J Surg Res 197:5–11. doi: 10.1016/j.jss.2015.02.037

306. Maawy AA, Hiroshima Y, Zhang Y, et al (2015) Near Infra-Red Photoimmunotherapy with Anti-CEA-IR700 Results in Extensive Tumor Lysis and a Significant Decrease in Tumor Burden in Orthotopic Mouse Models of Pancreatic Cancer. PLoS One 10:e0121989. doi: 10.1371/journal.pone.0121989

307. Nagaya T, Okuyama S, Ogata F, et al (2019) Near Infrared Photoimmunotherapy Using a Fiber Optic Diffuser for Treating Peritoneal Gastric Cancer Dissemination. Gastric Cancer 22:463–472. doi: 10.1007/s10120-018-0871-5

308. Nagaya T, Okuyama S, Ogata F, et al (2018) Endoscopic Near Infrared Photoimmunotherapy Using a Fiber Optic Diffuser for Peritoneal Dissemination of Gastric Cancer. Cancer Sci 109:1902–1908. doi: 10.1111/cas.13621

309. Okuyama S, Nagaya T, Sato K, et al (2018) Interstitial Near-Infrared Photoimmunotherapy: Effective Treatment Areas and Light Doses Needed for use with Fiber Optic Diffusers. Oncotarget 9:11159–11169. doi: 10.18632/oncotarget.24329

310. Ogata F, Nagaya T, Nakamura Y, et al (2017) Near-Infrared Photoimmunotherapy: A Comparison of Light Dosing Schedules. Oncotarget 8:35069–35075. doi: 10.18632/oncotarget.17047

311. Sato K, Ando K, Okuyama S, et al (2018) Photoinduced Ligand Release from a Silicon Phthalocyanine Dye Conjugated with Monoclonal Antibodies: A Mechanism of Cancer Cell Cytotoxicity after Near-Infrared Photoimmunotherapy. ACS Cent Sci 4:1559–1569. doi: 10.1021/acscentsci.8b00565

312. Kobayashi H, Choyke PL (2019) Near-Infrared Photoimmunotherapy of Cancer.

Acc Chem Res 52:2332–2339. doi: 10.1021/acs.accounts.9b00273

313. Lee ES, Lee JM (2014) Imaging Diagnosis of Pancreatic Cancer: a State-of-the-Art Review. World J Gastroenterol 20:7864–77. doi: 10.3748/wjg.v20.i24.7864

314. Alam IS, Steinberg I, Vermesh O, et al (2018) Emerging Intraoperative Imaging Modalities to Improve Surgical Precision. Mol Imaging Biol 2018 205 20:705–715. doi: 10.1007/S11307-018-1227-6

315. Wei W, Rosenkrans ZT, Liu J, et al (2020) ImmunoPET: Concept, Design, and Applications. Chem Rev 120:3787. doi: 10.1021/ACS.CHEMREV.9B00738

316. An F-F, Chan M, Kommidi H, Ting R (2016) Dual PET and Near-Infrared Fluorescence Imaging Probes as Tools for Imaging in Oncology. AJR Am J Roentgenol 207:266. doi: 10.2214/AJR.16.16181

317. Thomas D, Radhakrishnan P (2019) Tumor-Stromal Crosstalk in Pancreatic Cancer and Tissue Fibrosis. Mol Cancer 2019 181 18:1–15 . doi: 10.1186/S12943-018-0927-5

318. Jiang B, Zhou L, Lu J, et al (2020) Stroma-Targeting Therapy in Pancreatic Cancer: One Coin With Two Sides? Front Oncol 0:2272. doi: 10.3389/FONC.2020.576399

319. Hosein AN, Brekken RA, Maitra A (2020) Pancreatic Cancer Stroma: an Update on Therapeutic Targeting Strategies. Nat Rev Gastroenterol Hepatol 2020 178 17:487–505. doi: 10.1038/s41575-020-0300-1

320. Labrijn AF, Janmaat ML, Reichert JM, Parren PWHI (2019) Bispecific Antibodies: a Mechanistic Review of the Pipeline. Nat Rev Drug Discov 2019 188 18:585–608 . doi: 10.1038/s41573-019-0028-1

321. Oberg H-H, Peipp M, Kellner C, et al (2014) Novel Bispecific Antibodies Increase γδ T-Cell Cytotoxicity against Pancreatic Cancer Cells. Cancer Res 74:1349–1360. doi: 10.1158/0008-5472.CAN-13-0675

322. Lum LG, Thakur A, Choi M, et al (2020) Clinical and Immune Responses to anti-CD3 x anti-EGFR Bispecific Antibody Armed Activated T Cells (EGFR BATs) in Pancreatic Cancer Patients. https://doi.org/101080/2162402X20201773201 9: . doi: 10.1080/2162402X.2020.1773201

323. Thakur A, Ung J, Tomaszewski EN, et al (2021) Priming of Pancreatic Cancer Cells with Bispecific Antibody Armed Activated T Cells Sensitizes Tumors for Enhanced Chemoresponsiveness. https://doi.org/101080/2162402X20211930883 10. doi: 10.1080/2162402X.2021.1930883

324. Schizas D, Charalampakis N, Kole C, et al (2020) Immunotherapy for Pancreatic Cancer: A 2020 update. Cancer Treat Rev 86. doi: 10.1016/J.CTRV.2020.102016

325. Comer F, Gao C, Coats S (2018) Bispecific and Biparatopic Antibody Drug Conjugates. Cancer Drug Discov Dev 267–280 doi: 10.1007/978-3-319-78154-9_11